

# Search for the Supersymmetric Partner to the Top Quark using Recoils Against Strong Initial State Radiation

A DISSERTATION PRESENTED  
BY  
SIYUAN SUN  
TO  
THE DEPARTMENT OF PHYSICS

IN PARTIAL FULFILLMENT OF THE REQUIREMENTS  
FOR THE DEGREE OF  
DOCTOR OF PHILOSOPHY  
IN THE SUBJECT OF  
PHYSICS

HARVARD UNIVERSITY  
CAMBRIDGE, MASSACHUSETTS  
MAY 2017

©2014 – SIYUAN SUN  
ALL RIGHTS RESERVED.

# Search for the Supersymmetric Partner to the Top Quark using Recoils Against Strong Initial State Radiation

## ABSTRACT

The ATLAS experiment at Large Hadron Collider (LHC) searches for experimental evidence of many new beyond the standard model physics at the TeV scale. As we collect more data at the LHC we continue to extend our sensitivity to these new phenomenon, particularly probing increasingly more massive new particles. Despite this progress there are still regions of parameter space where constraints remain weak. One common cause of this lack of sensitivity is because the new particle has a very small mass splitting between it and its decay products. The particle then has little energy left over to give momenta to its decay products and the low momenta decay products are difficult to experimentally detect. These regions of small mass splitting are called *compressed* regions. We are able to gain sensitivity to these difficult regions by searching for new particles produced in conjunction with strong initial state radiation (ISR). The strong initial state radiation boosts the new particle's decay products and gives them momentum.

This thesis covers the search for the supersymmetric partner to the top quark (stop) in the region when the stop and its decay products are nearly degenerate in mass. No searches prior to 2016 was sensitive to this region. We were able to exclude stops up to a mass of 525 GeV in this region with the 2015 and 2016 ATLAS dataset. I will demonstrate a new and more accurate technique for identifying

whole initial state radiation systems instead of a single ISR jet. As the LHC provides more data and traditional search methods rule out parameter space at higher masses, it becomes more important that we also gain sensitivity to these compressed regions that are still unconstrained at low masses. I will show that this initial state radiation identification technique is completely generalizable and useful for many other searches that target small mass splittings.

# Contents

0	INTRODUCTION	I
1	THEORETICAL MOTIVATION	2
1.1	Introduction to Super-Symmetry . . . . .	2
2	EXPERIMENTAL APPARATUS	3
2.1	The Large Hadron Collider . . . . .	3
2.2	The ATLAS Detector . . . . .	5
2.2.1	The Inner Detector . . . . .	8
2.2.2	The Calorimeter . . . . .	12
2.2.3	The Muon Spectrometer . . . . .	14
3	OBJECT RECONSTRUCTION AT ATLAS	20
4	Monte Carlo Simulation of Physics Processes at ATLAS	21
4.1	Signal Monte Carlo Generation . . . . .	22
4.2	SM Background Monte Carlo Generation . . . . .	24
4.2.1	Standard Model $t\bar{t}$ Monte Carlo Generation . . . . .	24
4.2.2	Standard Model Single Top Monte Carlo Generation . . . . .	26
4.2.3	Standard Model $W + \text{jets}$ and $Z + \text{jets}$ Monte Carlo Generation . . . . .	28
4.2.4	Standard Model $t\bar{t} + V$ Monte Carlo Generation . . . . .	28
4.2.5	Standard Model $t\bar{t} + \gamma$ Monte Carlo Generation . . . . .	29
4.2.6	Standard Model Diboson Monte Carlo Generation . . . . .	29
4.3	Detector Simulation . . . . .	29
5	GENERAL ANALYSIS STRATEGY	31
5.1	General R-Parity Conserving SUSY Search Strategy . . . . .	31
5.2	General Strategies in Compressed Regions . . . . .	32
6	RECURSIVE JIGSAW RECONSTRUCTION FOR EVENTS WITH MISSING ENERGY AND IDENTIFYING ISR JETS	36
6.1	Introduction to Recursive Jigsaw Algorithm on Events with $E_T^{\text{miss}}$ . . . . .	37
6.2	Recursive Jigsaw Method of Identifying Initial State Radiation . . . . .	39
6.3	Performance of Initial State Radiation Identification Algorithm . . . . .	41
6.4	Kinematic Variables of Initial State Radiation and Sparticle Systems . . . . .	43

7	DEFINITIONS OF RECONSTRUCTED PHYSICS OBJECTS	45
7.1	Electron Definition . . . . .	46
7.2	Muon Definition . . . . .	46
7.3	Jet Definitions . . . . .	47
7.3.1	Calorimeter Jets . . . . .	47
7.3.2	$b$ -tagged Jets . . . . .	48
7.4	$E_T^{\text{miss}}$ Definitions . . . . .	48
7.4.1	Calorimeter-based $E_T^{\text{miss}}$ . . . . .	48
7.4.2	Track-based $E_T^{\text{miss}}$ . . . . .	49
7.5	Photon Definition . . . . .	49
7.6	Resolving overlapping objects . . . . .	49
8	EVENT SELECTIONS AND COLLISION DATA SAMPLES	51
8.1	Data Periods and Good Run List . . . . .	51
8.2	Event Preselection . . . . .	52
9	SIGNAL REGION DEFINITION	55
9.1	Physical Intuition on how Signal Region Selections Reject SM Background . . . .	55
9.2	Kinematic Variables Definitions . . . . .	58
9.3	Signal Region Kinematic Selection . . . . .	59
9.4	Signal Region Expected Yields and Kinematic Distributions . . . . .	64
9.5	Signal Region Background Composition . . . . .	65
10	STANDARD MODEL BACKGROUNDS	68
10.1	Common Background Estimation and Validation Techniques . . . . .	68
10.2	Dominant Background: Standard Model $t\bar{t}$ . . . . .	70
10.2.1	Two Kinematically Distinct Populations of $t\bar{t}$ . . . . .	71
10.2.2	Properties of $t\bar{t}$ in Signal Region . . . . .	73
10.2.3	Predicting the amount of $t\bar{t}$ in Signal Region using a One Lepton Control Region . . . . .	74
10.2.4	Validating $t\bar{t}$ Predictions in Signal Region using a Zero Lepton Validation Re- gion . . . . .	79
10.3	Subdominant Backgrounds . . . . .	82
10.3.1	Standard Model W+Jets . . . . .	82
10.3.2	Standard Model Single Top . . . . .	93
10.3.3	Standard Model $t\bar{t}$ +Z . . . . .	98
10.3.4	Standard Model Z+Jets . . . . .	105
10.3.5	Standard Model Diboson . . . . .	105
10.3.6	Standard Model QCD Multijet and all Hadronic $t\bar{t}$ . . . . .	105

II	SYSTEMATIC UNCERTAINTIES	III
II.O.1	Experimental Uncertainties . . . . .	II2
II.O.2	Theoretical Uncertainties . . . . .	II4
12	STATISTICAL ANALYSIS	126
12.1	Introduction to Log Likelihood Fitting . . . . .	126
12.2	Overview of Fitting to Control Regions and Signal Regions . . . . .	129
12.3	Parameterization of Systematics as Gaussian Constraints . . . . .	132
12.4	Background Only Fit and Background Estimation . . . . .	133
12.5	Exclusion Fit and Exclusion Limit Calculation . . . . .	134
12.6	Discovery Fit and Discovery Significance Calculation . . . . .	135
13	RESULTS	137
13.O.1	Unblinded distributions . . . . .	140
13.O.2	Background-only fit . . . . .	141
13.O.3	Exclusion-fit results . . . . .	150
14	INTERPRETATION OF RESULTS	154
15	CONCLUSION	155
	APPENDIX A SANITY CHECKS	156
	REFERENCES	157





# Acknowledgments

,

# Acknowledgments

,

# 0

## Introduction

# 1

## Theoretical Motivation

### 1.1 INTRODUCTION TO SUPER-SYMMETRY

# 2

## Experimental Apparatus

### 2.1 THE LARGE HADRON COLLIDER

The Large Hadron Collider (LHC) is the world's most powerful particle accelerator. By accelerating protons to 99.9999991 percent of the speed of light and smashing them in head on collisions, the LHC hopes to probe some of the most fundamental questions of physics. The LHC sits in a circular tunnel 27 km in circumference under the Franco-Swiss border near Geneva, Switzerland. A diagram

of the LHC complex is shown in figure 2.1

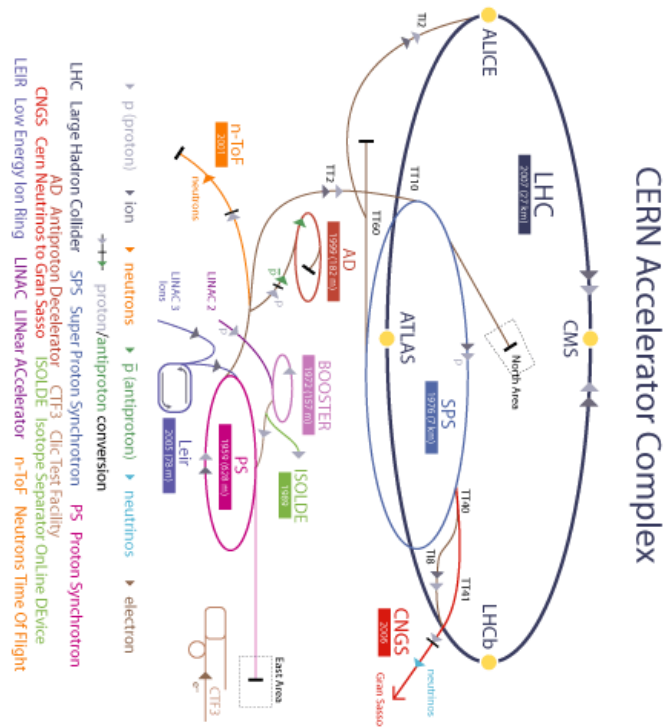


**Figure 2.1:** The Large Hadron Collider complex. (Taken from<sup>2</sup>)

The LHC expands upon older particle accelerators. First protons are obtained by stripping electrons from hydrogen atoms. These protons are accelerated by LINAC2, a older linear accelerator at CERN, to 31.4 percent of the speed of light. The Proton Synchrotron Booster (PSB) then boosts the protons to 91.6 percent of the speed of light. These protons are then dumped into the Proton Synchrotron (PS) and accelerated to 99.93 percent of the speed of light. Afterwards, the protons enter

the Super Proton Synchrotron (SPS). The SPS accelerate the proton to 99.9998 percent of the speed of light. At this point the energy of the proton is 450 GeV. These protons finally enter the LHC ring, which increases the proton energy to 3.5 TeV. This allows for a center of mass energy of 7 TeV during collisions.

The LHC is designed to accelerate the protons to energies of 7 TeV, creating 14 TeV center of mass collisions. The LHC is scheduled to achieve this target energy in two years.

The LHC has six particle detectors to detect the multitude of particles that are created during the collisions. The ALICE detector specializes in collisions of heavy ions. LHCb specializes in physics involving the bottom quark. TOTEM and LHCf are detectors measuring scattering cross sections, and diffractive processes, and cosmic ray physics. ATLAS and CMS are general purpose detectors optimized to detect a large spectrum of particles created by the proton proton collision.

This analysis uses data collected by the ATLAS detector.

## 2.2 THE ATLAS DETECTOR

The ATLAS Detector is a general purpose detector that detects a multitude of particles that is created by the proton proton collisions. The detector is 25 meters high and 44 meters long and weights over 7000 tons.<sup>3</sup> The detector consists of an inner tracking detector, the electromagnetic calorimeter, the hadronic calorimeter and the muon spectrometer. The structure of the ATLAS detector is shown in figure 2.2

The inner tracker detector is located closest to the collision beam and tracks the path of charged

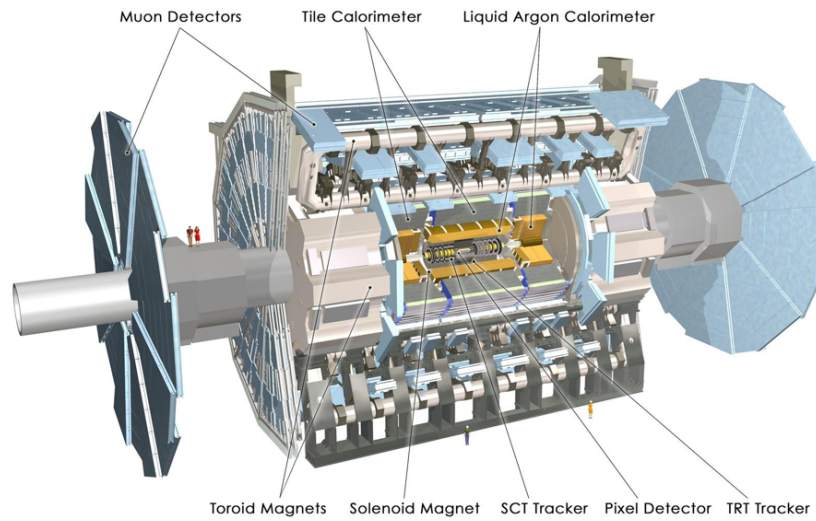


**Figure 2.2:** The ATLAS detector. Pixel, SCT, and TRT Detectors form the inner detector. (Taken from<sup>2</sup>)

particles such as electrons, and muons. The inner detector will be covered in further detail in section 2.2.1. The electromagnetic calorimeter (EM calorimeter) surrounds the inner detector and measures the amount of energy of electromagnetic particles such as electrons and photons. The hadronic calorimeter surrounds the electromagnetic calorimeter and measures the amount of energy of hadrons such as protons and neutrons. The calorimeters are described in further detail in section 2.2.2. The muon spectrometer forms the large outer layer of the detector, surrounding the hadronic calorimeter. Few particles other than muons and neutrinos can penetrate through the calorimeters. The muon spectrometer records the tracks left by the charged muons. The muon spectrometer is described in further detail in section 2.2.3. Neutrinos are undetectable and must be inferred through conservation of momentum. A diagram of the signature left by each particle type is given in figure

2.3

A photon is not charged and so leaves no track. Photons do interact electromagnetically and



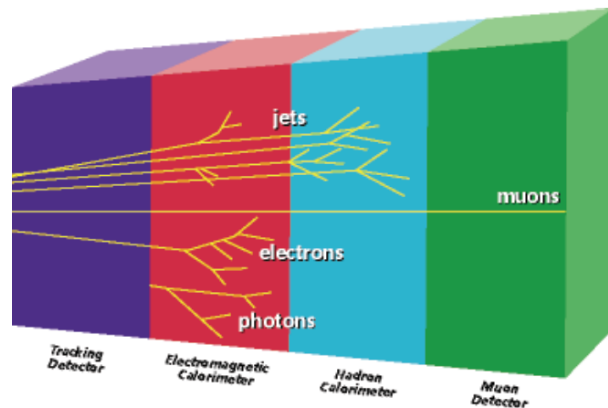


**Figure 2.3:** The signature left by different particles. (Taken from<sup>2</sup>)

therefore deposit all their energy in the EM calorimeter in the form of a cascading shower of electrons and photons. Electrons are charged and do leave a track in the inner detector and deposit their energy in the EM calorimeter. Pions and protons are charged and will leave a track in the inner detector, and they will deposit all their energy in the hadronic calorimeter. Neutrons are not charged and will not leave a track. Like protons, neutrons will deposit their energy in the hadronic calorimeter. Muons penetrate the detector and are charged. They will leave a track in both the inner detector and the muon spectrometer.

Almost all particles that the ATLAS detector is looking for are unstable, meaning the particles will decay before they reach the detector. The final decay product is almost always a combination of the above particles and the undetectable neutrino. The original particle's kinematics is then calculated from the kinematics of each of its measurable decay products.

Approximately 1000 particles are produced from the collision point every 75 nanoseconds at the Large Hadron Collider.<sup>3</sup> The ATLAS Detector uses a system of triggers to filter this vast amount of

data, recording only interesting collisions. The triggering system is complex and depends on the type of particle that is triggered on. This analysis uses the muon triggering system which is described in more detail in section ??.

The ATLAS detector has two equivalent coordinate systems. The rectangular coordinate system  $x, y, z$  is defined as follows. The  $z$  direction points in the direction of the beam pipe. The positive  $x$  direction points to the center of the LHC ring. The positive  $y$  direction points in the upward direction. The origin is defined as the center of the ATLAS detector and lie on the center line of the beam pipe. Alternatively, Radius  $R$  is defined as the distance from the  $z$  axis (also the beam axis). The azimuthal angle  $\varphi$  is measured around the beam axis, and the polar angle  $\vartheta$  is the angle from the beam axis. Frequently, the pseudorapidity, defined as  $\eta = -\ln \tan(\vartheta/2)$ , is used in place of  $\vartheta$  as the third coordinate.

#### 2.2.1 THE INNER DETECTOR

The inner detector surrounds the collider beam tube and tracks the path of charged particles including electrons, charged pions, protons, and muons. Figure 2.4 shows the configuration of the inner detector.

The inner detector consists of two silicon semiconductor detectors; the Pixel detector and the Semiconductor Tracker (SCT) and a straw tracker called the Transition Radiation Tracker (TRT). The three detectors operate independently of one another but the information they gather is combined during reconstruction to form a complete track of the particle as it flies through the inner detector. The whole inner detector is immersed in a 2 T magnetic field produced by a solenoidal su-

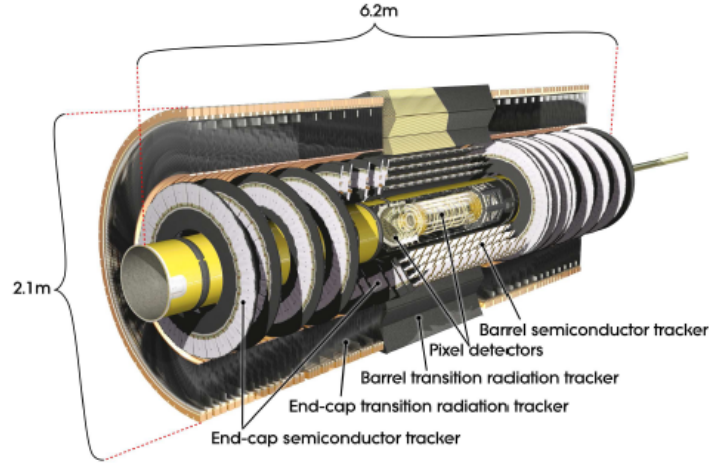


**Figure 2.4:** Cutaway view of the ATLAS inner detector. (Taken from<sup>2</sup>)

perconducting magnet that radially surrounds the whole inner detector. At this radii, around 1000 particles will emerge from the collision point every 75 ns demanding that the inner detector have good position and time resolution.<sup>3</sup>

The Pixel detector lies closest to the beam pipe. The Pixel detector uses thousands of pixels of doped silicon that form diodes. The diodes are placed in reverse bias within the larger electronic circuit. Hence no current will flow through the circuit unless the diode breaks down. As a charged particle pass through the diode, they cause small ionizations that momentarily breaks down the diode, allowing current to flow. This current can then be detected and measured.

The Pixel detector has three layers of pixel sensors in the cylindrical barrel and three wheels of pixel sensors in the endcaps covers a total  $|\eta|$  of 2.5. The pixels measures both the  $\phi$  and Z coordinate of the hit simultaneously, achieving  $10 \mu m$  accuracy in the (R -  $\phi$ ) direction and  $115 \mu m$  in the Z direction in the barrel and  $10 \mu m$  resolution in the (R -  $\phi$ ) direction and  $115 \mu m$  in the R direction in the

endcap.<sup>?</sup>

At larger radii, the SCT surrounds the Pixel detector. The SCT operates in a similar fashion to the Pixel detector as the SCT is also a silicon detector. Instead of pixels of doped silicon, the SCT uses narrow strips of doped silicon. Narrow strips allow measurement of only one coordinate (either the  $\phi$  or Z and not both like the Pixel Detectors) per strip but is more cost effective. To compensate for this, the SCT use two orthogonally oriented strips glued back to back to measure both coordinates. The SCT has four planes of these double strips in the cylindrical barrel and four wheels in the endcaps. The SCT can achieve position accuracies of  $17\ \mu m$  in the  $(R-\phi)$  direction and  $580\ \mu m$  in the Z direction in the barrel and  $17\ \mu m$  in the  $(R-\phi)$  direction and  $580\ \mu m$  in the R direction in the endcap.<sup>?</sup>

The TRT lies at a larger radii around both the SCT and the Pixel detector and covers an  $|\eta|$  range of 2.0. Unlike the two silicon detectors, the TRT is a straw tracker and is filled with around 300 thousand wire straws. The straws is filled with a combination of xenon,  $CO_2$ , and  $O_2$  gas. As a charged particle flies through the straw, it ionizes that gas within the straw. Voltage is applied to the wall of the straw and the central wire making the straw a capacitor. The positive gas ions and negative free electrons will follow the electric field lines of the capacitor and drift in opposite directions to the central wire and straw wall. The speed of the electron drift is known and based on the timing of the arrival of the first election and the last election, the distance from the center of the straw to the flight path of the charged particle can be determined. This allows the measurement of one coordinate of the particle's flight. This process is shown in figure 2.5.<sup>?</sup>

The TRT's straws in the barrel and endcaps are arranged to measure the  $\phi$  coordinate of the pass-

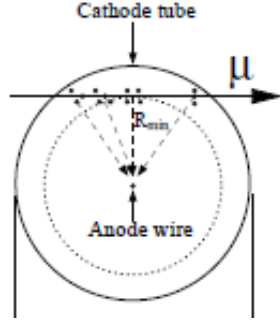


**Figure 2.5:** Cross-section of a straw tube with an interacting muon. (Taken from<sup>?</sup>)

ing charged particle. The  $\varphi$  direction is the direction in which charged particles bend. Therefore, the TRT helps to measure the momentum of the charged particle. The TRT provides  $(R-\varphi)$  direction information with an intrinsic accuracy of 130 mm per straw. This large resolution uncertainty is compensated by the large number of hits which a particle leaves in the TRT (around 36 hits per track is expected compared to 8 in the SCT and 3 in the Pixel).

The TRT also aids in electron identification. The space between the straws is filled with materials with different indexes of refraction. When ultra-relativistic charged particles crosses the boundaries of different materials, they produce transition radiation. The transition radiation will in turn further ionize the gas in the straw, producing a high threshold hit in the straw. Particles with small invariant masses such as electrons are more likely to emit transition radiation. This allows for another form of electron identification and complements the electron identification function of the calorimeter.

The hits in all three detectors are reconstructed into a track of the flight path of the charged particle by ATLAS reconstruction software. Depending on the curvature of the track, the momentum

and charge of the particle can be measured. By matching the track to other signals in the calorimeter or the muon spectrometer, the identity of the charged particle can be determined.

### 2.2.2 THE CALORIMETER

The calorimeter is separated into two types. The electromagnetic calorimeter (EM calorimeter) is designed to measure the energy of electromagnetic particles such as electrons and photons, and the hadronic calorimeter is designed to measure the energy of hadrons such as protons, neutrons, and pions. The calorimeter covers up to an  $\eta$  range of  $|\eta| < 4.9$ . The calorimeter is not only used to measure the energy of jets and particles but also used to reduce the probability of a non-muon particle from punching through to the outer muon detectors. Therefore the total thickness of the EM calorimeter is greater than 22 radiation lengths ( $X_0$ ) in the barrel and greater than  $24 X_0$  in the end-caps.<sup>2</sup> The cut away view of the whole calorimeter is show in figure 2.6

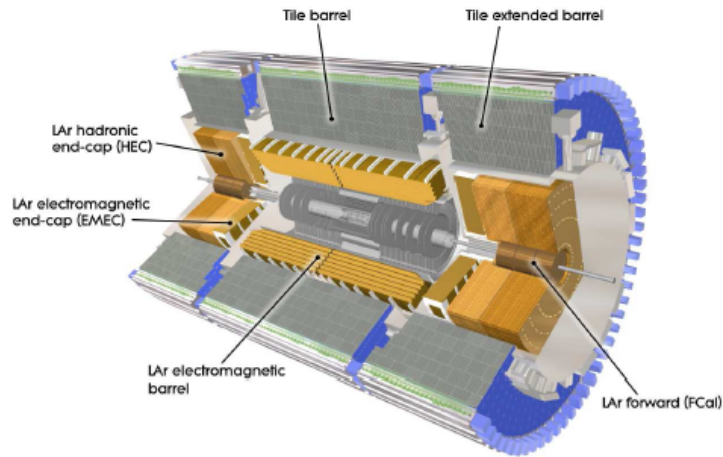


**Figure 2.6:** The ATLAS calorimeter. (Taken from<sup>2</sup>)

The inner most calorimeter is the liquid argon electromagnetic calorimeter (EM Calorimeter). The EM calorimeters are made of multiple planes of 1.5 mm thick lead plates. The 4 mm gap between the lead plates is filled with liquid argon. When high energy electrons or photons hit the lead plates they produce more electron-positron pairs through pair production. These newly produced electrons and positrons then will also produce more photons as they fly through the lead plates. This results in a shower of electrons and positrons until the photons no longer have enough energy to pair-produce. When the charged particles traverse the liquid argon, they ionize the argon. These ions and free electrons in the liquid argon drift to external electric terminals and are sensed as a current. The more energetic the initial electron or photon, the more electron - positron pairs will be produced causing a greater ionization in the liquid argon. Also, the more energetic the initial electron or photon, the deeper the electron shower will penetrate the calorimeter before it runs out of energy to produce more electron - positron pairs. Both are used to measure the total energy of the initial electromagnetic particle. The barrel part of the electromagnetic calorimeter covers up to an  $|\eta| < 1.475$  and the two endcaps covers the  $\eta$  range of  $1.375 < |\eta| < 3.2$ .

Outside the electromagnetic calorimeter lie the hadronic calorimeter. The hadronic calorimeter is formed by three different detectors, the barrel tile calorimeter, the hadronic endcap calorimeter (HEC) and the forward hadron calorimeter (FCal). The barrel tile calorimeter covers an  $\eta$  range  $|\eta| < 1.0$  and two extended barrel tile calorimeter covers  $0.8 < |\eta| < 1.7$ . The tile calorimeter consists of multiple steel plates with scintillating tiles sandwiched in between. When hadrons such as protons, neutrons, pions, and kaons pass, they interact with the nuclei in the steel via the strong force and produce more hadrons. Those hadrons in turn interact with more steel nuclei eventually

producing a shower of hadronic particles. As the hadrons pass the scintillating tiles, they cause the tiles to produce light that is amplified by a photomultiplier tube and then detected. The more energetic the initial hadron, the more hadrons produced in the hadronic shower and the more light is produced in the tiles. Also the more energetic the initial hadron, the deeper the hadronic shower penetrates before the hadrons no longer have enough energy to produce more hadrons. The HEC and the FCAL extends the  $\eta$  coverage of the hadronic calorimeter to an  $|\eta|$  of 4.9. Both are liquid argon calorimeters and operate in the same way as the EM calorimeter. The HEC uses copper instead of lead plates because copper is better at interacting with hadrons than lead. For the same reason, the FCAL uses copper-tungsten plates in place of lead.

### 2.2.3 THE MUON SPECTROMETER

The muon spectrometer tracks muons with high enough energy to penetrate the calorimeter. Few particles other than muons and the undetectable neutrino can penetrate the large calorimeter. The muon spectrometer consist of two precision tracking detectors, the Monitored Drift Tube (MDT) and the Cathode Strip Chamber (CSC), and two detectors used in muon triggering, the Resistive Plate Chambers (RPC) and the Thin Gap Chambers (TGC). The muon triggering system is discussed in more detail in ???. The configuration of the muon system is shown in figure 2.7

The muon spectrometer is immersed in a magnetic field produced by eight superconducting toroid magnets in the barrel and eight superconducting toroid magnets in the endcaps. The barrel magnets cover an  $|\eta|$  range of 1.4 and the endcap magnets cover an  $|\eta|$  range from 1.6 to 2.7. The area with  $1.4 < |\eta| < 1.6$  is called the transition region with a mixed magnetic field from both



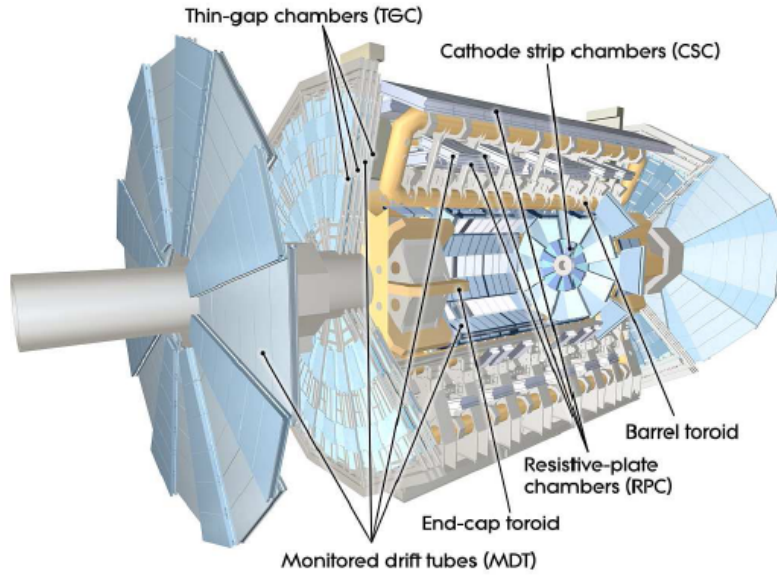


**Figure 2.7:** Cutaway view of the ATLAS Muon Spectrometer. (Taken from<sup>2</sup>)

the barrel and endcap. The endcap magnets are offset from the barrel magnets by 22.5 degrees in the  $\phi$  direction to allow a smoother magnetic field in this region. The configuration of the magnets is shown in figure 2.8

The magnetic field bends the charged muons in the  $\eta$  direction. The bending power of the magnets depends on the direction of muon travel. In the pseudorapidity range  $0 < |\eta| < 1.4$ , the barrel toroid provides 1.5 to 5.5 Tm of bending power. In between  $1.6 < |\eta| < 2.7$ , the end-cap toroids provide approximately 1 to 7.5 Tm of bending power. The bending power is lower in the transition region.

The path of the muon can be reconstructed and the momentum of the muon can be measured from the amount of bending. The size of the muon spectrometer combined with the inner detector

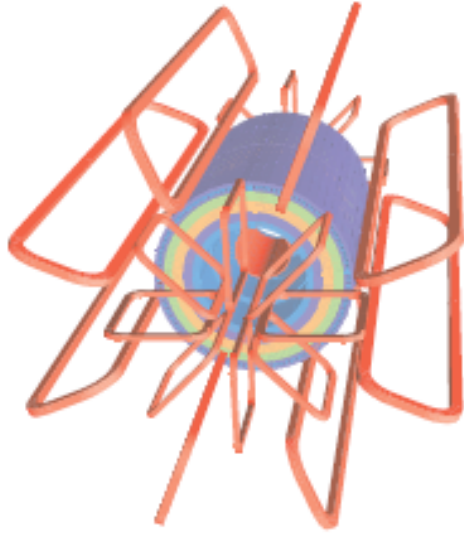


**Figure 2.8:** Geometry of the barrel and endcap toroid magnets. The cylinder represents the calorimeter. (Taken from<sup>2</sup>)

allows ATLAS to track muons over long distances. This is important because longer tracks mean more precise momentum measurements.<sup>3</sup>

The Monitored Drift Tube (MDT) consists of three to eight layers of drift tubes and covers an  $\eta$  range of  $|\eta| < 2.7$ . The inner-most layer of the MDT only covers up to an  $\eta$  range of  $|\eta| < 2.0$ . In the  $\eta$  range between  $2.0 < |\eta| < 2.7$ , the Cathode Strip Chamber (CSC) replaces the MDT inner layer.

The drift tubes of the MDT function in the same manner as the straw tubes of the TRT in the inner detector. The muon ionizes the gas inside the tube and frees electrons. These electrons drift to the central wire of the drift tube because of the voltage difference between the central wire and the tube wall. The arrival of the electrons creates a pulse of current that is registered as a hit. How drift tubes operate is discussed in more detail in section 2.2.1. The purpose of the MDT is to precisely

measure the coordinates of the muon flight path in the bending  $\eta$  direction. This measurement of the bending coordinate is used in the calculation of the momentum of the muon. The resolution of the MDT is  $80 \mu\text{m}$  per tube.<sup>2</sup>

The CSC replaces the inner MDT layer in the forward  $\eta$  ranges between 2.0 and 2.7. This is needed because in this section the expected density of muons exceeds the safe operational limits of the MDT.<sup>2</sup> The CSC is formed with multiwire proportional chambers. The chambers are formed with strips of cathode capacitor plates on either side and a row of anode wires sandwiched in between. As a charged particle flies through the chamber it will ionize the gas in the chamber, freeing electrons and positively charged ions. The free electron will drift along electric field lines to the nearest wire and the ions will drift to the cathode plates strips. Different electrons may end up in different wires as the ionization area has some spread and different ions on different strips. The CSC then regresses the position of the muon from the proportions of signal in each strip. The structure of the CSC is show in figure 2.9.

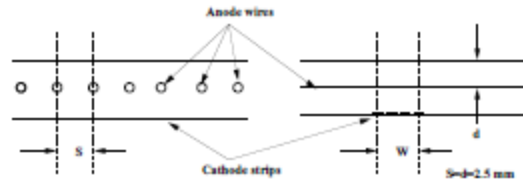


**Figure 2.9:** Diagram of a plane in the ATLAS Cathode Strip Chamber. (Taken from<sup>2</sup>)

The wires are arranged in the radial direction. This allows the wires to measure the  $\phi$  coordinate of the muon. On one side, the cathode strips are arranged parallel to the wire to complement the measured  $\phi$  coordinate of the muon and to reduce noise levels. On the other side, the cathode

strips are arranged transverse to the wires to measure the  $\eta$  coordinate of the muon. The resolution achieved by the CSC is  $40\text{ }\mu\text{m}$  in the bending  $\eta$  plane and about  $5\text{mm}$  in the transverse  $\phi$  plane. The difference is because the  $\eta$  coordinate is measured by the cathode strips and the  $\phi$  coordinate is measured by the wires.<sup>2</sup>

The RPC and TGC are trigger chambers with the goal of quickly measuring the position of the muon. The RPC chamber is formed by two orthogonal planes of cathode and anode strips. The gas in between the planes is chosen such that the gas sparks when a muon passes through. The sparking allow near-instantaneous detection of muons instead of waiting for the electrons and ions to drift onto the plates. The two orthogonal planes measure both the  $\eta$  and  $\phi$  coordinates of the muon track. The RPC extends out to an  $|\eta|$  of 1.05 and covers the barrel of the detector. The TGC is a multiwire proportional chambers and operates similarly to the CSC. The TGC covers the  $|\eta|$  range between 1.05 and 2.7 and covers the endcaps of the detector. However, the TGC can only trigger up to an  $|\eta|$  of 2.4. The trigger system and software is described in section ??.

The MDT can only measure the  $\eta$  coordinate and not the  $\phi$  coordinate of the muon. To compensate for this, the MDT chamber hits are matched to the respective RPC or TGC chamber hits and uses the  $\phi$  coordinate of the trigger chamber as the second coordinate of the hit. If more than one muon passes through an MDT and trigger chamber pair then there is no unambiguous method to match the hits. Therefore the muon density in the MDT chambers must be low. Fortunately, simulations show that the number of muons that reach the muon spectrometer with  $P_T > 6\text{ GeV}$  is about  $6 * 10^{-3}$  per beam-crossing, corresponding to about  $1.5 * 10^{-5}$  per chamber.<sup>2</sup> Assuming uncorrelated tracks, the probability of finding more than one track in any MDT/trigger chamber pair

is very small.<sup>3</sup> If two muons do traverse the same chamber, then the corresponding inner detector tracks of the muons are used to resolve the ambiguity.

The hits recorded by the muon spectrometer detectors are reconstructed into the track of the flight path of the muon. The muon track is then matched to the inner detector track of the muon by the ATLAS reconstruction software MuID and STACO. This forms one complete combined muon track that traverses the whole ATLAS detector. The uncertainty of the momentum measurement is inversely related with the length of the track. Therefore, the long length the combined muon track serves to give precise measurements of the momentum of the muon.

# 3

## Object Reconstruction at ATLAS

# 4

## Monte Carlo Simulation of Physics

### Processes at ATLAS

Simulated event samples are used to model the signal and background processes in this analysis. A full list of the samples that are used is given in Appendix ??.

Process	Generator	fragm./hadron.	PDF set	UE Tune	Cross section order
SUSY Signal	MADGRAPH5_AMC@NLO	PYTHIA 8	NNPDF2.3	A14	LO
$t\bar{t}$	POWHEG-BOX v2	PYTHIA 6	CT10	PERUGIA 2012	NLO
Single top	POWHEG-BOX v2	PYTHIA 6	CT10	PERUGIA 2012	NLO
$W/Z$ +jets	SHERPA 2.2.1	SHERPA	NNPDF3.0NNLO	Default	NLO
Diboson	SHERPA 2.2	SHERPA	CT10	Default	LO
$t\bar{t} + V$	MADGRAPH5_AMC@NLO	PYTHIA 8	NNPDF3.0NNLO	A14	NLO

**Table 4.1:** Overview of the nominal simulated samples.

#### 4.1 SIGNAL MONTE CARLO GENERATION

For the stop signal, the matrix element (ME) of the hard scattering interaction are calculated using MADGRAPH5\_AMC@NLO. Up to two additional QCD partons are included in the ME calculation, making the total hard scattering process  $pp \rightarrow t\bar{t} + j + j$ . The ME calculation is performed to leading order accuracy (LO).

The stop decays are treated differently depending on the mass splitting between the stop and its decay products. The resulting decays are seen in the Feynman diagrams shown in figure 4.1.

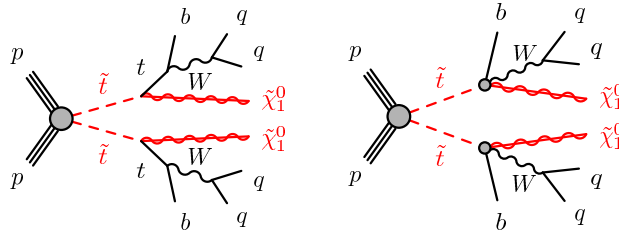


**Figure 4.1:** The decay topologies of the signal models considered depending on the mass splitting between  $\tilde{t}$  and  $\tilde{\chi}_1^0$ , a real top may be produced in the 2 body decay  $\tilde{t} \rightarrow t\tilde{\chi}_1^0$ , or virtually through a three body decay  $\tilde{t} \rightarrow bW\tilde{\chi}_1^0$

If  $m_{\tilde{t}} - m_{\tilde{\chi}_1^0} \geq m_T$ , then the top can be produced on shell. PYTHIA 8 perform 2 body  $\tilde{t} \rightarrow t\tilde{\chi}_1^0$  decay and subsequent decays of the top.  $m_T$  is set to 172.5 GeV. This process has the advantage



in that it is much computationally faster when compared to decaying the stops as part of the ME calculation. However it has the disadvantage of effectively assuming that the stop width is zero. The zero stop width assumption was found to differ from the true stop width case by less than 5 percent in the distributions of all relevant kinematic variables. The nominal stop width in the simplified model is 1/10 the width of the top and so the stop width represents only a small smearing on the distribution of  $m_T$  and  $E_T^{\text{miss}}$  compared to the one produced by the top width.

If  $m_{\tilde{t}} - m_{\tilde{\chi}_1^0} < m_T$ , then the top must be produced off shell. PYTHIA 8 cannot perform the 3 body  $\tilde{t} \rightarrow bW\tilde{\chi}_1^0$  or 4 body  $\tilde{t} \rightarrow bff\tilde{\chi}_1^0$  decays where the "f" stands for the fermions that result from a  $W$  decay. Instead we use MadSpin to perform the  $\tilde{t} \rightarrow bff\tilde{\chi}_1^0$  decay. MadSpin can perform 3 body and 4 body decays with off shell virtual particles as long as the decay are ultimately a series of 2 body decays. MadSpin performs the decays in a timely manner compared to calculating the decay within the ME. In this case, MadSpin cannot calculate the spin correlations between the two stops but this is not a problem because the stops are scalar particles so no spin correlations exist between the two.

In addition to the ME calculation and stop decays, the parton shower (PS) and hadronization of jets are simulated with PYTHIA 8 with the EVTGEN v1.2.0 program as afterburner. The matching between the matrix element and parton shower jets is performed with the CKKW-L prescription. The matching scale is set to 1/4 the mass of the stop.

The internal structure of the proton is modeled with the NNPDF3.0 NNLO parton distribution function (PDF) set with A14 set as the underlying event tuned parameters (UE tune).<sup>3</sup> The A14 tune optimizes over 10 parameters that vary the amount of ISR, FSR and multiple parton interactions. The variations are reduced to a 5 variable subset that is found to cover experimental observ-

ables.<sup>2</sup> Variable 1 mainly cover variation in the modeling of the underlying events. Variable 2 mainly cover variation in jet structure and variable 3a, 3b and 3c cover different variations of ISR and FSR production. All 5 variations are used to quantify the theoretical uncertainties associated with parton shower and multiple parton interactions and are added in quadrature.

Signal cross sections are calculated to next-to-leading order in the strong coupling constant with the resummation of soft gluon emission added to next-to-leading-logarithmic accuracy (NLO+NLL).<sup>3</sup> An envelope of cross section predictions is produced using different PDF sets and factorization and renormalization scales. The nominal cross section and the uncertainty are then taken from the median and 1 sigma fluctuations around the median within the envelope.

A 2D grid of signal samples is generated to cover the stop and neutralino mass phase space that we maybe sensitive to. Stop masses between 200 and 700 GeV are generated separated in  $m_{stop}$  by 50 GeV. For each Stop mass, five different  $\Delta m = m_{\tilde{t}} - m_{\tilde{\chi}_1^0}$  are simulated:  $\Delta m = m_{\tilde{t}} - 82.5$  GeV,  $m_{\tilde{t}} - 52.5$  GeV,  $m_{\tilde{t}} - 22.5$  GeV,  $m_{\tilde{t}} - 7.5$  GeV,  $m_{\tilde{t}} + 0.5$  GeV,  $m_{\tilde{t}} + 15.5$  GeV,  $m_{\tilde{t}} + 27.5$  GeV. An extra row of  $m_{\tilde{t}} = 225$  GeV samples is also produced to quantify the bound of sensitivity at low stop masses.

## 4.2 SM BACKGROUND MONTE CARLO GENERATION

### 4.2.1 STANDARD MODEL $t\bar{t}$ MONTE CARLO GENERATION

The nominal  $t\bar{t}$  samples are generated using POWHEG-BOXv2. The matrix element calculation is computed to NLO accuracy and includes the  $pp \rightarrow t\bar{t} + j$  process where the  $j$  is an one additional

emitted parton. The top quark mass is set to 172.5 GeV and the proton substructure is modeled by the NLO CT10 PDF set<sup>7</sup> for the hard scattering process. The hard scattering renormalization and factorization scales are set to the generator default of  $\sqrt{(m_T)^2 + (p_{T\bar{T}})^2}$ .

PYTHIA6 version 6.427 simulates the parton shower, hadronization and underlying event. We use the Perugia 2012 tune<sup>8</sup> and the corresponding leading order CTEQ6L1 PDF set<sup>9</sup> in PYTHIA6. The resummation damping factor or  $b_{damp}$  which is one of the parameters used by POWHEG to control the ME and PS matching and the amount of high- $p_T$  ISR/FSR, is set to  $m_T$ .

$t\bar{t}$  cross-sections are calculated to NNLO accuracy in the strong coupling constant with the resummation of soft gluon emissions added to NNLL accuracy using the TOP++v2.0 program.<sup>2</sup> Again an envelope of cross-sections is produced for different PDF sets including MSTW2008NNLO, CT10 NNLO and NNPDF2.3 NNLO. Variations in the renormalization and factorization scales, strong coupling constant, and top quark mass are also included in the envelope. The median of envelope is taken as the nominal  $t\bar{t}$  cross-section and the 1 sigma variation in the envelope is taken as the  $t\bar{t}$  cross-section uncertainty.

In addition to the total cross-section uncertainty, a number of  $t\bar{t}$  samples are produced to study the variation in the shapes of  $t\bar{t}$  kinematic distributions.

A radHi and radLo sample are produced to study the variation in the total amount of ISR/FST  $p_T$ . These samples are also produced with POWHEG+PYTHIA6 but have different renormalization and factorization scales (x0.5 to radHi and x2 to radLo). The radHi sample also has the  $b_{damp}$  parameter that help control the matching between PS and ME increased from the nominal  $m_{top}$  to x2  $m_{top}$ .

We study the variation of the parton shower simulation using a POWHEG+HERWIG++ ttbar sample. The hard scattering ME calculation has not changed from the nominal. The PDF used for the ME calculation is still NLO CT10 and the calculation is still performed with POWHEG-BOXV.2 with the  $b_{damp} = m_T$ . However the PS, fragmentation and hadronization is now performed with HERWIG++ with the CTEQ6L1 PDF set<sup>7</sup> with the UE-EE-5 parameter tune.

Variation in the hard scattering ME calculation are studied by comparing the nominal to a sample generated with SHERPA<sup>8</sup>. The same CT10 PDF set is used for sherpa and the nominal sample.

Non overlapping samples that are filtered according to  $E_T^{\text{miss}}$  are generated to increase statistics at high  $E_T^{\text{miss}}$  where our analysis resides. These samples are then merged to form a continuous distribution in  $E_T^{\text{miss}}$ .

#### 4.2.2 STANDARD MODEL SINGLE TOP MONTE CARLO GENERATION

Like the nominal ttbar sample, the nominal single top samples are also simulated with POWHEG-BOXV.2 and interfaced to PYTHIA6 for hadronization and parton showering, with CT10 PDF set and using the Perugia 2012 set<sup>9</sup> of tuned parameters.

Unlike the ttbar samples, single top samples are produced separately according to production channels. Three production channels exist including the s-channel, t-channel and the Wt channel. The largest contribution to our analysis comes from the Wt channel.

The NLO calculation of the  $pp \rightarrow Wt$  includes contributions from  $pp \rightarrow t\bar{t} \rightarrow T + b + W$ . However  $pp \rightarrow t\bar{t} \rightarrow T + b + W$  is already included in our simulation of ttbar and including it here would be double counting. We can subtract out the ttbar contribution at either the level of

amplitude (DR scheme) or at the level of matrix elements (DS scheme). Subtracting at the matrix element level also remove any potential interference between the single top  $pp \rightarrow Wt$  and  $t\bar{t}$ bar  $pp \rightarrow t\bar{t} \rightarrow \top + b + W$  processes. Subtracting at the amplitude level does not remove those interferences. Both schemes violates formal gauge invariance and there isn't a consensus on the correct procedure. We generate two sets of  $Wt$  channel single top samples with the two schemes. The nominal single top sample is generated with the DR scheme and another sample is generated with the DS scheme. We compare the difference between the two samples to quantify the uncertainty due to the single top and  $t\bar{t}$ bar interference terms.

RadHi and radLo samples are also produced for all channels to study the variation in single top ISR and FSR emissions. These samples are also produced with POWHEG+PYTHIA6 but have different renormalization and factorization scales ( $\times 0.5$  to radHi and  $\times 2$  to radLo). The radHi sample also has the  $h_{damp}$  parameter that help control the matching between PS and ME increased from the nominal  $m_{top}$  to  $\times 2 m_{top}$ .

We study the variation of the parton shower simulation using POWHEG+HERWIGG++ single top samples. The hard scattering ME calculation has not changed from the nominal. The PDF used for the ME calculation is still NLO CT10 and the calculation is still performed with POWHEG-BOXv.2 with the  $h_{damp} = m_{\top}$ . However the PS, fragmentation and hadronization is now performed with HERWIGG++ with the CTEQ6L1 PDF set<sup>3</sup> with the UE-EE-5 parameter tune.

#### 4.2.3 STANDARD MODEL $W + \text{jets}$ AND $Z + \text{jets}$ MONTE CARLO GENERATION

$W + \text{jets}$  and  $Z + \text{jets}$  are generated with the SHERPAv2.2.1 program. The matrix element are calculated for the vector boson (V) plus 0,1, and/or 2 additional partons at NLO accuracy and 3, and/or 4 additional partons at LO accuracy.

The ME calculation is merged with SHERPA parton shower according to the MEPS@NLO prescription. The proton substructure is modeled with the NNPDF3.0 NNLO PDF set and the PS tuning defined by SHERPA.

Systematic variations include a 7 point variation of the renormalization and factorization scales. The variations are used to quantify the theoretical uncertainty on our modeling of the  $W + \text{jets}$  and  $Z + \text{jets}$ .

The  $W + \text{jets}$  and  $Z + \text{jets}$  samples are generated in multiple non-overlapping slices of vector boson  $p_T$  and b-jets and c-jets presence. The samples are then merged later to form a continuous distribution covering all phase space. This allows us to generate higher MC statistics in the region of phase space that is relevant to our analysis, the high- $p_T$  region with the presence of b and/or c-jets.

#### 4.2.4 STANDARD MODEL $t\bar{t}+V$ MONTE CARLO GENERATION

$t\bar{t}+V$  where V is a  $W$  or  $Z$  boson samples are generated using MADGRAPH5\_AMC@NLO with the NNPDF3.0NNLO PDF set. The matrix element calculation is performed to NLO accuracy. The parton shower, fragmentation, and hadronization is simulated using PYTHIA 8 with the underlying event tune A14. Variations in the hard scattering ME calculation are studied by generating another

sample using SHERPA and comparing its results to the nominal sample. Variation in renormalization and factorization scales are also produced.

#### 4.2.5 STANDARD MODEL $t\bar{t} + \gamma$ MONTE CARLO GENERATION

$t\bar{t} + \gamma$  samples are generated using MADGRAPH5\_AMC@NLO with the NNPDF2.3LO PDF set. The matrix element calculation is performed to LO accuracy. The parton shower, fragmentation, and hadronization is simulated using PYTHIA 8 with the underlying event tune A14.

#### 4.2.6 STANDARD MODEL DIBOSON MONTE CARLO GENERATION

dibosons samples are generated with SHERPA v2.2 using CT10 PDF set.

### 4.3 DETECTOR SIMULATION

The detector simulation is performed using either GEANT4 or a fast simulation framework where the showers in the electromagnetic and hadronic calorimeters are simulated with a parameterized description and the rest of the detector is simulated with GEANT4. The fast simulation was validated against full GEANT4 simulation for several selected signal samples. All MC samples are produced with a varying number of simulated minimum-bias interactions overlaid on the hard-scattering event to account for multiple  $pp$  interactions in the same or nearby bunch crossing (pileup). The simulated events are reweighted to match the distribution in data. Corrections are applied to the simulated events to correct for differences between data and simulation for the lepton trigger and reconstruction efficiencies, momentum scale, energy resolution, isolation, and for the efficiency of

identifying jets originating from the fragmentation of  $b$ -quarks, together with the probability for mis-tagging light-flavor and charm quarks.



# 5

## General Analysis Strategy

### 5.1 GENERAL R-PARITY CONSERVING SUSY SEARCH STRATEGY

In most R-parity conserving SUSY searches, the sought after super-symmetric particle will mostly be produced in pairs. Each particle decays via a chain that ends in a stable, weakly interacting lightest super-symmetric particle (LSP). Because the LSP is weakly interacting, it will not be directly detectable by the ATLAS detector and must be inferred via momentum conservation as  $E_T^{\text{miss}}$ . The rest

of the products from the decay chain will be a series of standard model particles which can also be a combination of visible particles and invisible neutrinos.

All searches must distinguish between true SUSY processes and standard model physics processes that mimic the decay products of the target SUSY process. Traditional search methods often place special emphasis on identifying the LSP as this is the one part that is unique to the SUSY events. Practically this means searching for events with large amount of  $E_T^{\text{miss}}$ . The decay of the original SUSY particle generates large amounts of momenta for the LSP in regions with a large mass splitting between the original SUSY particle and LSP. Traditional searches therefore target the large amount of  $E_T^{\text{miss}}$  generated by the LSP can be used to identify SUSY events and is sensitive to regions where the SUSY particle and LSP decay products have large mass splittings.

## 5.2 GENERAL STRATEGIES IN COMPRESSED REGIONS

When mass splitting between the original SUSY particle and its decay products become small, there is little energy left over to generate momenta in those decay products. The result is a LSP with little momenta. The traditional strategy of searching for events with large amount of  $E_T^{\text{miss}}$  therefore fails in this region of parameter space. Any region where the decay products of the target particle have little momenta is considered a compress region.

For our specific analysis, the super-partner of the top, the s-top ( $\tilde{t}$ ) is expected to decay into a neutralino and top. When the  $\tilde{t}$  mass is close to that of the top mass plus the neutralino mass, both the top and neutralino gain very little momenta from the decay. The invisible neutralinos in turn

generate very little missing transverse energy. This leaves only the visible tops which are mimicked by standard model  $t\bar{t}$ bar. The same problem arises in many other searches if the mass splittings are small or at a particular value where the decay products gain very little momenta. However, the soft decay products can gain additional momenta if the entire system is boosted by strong initial state radiation (ISR).

The true goal of the searches have always been to identify the presence of the LSPs and use their presence to distinguish the target events from SM processes. Instead of targeting events with large amount of  $E_T^{\text{miss}}$ , we use the correlations between the LSP momenta and any ISR jets to identify LSPs in compressed regions. It is precisely because most of the momenta of the decay products are not coming from the decays but from the boost via strong ISR that the correlation between decay products and ISR tends to be extremely strong. In this way, we turn an experimental difficulty into a strength.

The relationship between the decay products and ISR also has an additional benefit of being model independent. This correlation is dictated solely by relativistic kinematics rather than the underlying QFT of any particular model. Essentially because the decay products gain little energy from the decay, the majority of the decay product's energy is coming from the kick of the ISR. Therefore, the direction and magnitude of the momenta of the decay products are determined mostly by two things, how heavy the decay products are and how hard they are kicked by the ISR. For the  $pp \rightarrow \tilde{t}\tilde{t} \rightarrow t\tilde{\chi}_1^0 \bar{t}\tilde{\chi}_1^0$  process, the relationship is given by equation 5.2. This ratio between the invisible decay products and the total ISR pt is called  $R_{\text{ISR}}$ .

$$E_T^{\text{miss}} \equiv p_{\tilde{\chi}_1^0, T}^{\text{lab}} \sim \gamma_{\tilde{t}}^{\text{lab}} \beta_{\tilde{t}}^{\text{lab}} E_{\tilde{\chi}_1^0, \tilde{t}}^{\tilde{t}} \sim \frac{p_T^{\text{ISR}}}{m_{\tilde{t}}} 2\gamma_{\tilde{t}}^{\tilde{t}} m_{\tilde{t}} \sim p_T^{\text{ISR}} \frac{2\gamma_{\tilde{t}}^{\tilde{t}} m_{\tilde{t}}}{2\gamma_{\tilde{t}}^{\tilde{t}} m_{\tilde{t}}} \sim p_T^{\text{ISR}} \frac{m_{\tilde{\chi}_1^0}}{m_{\tilde{t}}} \implies \quad (5.1)$$

$$R_{\text{ISR}} \equiv \frac{E_T^{\text{miss}}}{p_T^{\text{ISR}}} \sim \frac{m_{\tilde{\chi}_1^0}}{m_{\tilde{t}}}, \quad (5.2)$$

Figure 5.1 shows the correlations between the di-neutralino system, decay products of the  $\tilde{t}\tilde{t}^*$  system, and the ISR system before taking into account detector resolution effects. As you can see, the correlation between the ISR pt and the  $E_T^{\text{miss}}$  follows a straight line with a slope that is predicted by equation 5.2.

Notice that although the  $E_T^{\text{miss}}$  is directly proportional to the combined di-LSP pt, the ratio between  $E_T^{\text{miss}}$  and ISR pt is still proportional to the mass of a single LSP and original sparticle. This means that the back to back boost between the two original sparticles in this case the two  $\tilde{t}$  do not affect the correlation between the observable  $E_T^{\text{miss}}$  and ISR pt. Only the di-LSP pt is measurable because the LSPs are invisible and cannot be measured alone. Although the LSPs can individually gain momenta from the back to back boost of the sparticles against one another, the back to back momenta will exactly cancel resulting in zero measurable  $E_T^{\text{miss}}$  for the di-LSP system regardless of the back to back boost of the two sparticles. The di-LSP system only gains pt by inheriting it from the boost of di-sparticle system by the ISR system. The fraction of the momenta that is inherited by the di-LSP system from the pt of the di-sparticle system is exactly  $\frac{m_{\text{LSP}}}{m_{\text{sparticle}}}$  if the sparticle decay gives no additional momenta to the LSP. Because the di-sparticle pt must be equal and opposite that of the ISR pt by momenta conservation, the ratio between observable  $E_T^{\text{miss}}$  and ISR pt or  $R_{\text{ISR}}$

is given by 5.2. Figure ?? shows the correlation between the  $E_T^{\text{miss}}$  and ISR pt in simulation for the  $pp \rightarrow \tilde{t}\tilde{t} \rightarrow \tilde{t}\tilde{\chi}_1^0\tilde{t}\tilde{\chi}_1^0$  process for the case when the sparticle ( $\tilde{t}$ ) has mass 400 GeV and the LSP ( $\tilde{\chi}_1^0$ ) has mass 227 GeV and the top has mass 172.5 GeV. The preferred ratio between the  $E_T^{\text{miss}}$  and ISR pt is shown by a line with the slope that is exactly predicted by equation 5.2. Generating an offshell top far from the kinematic limit of  $m_{\tilde{t}}$  minus  $m_{\tilde{\chi}_1^0}$  can free up additional energy that can boost the LSP and spoil this correlation but the probability of this deviation is limited by the top width of 1.3 GeV.

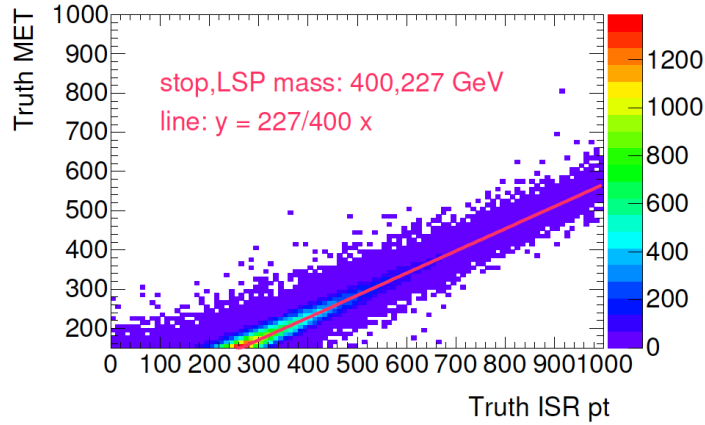


**Figure 5.1:** Distribution of di-neutralino pt, as represented by  $E_T^{\text{miss}}$ , vs total ISR pt before factoring in detector resolution for (400, 227)  $\tilde{t}, \tilde{\chi}_1^0$  mass point. The preferred ratio between the  $E_T^{\text{miss}}$  and ISR pt can be predicted using special relativity kinematics by equation 5.2. Deviation from this ratio is limited by the top width.

By constructing variables that capitalize on this correlation we are able to separate signal from standard model backgrounds which do not peak sharply in the  $R_{\text{ISR}}$  variable. On a practical note, the increase in center-of-mass energy from 8 to 13 TeV can mean up to an order of magnitude higher probability of emitting strong ISR. The 13 TeV dataset presents a golden opportunity to search for many new physics processes that need a boost from strong ISR in order to be detected.

6

# Recursive Jigsaw Reconstruction for Events with Missing Energy and Identifying ISR

Jets

## 6.1 INTRODUCTION TO RECURSIVE JIGSAW ALGORITHM ON EVENTS WITH $E_T^{\text{miss}}$

Every search involving missing energy has to contend with the fact that information on the invisible system is lost. The question of how to best fill the missing degree of freedom is a problem ubiquitous to all analysis that have  $E_T^{\text{miss}}$  especially when there exists multiple invisible particles in the event. The recursive jigsaw method aims to compartmentalize the lost information and gain the most from what information that is available.

Traditional edge variables such as  $\mathcal{M}_{T_2}$ , shown in equation 6.1, extremize over all possible kinematic configurations of the two invisible particles  $p_1$  and  $p_2$  to find some sort of kinematic edge. In effect,  $\mathcal{M}_{T_2}$  is an extremization over all possible configurations allowed by the ambiguity due to not being able to directly measure all aspects of the two invisible particles. However, over optimizing over a large phase space to pin down the unknown degrees of freedom can unintentionally destroy useful information.

$$\mathcal{M}_{T_2}^e \equiv \min_{\not{p}_1 + \not{p}_2 = \not{E}_T^{miss}} \left[ \max \{ m_T^2(p_{T1-}, \not{p}_1), m_T^2(p_{T1+}, \not{p}_2) \} \right] \quad (6.1)$$

The recursive jigsaw reconstruction (RJR) method also uses maximizations and minimizations to pin down the degrees of freedom left open by lost information. However, these extremizations are restricted to the specific location of the visible particle in its decay tree. Imagine a simple particle decay chain where  $a \rightarrow b c$  and then  $c \rightarrow 1 2$ . Recursive jigsaw would treat the situation differently if particle 1 was invisible compared to if particle  $b$  was invisible. To zeroth order, losing information about particle 1 affects only half the information on particle  $c$  which contains only half the information of particle  $a$ , but losing information on particle  $b$  directly affects half the information on particle  $a$ . Unlike traditional methods which extremizes over all possible configurations of the invisible particle, RJR compartmentalizes the lost information and extracts the maximum amount of information from events with missing energy.

RJR separates the event according to a predefined "decay tree." For compressed region, the most basic tree involve separating the event into sparticle and ISR systems and then further separating the sparticle system into visible and invisible parts. The decay tree is represented in figure. 6.1.

Each node in the decay tree represent a particular intermediate state or final state. RJR will classify all accepted objects into the different nodes according to a specific set of rules detailed in section 6.2. The rules overcomes combinatoric ambiguities and sets the unknown degree of freedoms associated with all weakly interacting final state particles according to maximizations and minimizations.

The decay tree can be as detailed as needed be, either attempting to resolve every branch in the



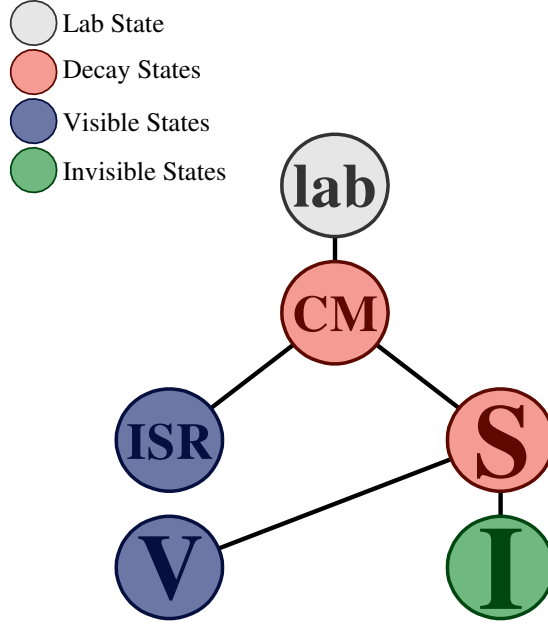


**Figure 6.1:** Decay Tree corresponding to ISR-assisted  $E_T^{\text{miss}}$  signal analysis strategy.

decay tree down to the level of the final state objects or forming generic aggregate intermediate states that have useful kinematics.

## 6.2 RECURSIVE JIGSAW METHOD OF IDENTIFYING INITIAL STATE RADIATION

In order to separate the event into an initial state radiation (ISR) system and a sparticle system, we first boost to the transverse center of mass frame of all accepted objects. This transverse center of mass frame has symmetries that we would like to exploit. The most important property of the transverse center of mass frame is that if the entire event is divided into two systems, these two systems must have equal and opposite transverse momenta. The other important point to note is that the lab frame and the transverse center of mass frame significantly differ only in cases when an energetic

object is not accepted. In other words, the two frames differ significantly only when the  $E_T^{\text{miss}}$  has a high probability of being miss reconstructed.

Once in the transverse center of mass frame, we find the thrust axis  $\vec{n}$  as defined in 6.3.

$$\vec{n} \equiv \max_{\vec{n}} \sum_i^{\text{jets}, E_T^{\text{miss}}} |p_T^i \cdot \vec{n}| \quad (6.2)$$

The thrust axis  $\vec{n}$  represents the axis that maximizes the amount of transverse momenta along it.

The back to back recoil between ISR and stops should represent the single largest back to back kick in events with strong ISR. As such, the thrust axis should approximate the direction of the back to back recoil between the stops and ISR. We divide the event into two hemispheres according to the thrust axis. The hemisphere containing the  $E_T^{\text{miss}}$  is identified as the sparticle hemisphere containing the decay products of the two stops. This is because we expect the sparticle hemisphere to contain the two  $\tilde{\chi}_1^0$ . The hemisphere opposite the direction of the  $E_T^{\text{miss}}$  is identified as the ISR hemisphere. All jets in the ISR hemisphere are considered to have originated from initial state radiation and all jets in the sparticle hemisphere are considered to have originated from one of the two stops.

The thrust axis is ensured to maximize the amount of back to back  $p_T$  because the total  $p_T$  of the event is zero in the transverse center of mass frame.

There is a mathematically equivalent second interpretation of this method of ISR identification. Since we are in the transverse center of mass frame, finding the thrust axis is the same as simultaneous maximizing the  $p_T$  of the sparticle and ISR systems. Since the total  $E_T$  of the event is a constant, then maximizing the  $p_T$  of the sparticle and ISR systems is identical to minimizing the masses of the

sparticle and ISR systems.

$$E_T = \sqrt{(m^{ISR})^2 + (p_T^{ISR})^2} + \sqrt{(m^{sparticle})^2 + (p_T^{sparticle})^2} \quad (6.3)$$

In this view, the ISR identification algorithm is an exclusive two jet clustering algorithm that seeks to simultaneously minimize the masses of both jets. Again the two jets are guaranteed to have back to back jet axis because we in the transverse center of mass frame.

### 6.3 PERFORMANCE OF INITIAL STATE RADIATION IDENTIFICATION ALGORITHM

We can check the performance of the thrust based initial state radiation (ISR) identification algorithm described in section 6.2 by plotting the ratio of reconstructed vs true ISR  $p_T$  in signal simulation. Figure 6.2 shows the distribution of the ratio of reconstructed vs true ISR  $p_T$  for 350 GeV stop mass and 172 GeV neutralino mass signal sample. Only events with fully hadronic stop decays and at least 400 GeV of true ISR  $p_T$  are accepted for this plot. Detector resolution effects on jets and  $E_T^{\text{miss}}$  are included when calculating the reconstructed ISR  $p_T$ .

A simple and currently popular form of ISR identification is simply the equating the highest  $p_T$  jet with the ISR system. This algorithm is represented by the distribution in red in figure 6.2. We see that the simple highest  $p_T$  jet algorithm often fails to capture the full  $p_T$  of the ISR system because the ISR system's energy is split between multiple jets. 20 to 50 percent of the ISR energy is not reconstructed about 40 percent of the time when we use the highest  $p_T$  jet ISR identification algorithm.

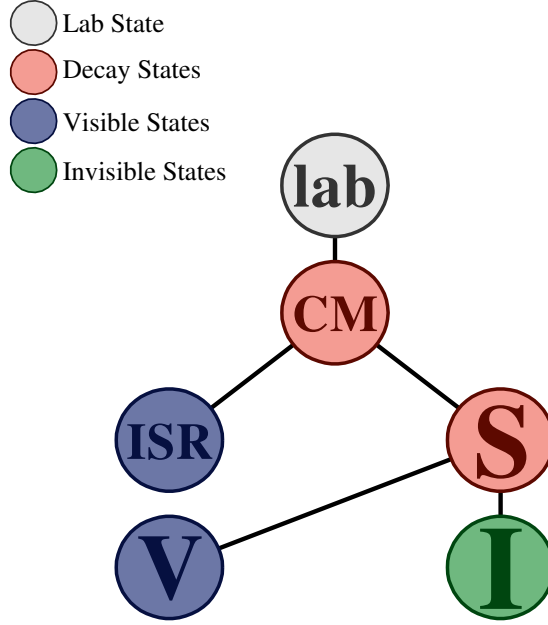


**Figure 6.2:** The distribution of the ratio of reconstructed vs true ISR  $p_T$  for the 350 GeV stop mass and 172 GeV neutralino mass signal sample. Only simulations with fully hadronic stop decays and at least 400 GeV of true ISR  $p_T$  are accepted. The red distribution is formed when the whole ISR system is equated to just the highest  $p_T$  jet. The blue distribution uses the thrust based ISR identification system.

In contrast the thrust based ISR identification system is able to capture the total  $p_T$  of the ISR system quite well. The fitted gaussian width of the blue peak is only 9 percent and this includes detector resolution effects. The gaussian mean is not centered about zero but instead is centered about 1.05. The reason for this is because a jet originating from a stop will occasionally go in the opposite direction as the  $E_T^{\text{miss}}$  and be misidentified as an ISR jet. The  $p_T$  of the misidentified sparticle jet tend to be small relative to the  $p_T$  of the ISR system as a whole. Therefore this misidentification shows up as a 5 percent bias in the reconstructed ISR  $p_T$ . Optimization of the ISR identification algorithm shows that this small bias does not impact the sensitivity of the search.

The non-gaussian tail in the blue distribution that exponentially decays to a reco vs true  $p_T$  ratio

of 1.5 is due to energetic ISR jets that go in the same direction as the  $E_T^{\text{miss}}$ . In these cases, the ISR jets that are in the same direction as the  $E_T^{\text{miss}}$  are miss-reconstructed as having originated from a stop. Only the ISR jets going in an opposite direction to the  $E_T^{\text{miss}}$  are reconstructed as ISR jets. The reconstructed ISR system fail to partially cancel the  $p_T$  of the oppositely facing jets and the reconstructed ISR system has a larger  $p_T$  then the true ISR  $p_T$ . However, this case is rare and the non-gaussian tail accounts for less than 15 percent of the events in blue distribution.

#### 6.4 KINEMATIC VARIABLES OF INITIAL STATE RADIATION AND SPARTICLE SYSTEMS

Once we separated the event into two hemispheres according the thrust axis as described in section 6.2 we can construct several variables that captures the kinematic properties of the two hemispheres. The important variables are listed below.

$N_{\text{btag}}^S$ : number of b-tagged jets associated with the sparticle hemisphere.

$N_{\text{jet}}^S$ : number of jets associated with the sparticle hemisphere.

$p_{T,b}^{o,S}$ :  $p_T$  of the leading b-tagged jet in the sparticle hemisphere.

$p_T^{\text{jet } 4, S}$ :  $p_T$  of the fourth highest  $p_T$  jet in the sparticle hemisphere.

$M_T^S$ : transverse mass of the whole sparticle system and  $E_T^{\text{miss}}$ .

$p_T^{\text{ISR}}$ :  $p_T$  of the ISR system

$\Delta\phi_{\text{ISR}, I}$ : angular separation in  $\phi$  of the ISR and the  $E_T^{\text{miss}}$  (evaluated in the transverse CM frame)

$R_{\text{ISR}}$ : Ratio between  $E_{\text{T}}^{\text{miss}}$  and  $p_{\text{T}}^{\text{ISR}}$  (evaluated in transverse CM frame)

$N_{\text{jet}}^{\text{S}}$  and  $N_{\text{btag}}^{\text{S}}$  quantify the jet multiplicity in the sparticle system.  $p_{\text{T},b}^{\text{o,S}}, p_{\text{T}}^{\text{jet 4,S}}, \mathcal{M}_{\text{T}}^{\text{S}}$  and  $p_{\text{T}}^{\text{ISR}}$  quantify the amount of energy in the sparticle and ISR hemispheres. Finally,  $\Delta\phi_{\text{ISR}, l}$  and  $R_{\text{ISR}}$  quantify the correlation between the ISR system and the  $E_{\text{T}}^{\text{miss}}$  in direction and magnitude. All of these variables will be used to separate signal from background in the signal region described in detail in section ??.

# 7

## Definitions of Reconstructed Physics

### Objects

The object definitions used follow the ATLAS recommendations and SUSY group standards for MC15c samples (SUSYTools-00-08-33 and AnalysisBase-2.4.23), details of which are given below.

## 7.1 ELECTRON DEFINITION

Electron candidates are selected using the `VeryLooseLH` definition and are required to have  $E_T = E_{\text{cl}} / \cosh \eta > 7 \text{ GeV}$  and to fall within  $|\eta_{\text{cl}}| < 2.47$ , where  $E_{\text{cl}}$  and  $\eta_{\text{cl}}$  are the energy and pseudo-rapidity of the electron candidate cluster, respectively<sup>3</sup>. Currently, electrons falling in the so-called “crack” region ( $1.37 < |\eta| < 1.52$ ) and satisfying the `VeryLooseLH` criteria are considered electron candidates.

Table 7.1 summarizes the electron definition criteria and specifies the angular distance for which an electron overlapping with a jet is rejected (see section 7.6).

**Table 7.1:** Electron selection criteria. The overlap removal is described in more detail in section 7.6.

Cut	Value
Acceptance	$p_T > 7 \text{ GeV},  \eta_{\text{clust}}  < 2.47$
Quality	<code>VeryLooseLH</code>
Isolation	<code>Gradient Loose</code>
Overlap: $e$ rejected if	$0.2 < \Delta R(e, \text{jet}) < 0.4$

## 7.2 MUON DEFINITION

In order to be accepted, muon candidates must pass the `Loose` selection criteria, have  $p_T > 6 \text{ GeV}$ , and fall within  $|\eta| < 2.7$ .

Table 7.2 summarizes the muon definition criteria and specify the angular distance for which a muon overlapping with a jet is rejected (see section 7.6).



**Table 7.2:** Muon selection criteria. The overlap removal is described in more detail in section 7.6.

Cut	Value
Acceptance	$p_T > 6 \text{ GeV},  \eta  < 2.7$
Quality	Loose
Overlap: $\mu$ is rejected if	$\Delta R(\mu, jet) < 0.4$

### 7.3 JET DEFINITIONS

#### 7.3.1 CALORIMETER JETS

Jets are reconstructed from topological clusters using the anti- $k_t$  jet algorithm<sup>2</sup> with a distance parameter of  $R = 0.4$  and full four-momentum recombination. The `AntiKt4EMTopo` jet collection is used, and global sequential calibration is enabled. Area-based corrections are also applied. All jets must have  $p_T > 20 \text{ GeV}$  with no  $\eta$  requirement to be considered in the analysis. Jets that pass this loose selection are considered when resolving overlapping objects and determining if the event should be vetoed due to bad quality jets. After the overlap removal and jet quality cuts, jets are required to have  $p_T > 20 \text{ GeV}$  and  $|\eta| < 2.8$  to be considered in the analysis. In addition to the  $\eta$  and  $p_T$  requirement a jet vertex tagger<sup>3</sup> value greater than 0.59 is required, corresponding to a 92% efficiency for jets originating from the hard scatter event and a 2% fake rate from pileup jets, if the jet has  $|\eta| < 2.4$  and  $p_T < 60 \text{ GeV}$ . This requirement helps to reduce sensitivity to pileup jets.

### 7.3.2 $b$ -TAGGED JETS

A subset of the baseline jets in the event are identified as originating from the decay of a  $b$ -quark by requiring they pass the MV2c10 jet tagger and are within the tracker acceptance with  $|\eta| < 2.5$ . The  $(\text{MV2c10} > 0.6459)$  operating point is used, which corresponds to a  $\sim 77\%$   $b$ -tagging efficiency. Events in the signal region must contain at least one  $b$ -tagged jet. The  $b$ -tagging efficiencies and mistag rates have been measured by the Flavour Tagging group. A correction scale factor, parameterized in  $\eta$ ,  $p_T$  and jet flavor, has been calculated by this group and applied to all jets in Monte Carlo samples<sup>3</sup>.

## 7.4 $E_T^{\text{miss}}$ DEFINITIONS

### 7.4.1 CALORIMETER-BASED $E_T^{\text{miss}}$

The calorimeter-based  $E_T^{\text{miss}}$  is calculated from an object-based algorithm. The  $E_T^{\text{miss}}$  is recalculated with the object definitions above. Baseline muons, electrons, and jets after overlap removal are used in the  $E_T^{\text{miss}}$  recalculation performed within SUSYTools. An extra term is added to account for soft energy in the event that is not associated to any of the selected objects. This soft term is calculated from inner detector tracks with  $p_T > 400$  MeV matched to the primary vertex to make it more resilient to pileup contaminations.

#### 7.4.2 TRACK-BASED $E_T^{\text{miss}}$

The  $E_T^{\text{miss}}$  derived from the sum of the transverse momenta of the tracks in the event ( $E_T^{\text{miss,track}} = -\sum_i^{\text{tracks}} p_T^i$ ). In the 2012 analysis, the azimuthal angle between this and the calorimeter-based  $E_T^{\text{miss}}$  was an effective discriminant against events with fake  $E_T^{\text{miss}}$ . The  $E_T^{\text{miss,track}}$  is rebuilt using the muons, electrons, and jets, similar to the  $E_T^{\text{miss}}$ .

### 7.5 PHOTON DEFINITION

The photon reconstruction is only considered in the photon control region. Photon candidates are obtained and calibrated using `GetPhoton` function in `SUSYTools`. A signal photon must pass the selection requirements that are described in Table 7.3.

**Table 7.3:** Photon selection criteria.

Cut	Value
Acceptance	$p_T > 130 \text{ GeV},  \eta  < 2.37$
Quality	Tight
Isolation	FixCutLoose

The  $p_T$  requirement is to ensure that the event is on the plateau of the photon trigger `HLT_g120_loose`.

### 7.6 RESOLVING OVERLAPPING OBJECTS

In the case of candidate objects overlapping with each other, all but one object must be removed from the event. The distance metric used to define overlapping objects is  $\Delta R = \sqrt{\Delta\phi^2 + \Delta\eta^2}$ . The

baseline SUSYTools overlap removal provided by the SUSY group is applied with an additional overlap removal applied to objects that survive the baseline. The SUSYTools baseline overlap removal is:

- If an electron and jet are located with  $\Delta R < 0.2$  consider the object an electron and remove the jet unless the jet is b-tagged (using the 85% working point rather than the 77% working point used in the signal regions) in which case the jet is kept and the electron is removed.
- If a muon and jet are located with  $\Delta R < 0.4$ , consider the object a jet and remove the muon. Unless the object has less than three tracks (with  $p_T > 500$  MeV), then the jet is removed while the muon is kept.
- If an electron and jet are located with  $0.2 \leq \Delta R < 0.4$ , consider the object a jet and remove the electron.

# 8

## Event Selections and Collision Data

### Samples

#### 8.1 DATA PERIODS AND GOOD RUN LIST

The dataset analysed in this search corresponds to the data collected by the ATLAS experiment in 2015 and 2016 from the LHC  $pp$  collisions at a centre-of-mass energy,  $\sqrt{s}=13$  TeV. This dataset corre-

spends to an integrated luminosity of  $36.46 \pm 0.07 \text{ fb}^{-1}$  of good-quality data as given by the final good run list (GRL)

`data15_13TeV.periodAllYear_DetStatus-v79-repro20-02_DQDefects-00-02-02_PHYS_StandardGRL_All_Good_25ns.xml`.

The newest GRL for 2016 data,

`data16_13TeV.periodAllYear_DetStatus-v83-pro20-15_DQDefects-00-02-04_PHYS_StandardGRL_All_Good_25ns.xml`,

The baseline trigger used for the signal selection is a  $E_T^{\text{miss}}$ -only trigger. For the data recorded in 2015 the lowest unscaled trigger with best turn-on curve `HLT_xe70_tc_lcw` was chosen; for the 2016 data the `HLT_xe90_mht_L1XE50` (period A-D<sub>3</sub>), `HLT_xe100_mht_L1XE50` (period D<sub>4</sub>-F<sub>1</sub>), `HLT_xe110_mht_L1XE50` (period F<sub>2</sub> and onward) are used.

## 8.2 EVENT PRESELECTION

In addition to the trigger requirements, several event cleaning and basic selection cuts must be passed for events to be considered for the signal region.

**Cut 1** For data samples only, events must be in the Good Runs List (GRL). The GRL for data 2015

is `data15_13TeV.periodAllYear_DetStatus-v79-repro20-02_DQDefects-00-02-02_PHYS_StandardGRL_All_Good_25ns.xml`.

The GRL for data 2016 is `data16_13TeV.periodAllYear_DetStatus-v83-pro20-15_DQDefects-00-02-04_PHYS_StandardGRL_All_Good_25ns.xml`.

The total luminosity that corresponds to these GRLs is  $36.46 \text{ fb}^{-1}$ .

**Cut 2** For data samples only, cleaning from noise bursts and possible incomplete events. Events

must have `larError == 0`, `tileError == 0`, `SCT error == 0`, and `coreFlags & 0x4000 == 0` to reject incomplete events due to the TTC reset procedure.

- Cut 3 The event must pass the (lowest unprescaled)  $E_T^{\text{miss}}$  trigger. For the 2015 data the HLT\_xe70\_mht\_L1XE50 is used. For the 2016 data the HLT\_xe90\_mht\_L1XE50 (period A-D<sub>3</sub>), HLT\_xe100\_mht\_L1XE50 (period D<sub>4</sub>-F<sub>1</sub>), HLT\_xe110\_mht\_L1XE50 (period F<sub>2</sub> and onward) are used.
- Cut 4 A reconstructed primary vertex must exist.
- Cut 5 Events must not contain any “Bad Jets” with  $p_T > 20$  GeV (at any  $\eta$  range). Details are given in<sup>3</sup>.
- Cut 6 The event must not contain any cosmic muons.
- Cut 7 The event must not contain any bad muons.
- Cut 8 Lepton veto. The event must contain exactly 0 baseline electron candidates and 0 baseline muon candidates with  $p_T > 7$  GeV and  $p_T > 6$  GeV, respectively.
- Cut 9 The leading two jets must have  $p_T > 80$  GeV, and the third- and fourth-leading jets must have  $p_T > 40$  GeV.
- Cut 10 The event must have  $E_T^{\text{miss}} > 250$  GeV.
- Cut 11 The event must contain at least four jets.
- Cut 12 The  $\Delta\phi$  between the leading two jets and the  $E_T^{\text{miss}}$ ,  $|\Delta\phi(\text{jet}^{\text{O.I.}}, E_T^{\text{miss}})|$ , must be greater than 0.4.
- Cut 13 The  $E_T^{\text{miss,track}}$  must be greater than 30 GeV.

Cut 14 The  $\Delta\phi$ , between the calo  $E_T^{\text{miss}}$  and the  $E_T^{\text{miss,track}}$ ,  $\left| \Delta\phi \left( E_T^{\text{miss}}, E_T^{\text{miss,track}} \right) \right|$ , must be smaller than  $\pi/3$ .

Cut 15 At least one b-tagged jet at the 77% working point is required.

Requirements 8 – 15 above are also summarized in Table ?? for convenience. A cutflow comparison on simulated events (for various SUSY1 xAOD signal and background samples) has been performed using independent code bases; many groups have achieved exact agreement. This serves as a technical validation.



# 9

## Signal Region Definition

### 9.1 PHYSICAL INTUITION ON HOW SIGNAL REGION SELECTIONS REJECT SM BACKGROUND

The kinematic selection in the signal region is designed to reject SM  $t\bar{t}$  events while retaining signal. After the zero lepton preselection, single hadronic tau and single lepton  $t\bar{t}$  makes up 95 percent of the  $t\bar{t}$  background because fully hadronic  $t\bar{t}$  generates no neutrinos and therefore  $E_T^{\text{miss}}$ . Because we select for events with least 250 GeV of  $E_T^{\text{miss}}$ , the top that decays leptonically must

be boosted. The leptonic top can gain boost by recoiling against the other hadronic top in a back to back fashion. Alternatively both tops can be boosted by strong initial state radiation. A detailed description of the  $t\bar{t}$  background and these two distinct populations is given in section 10.2.

90 percent of all  $t\bar{t}b\bar{a}$  events after pre-selection belong to the two tops back to back population. It is simply easier to boost one top against the other instead of having to both tops with additional strong initial state radiation. At the same time, the kinematics of the two tops back to back  $t\bar{t}b\bar{a}$  population is very different from those of the signal. This means we are able to reject the majority of the two tops back to back population without losing too much signal.

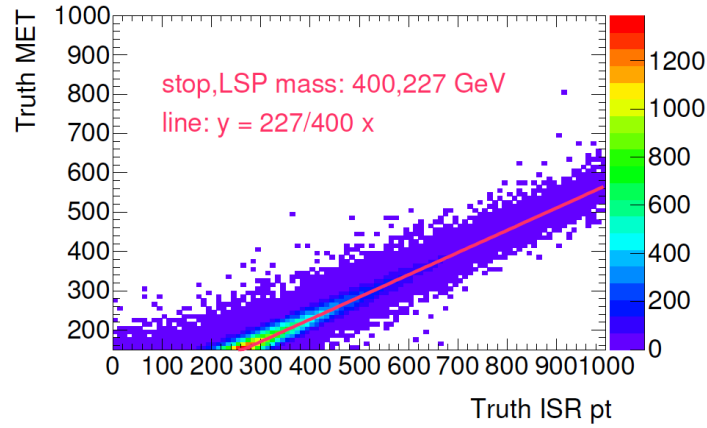


**Figure 9.1:** Basic depiction of the kinematics of the two  $t\bar{t}b\bar{a}$  populations and stop plus strong ISR events after 0 lepton pre-selection

Figure 9.1 shows examples of the three different populations lined up along their thrust axis with the hemisphere containing the  $E_T^{\text{miss}}$  in the upper half. The hemisphere with the  $E_T^{\text{miss}}$  contains significantly more jets and a total higher energy in signal than the  $t\bar{t}b\bar{a}$  two tops back to back population. The signal has 6 jets originating from the two hadronic tops in the hemisphere with  $E_T^{\text{miss}}$  instead

of only a single leptonic top in the  $t\bar{t}$  back to back population. The  $t\bar{t}$  with strong ISR population looks more signal like as it has higher jet multiplicity and energy in the  $E_T^{\text{miss}}$  hemisphere however, it still has less total energy than that of signal.

By cutting on the jet multiplicity and total energy in the hemisphere with  $E_T^{\text{miss}}$  we are able to reject 98 to 99 percent of  $t\bar{t}$  events which already passed preselection but have less than 400 GeV of true ISR pt. Acceptance of  $t\bar{t}$  events increase with high ISR pt but only asymptotically. Even at 1200 GeV of true ISR pt, a  $t\bar{t}$  event which already passed zero lepton preselection only has a 35 percent chance of passing the additional signal region selection.

After 0 lepton preselection, the signal to background ratio is 1 to 40 for a stop mass of 400 GeV. After signal region selection we get an around 2 to 1 signal to background ratio for the same mass point. This resounding success in eliminating background can largely be attributed to the signal region selection's efficiency in eliminating the dominant back to back  $t\bar{t}$  population and significantly reducing the lesser  $t\bar{t}$  plus strong ISR population all the while retaining most of signal.

At the same time, the same kinematic selections on jet multiplicity and total energy is also difficult for sub-dominant backgrounds such as  $W$ +jets,  $Z$ +jets, single top and QCD multijet to satisfy. In general it is difficult for these other processes to produce such high jet multiplicity and total energy in the same half of the event as the  $E_T^{\text{miss}}$ . Processes such as  $W$ +jets and  $Z$ +jets normally have the  $E_T^{\text{miss}}$  recoiling against other energetic jets. Therefore, most energetic jets in these processes tend to lie in the hemisphere opposite the  $E_T^{\text{miss}}$ . After signal selection, the dominate background is still standard model  $t\bar{t}$  which comprises over 90 percent of all backgrounds in the SR.

## 9.2 KINEMATIC VARIABLES DEFINITIONS

The kinematic variables used are reconstructed using the recursive jigsaw method. A detailed description of this method and variable defined can be found in section 6.2. In short, the recursive jigsaw method separates the event into two hemispheres according to the thrust axis. The thrust axis is the axis that maximizes the amount of back to back momenta along it and should approximate the direction of initial state radiation and sparticle back to back recoil in events with strong ISR. The hemisphere containing the  $E_T^{\text{miss}}$  is considered the "sparticle" hemisphere and the hemisphere opposite the  $E_T^{\text{miss}}$  is considered the ISR hemisphere. All jets in the sparticle hemisphere is considered to have originated from one of the stop decays. All jets in the ISR hemisphere is considered to be an ISR jet. The performance of this ISR identification algorithm can be found in section 6.3.

We construct variables that measure kinematic properties of both the ISR and sparticle hemispheres. Those variables are listed below:

$N_{\text{b-jet}}^{\text{S}}$ : number of b-tagged jets associated with the sparticle hemisphere.

$N_{\text{jet}}^{\text{S}}$ : number of jets associated with the sparticle hemisphere.

$p_{\text{T},b}^{\text{o},\text{S}}$ :  $p_{\text{T}}$  of the leading b-jet in the sparticle hemisphere.

$p_{\text{T}}^{4,\text{S}}$ :  $p_{\text{T}}$  of the fourth jet ordered in  $p_{\text{T}}$  in the sparticle hemisphere.

$\Delta\phi_{\text{ISR},E_T^{\text{miss}}}$ : angular separation in  $\phi$  of the ISR and the  $E_T^{\text{miss}}$  in the CM frame.

$p_{\text{T}}^{\text{ISR}}$ :  $p_{\text{T}}$  of the ISR system, evaluated in the CM frame.

$m_S$ : transverse mass between the whole sparticle system and  $E_T^{\text{miss}}$ .

$m_V/m_S$ : ratio of the transverse mass of the only the visible part of the sparticle system without  $E_T^{\text{miss}}$  and the whole sparticle system including  $E_T^{\text{miss}}$ .

$R_{\text{ISR}}$ : Ratio between invisible system ( $E_T^{\text{miss}}$  in CM frame) and  $p_T^{\text{ISR}}$

$N_{\text{btag}}^S$  and  $N_{\text{jet}}^S$  describes the jet multiplicity of the sparticle system.  $M_T^S$ ,  $p_T^{\text{jet } 4, S}$ , and  $p_{T,b}^{o,S}$  are all related to the total energy in the sparticle system.  $p_T^{\text{ISR}}$  corresponds to the total  $p_T$  of the ISR system. Finally  $R_{\text{ISR}}$  and  $\Delta\phi_{\text{ISR}, l}$  describe the correlation between the ISR system and  $E_T^{\text{miss}}$  in both direction and magnitude.

### 9.3 SIGNAL REGION KINEMATIC SELECTION

Kinematic Selections for Signal Region is defined in table 9.1.

The selections on  $N_{\text{jet}}^S$  and  $N_{\text{b-jet}}^S$  ensures that the hemisphere with  $E_T^{\text{miss}}$  has high amounts of jet multiplicity. This requirement is naturally satisfied in signal events because the two neutralinos naturally go in the same direction as the six jets resulting from the two stop decays. However this requirement is difficult for the two top back to back population to satisfy since only a single leptonic or hadronic tau top is in the same hemisphere as the  $E_T^{\text{miss}}$  in the hard process.

The ttbar plus strong ISR population is able to pass this selection as both the leptonic and hadronic tops are in sparticle hemisphere in this case. The result is the main background is ttbar plus strong ISR pt events pass after a requirement on the sparticle jet multiplicity and the  $p_T^{\text{ISR}} > 400 \text{ GeV}$  requirement. Signal to background ratio is around 1 to 5 after these selections. NEEDS PLOTS

**Table 9.1:** Signal region definitions, in addition to the preselection requirements presented in Table ??.

Variable	SRC-1	SRC-2	SRC-3	SRC-4	SRC-5
b-tagged jets			$\geq 1$		
$N_{b\text{-jet}}^s$			$\geq 1$		
$N_{\text{jet}}^s$			$\geq 5$		
$p_T^{\text{ISR}}$			$> 400 \text{ GeV}$		
$p_{T,b}^{\text{o},s}$			$> 40 \text{ GeV}$		
$p_T^{4,s}$			$> 50 \text{ GeV}$		
$m_S$			$> 300 \text{ GeV}$		
$\Delta\phi_{\text{ISR}, E_T^{\text{miss}}}$			$> 3.00$		
$R_{\text{ISR}}$	0.30-0.40	0.40-0.50	0.50-0.60	0.60-0.70	0.70-0.80

Distribution of different kinematic variables is shown after a requirement on  $p_T^{\text{ISR}}$ ,  $N_{\text{jet}}^s$ , and  $N_{b\text{-jet}}^s$  is shown in figure 9.2. The ttbar MC is normalized to a 1 lepton control region with the same selections on sparticle jet multiplicity, and  $p_T^{\text{ISR}}$ . All sub-dominant background are normalized to their respective CRs defined in section 10.3.

Next we make a requirement on the total energy of the sparticle system. The total transverse mass of the sparticle system  $m_S$  must be greater then 300 GeV and the  $p_T$  of the jet with 4th highest  $p_T$  in the sparticle system must be greater then 50 GeV.  $p_{T,b}^{\text{o},s}$  must also be greater then 40 GeV.

In general, the signal with two fully hadronic tops has more energy in the sparticle hemisphere then ttbar. The two top back to back recoil population is nearly eliminated by these selections. Of the ttbar events that passed 0 lepton preselection, less then 2 percent of ttbar events with true ISR pt

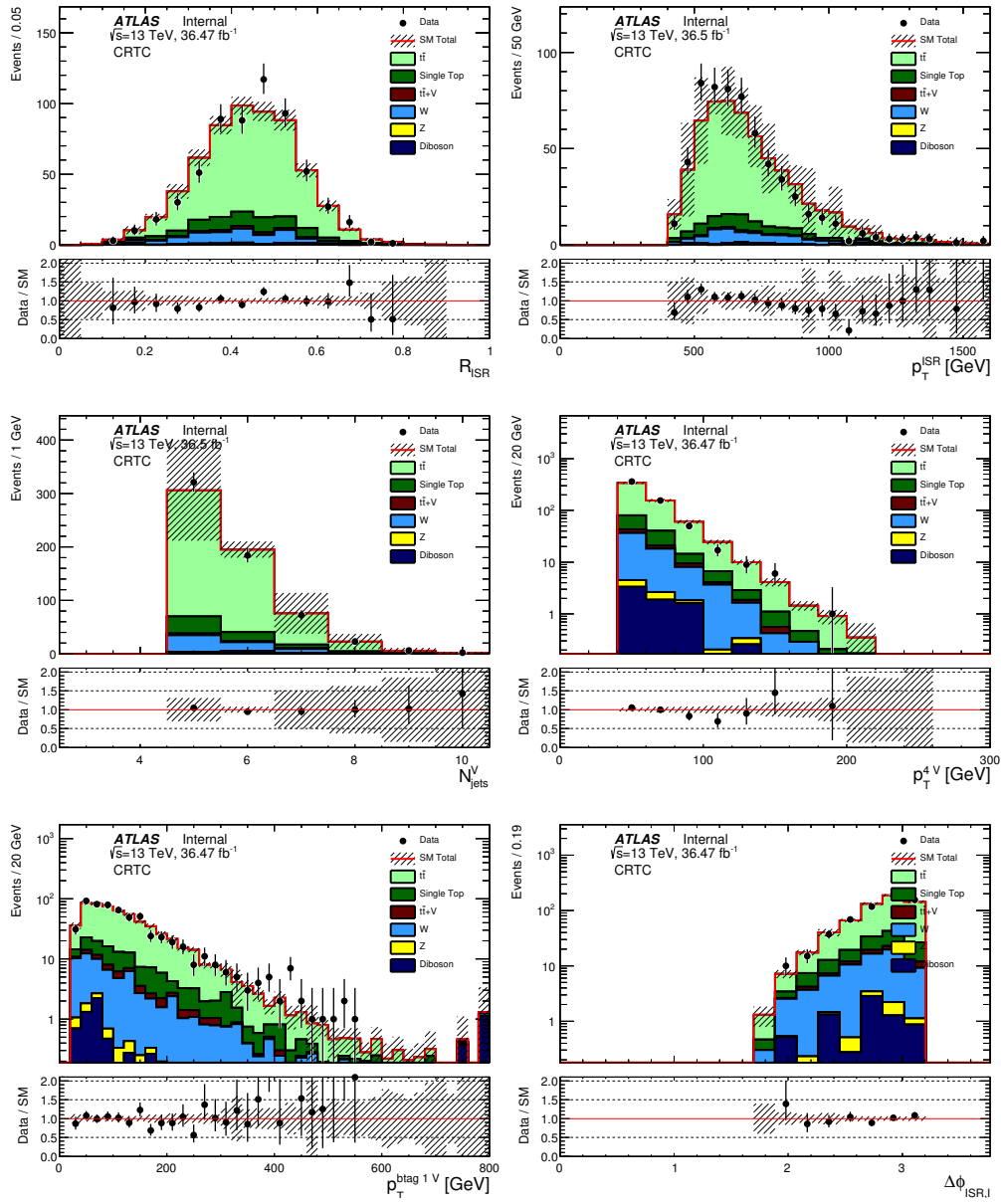


**Figure 9.2:** NEEDS PLOTS Distributions for 0 lepton preselection plus  $p_T^{\text{ISR}} > 400 \text{ GeV}$ ,  $N_{b\text{-jet}}^S \geq 1$  and  $N_{\text{jet}}^S \geq 5$  with  $36.47 \text{ fb}^{-1}$  of data. The ratio between data and MC is shown in the bottom panel. The hashed area in both the top and lower panel represent the uncertainty due to MC statistics and detector plus theoretical systematic uncertainties

less than 400 GeV pass these selections. Even for ttbar events with greater than 600 GeV of true ISR  $p_T$ , the selection is difficult to satisfy. Only 35 percent of the ttbar with greater than 600 GeV and also passed the 0 lepton preselection pass the addition requirement on sparticle jet multiplicity and energy. Signal to background ratio improves to around 1 to 2 after these selections.

Distribution of various kinematic variables after sparticle jet multiplicity,  $p_T^{\text{ISR}}$ , and sparticle energy requirement is shown in figure 9.3. The ttbar MC is normalized to a 1 lepton control region with the same selections on sparticle jet multiplicity,  $p_T^{\text{ISR}}$ , and sparticle energy requirement. All sub-dominant background are normalized to their respective CRs defined in section 10.3.

Lastly we make the a selections on correlations between the  $E_T^{\text{miss}}$  and ISR systems.  $\Delta\phi_{\text{ISR}, E_T^{\text{miss}}} > 3.0$  ensures the  $E_T^{\text{miss}}$  and ISR systems are back to back. The ISR system and  $E_T^{\text{miss}}$  must be nearly back to back in signal because the neutralino gains momenta mainly from ISR. SM ttbar on the other hand do not need to have back to back  $E_T^{\text{miss}}$  and ISR systems. Although the  $E_T^{\text{miss}}$  and ISR are also correlated for SM ttbar, the neutrino from the single lepton top decay gain some momenta from the top decay itself and can go in a different direction. The same logic holds for subdominant backgrounds such as  $W$ +jet and single top.

The distribution of  $\Delta\phi_{\text{ISR}, E_T^{\text{miss}}}$  with all previous selections on sparticle jet multiplicity and sparticle system energy applied is shown in figure 9.4. The ttbar MC is normalized to a 1 lepton control region with the same selections on sparticle jet multiplicity,  $p_T^{\text{ISR}}$ , and sparticle energy requirement. All sub-dominant background are normalized to their respective CRs defined in section 10.3.

After we get the final  $R_{\text{ISR}}$  distribution shown in figure 9.5. The ttbar MC is normalized to a 1 lepton control region defined in table 10.1. All sub-dominant background are normalized to their



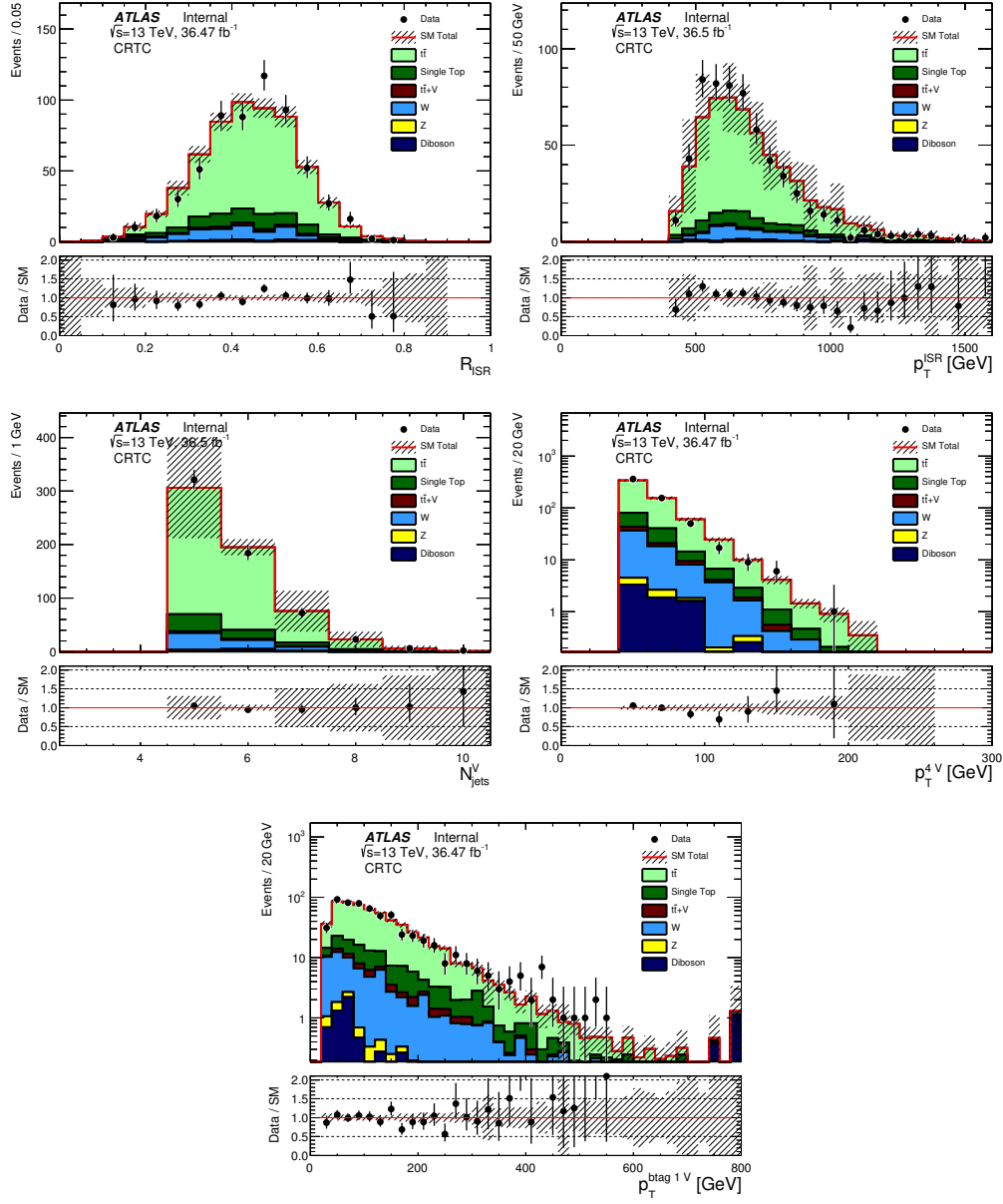


**Figure 9.3:** NEEDS PLOTS Distributions for 0 lepton preselection plus sparticle jet multiplicity,  $p_T^{\text{ISR}}$ , and sparticle total energy requirement with  $36.47 \text{ fb}^{-1}$  of data. The ratio between data and MC is shown in the bottom panel. The hashed area in both the top and lower panel represent the uncertainty due to MC statistics and detector plus theoretical systematic uncertainties

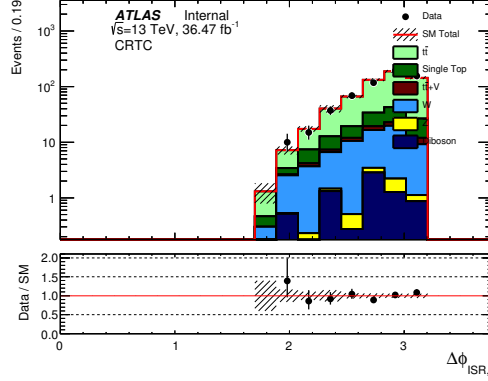


**Figure 9.4:** NEEDS PLOTS  $\Delta\phi_{\text{ISR},E_T^{\text{miss}}}$  distributions for 0 lepton preselection plus sparticle jet multiplicity,  $p_T^{\text{ISR}}$ , and sparticle total energy requirement with  $36.47 \text{ fb}^{-1}$  of data. The ratio between data and MC is shown in the bottom panel. The hashed area in both the top and lower panel represent the uncertainty due to MC statistics and detector plus theoretical systematic uncertainties

respective CRs defined in section 10.3.

This  $R_{\text{ISR}}$  distribution is then separated into 5 bins from 0.3 to 0.8. We expect to receive very little signal events in  $R_{\text{ISR}}$  below 0.3. At the same time, the region of  $R_{\text{ISR}}$  below 0.3 is dominated by QCD background and serves as a validation region for QCD multijet background.

Stop samples with different stop and neutralino masses will peak in different locations in  $R_{\text{ISR}}$  with a signal to background ratio of about 2 to 1 under the peak. The simultaneous fit to all five bins captures the feature of the signal peak in  $R_{\text{ISR}}$ .

#### 9.4 SIGNAL REGION EXPECTED YIELDS AND KINEMATIC DISTRIBUTIONS

The expected yields in the signal region is given in table 9.2. All backgrounds have been normalized to control regions defined in chapter 10. Signal yields for three example signal samples with stop,

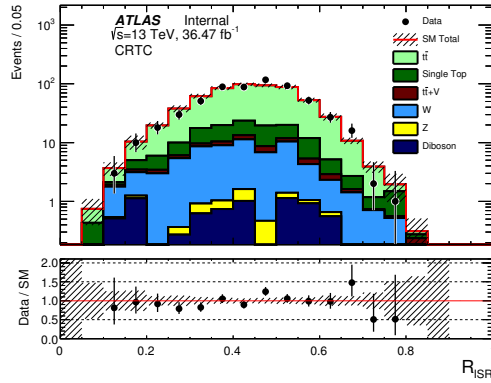


**Figure 9.5:** NEEDS PLOTS  $R_{\text{ISR}}$  distribution after signal region selection with  $36.47 \text{ fb}^{-1}$  of data. The ratio between data and MC is shown in the bottom panel. The hashed area in both the top and lower panel represent the uncertainty due to MC statistics and detector plus theoretical systematic uncertainties

neutralino masses of  $(300, 127 \text{ GeV})$ ,  $(400, 227 \text{ GeV})$ , and  $(500, 327 \text{ GeV})$  are also shown for comparison. In general between 1 to 1 or 2 to 1 signal to background ratio is achieved in the signal peak in  $R_{\text{ISR}}$ .

Plots of signal region distribution for select kinematic variables are shown in figure 9.6

## 9.5 SIGNAL REGION BACKGROUND COMPOSITION

The dominate background in all signal region bins is standard model pair produced tops ( $t\bar{t}$ ). The breakdown of background composition is given in table ??

$t\bar{t}$  accounts for 85 percent of all backgrounds in the signal region. The next most prevalent background is  $W$ +jets which can reach up to 15 percent in high  $R_{\text{ISR}}$  bins.

SRC <sub>1</sub>		SRC <sub>2</sub>		SRC <sub>3</sub>	
Z	$0.11 \pm 0.03$	Z	$0.43 \pm 0.09$	Z	$0.86 \pm 0.12$
dibosons	$0.04 \pm 0.04$	dibosons	$0.41 \pm 0.28$	dibosons	$0.24 \pm 0.21$
ttbar	$1.99 \pm 0.46$	ttbar	$16.01 \pm 1.58$	ttbar	$28.65 \pm 1.99$
singleTop	$0.09 \pm 0.06$	singleTop	$1.26 \pm 0.44$	singleTop	$0.96 \pm 0.17$
ttV	$0.03 \pm 0.04$	ttV	$0.23 \pm 0.09$	ttV	$0.39 \pm 0.18$
W	$0.46 \pm 0.23$	W	$0.59 \pm 0.13$	W	$1.38 \pm 0.27$
Total MC	$2.72 \pm 0.52$	Total MC	$18.94 \pm 1.67$	Total MC	$32.47 \pm 2.04$

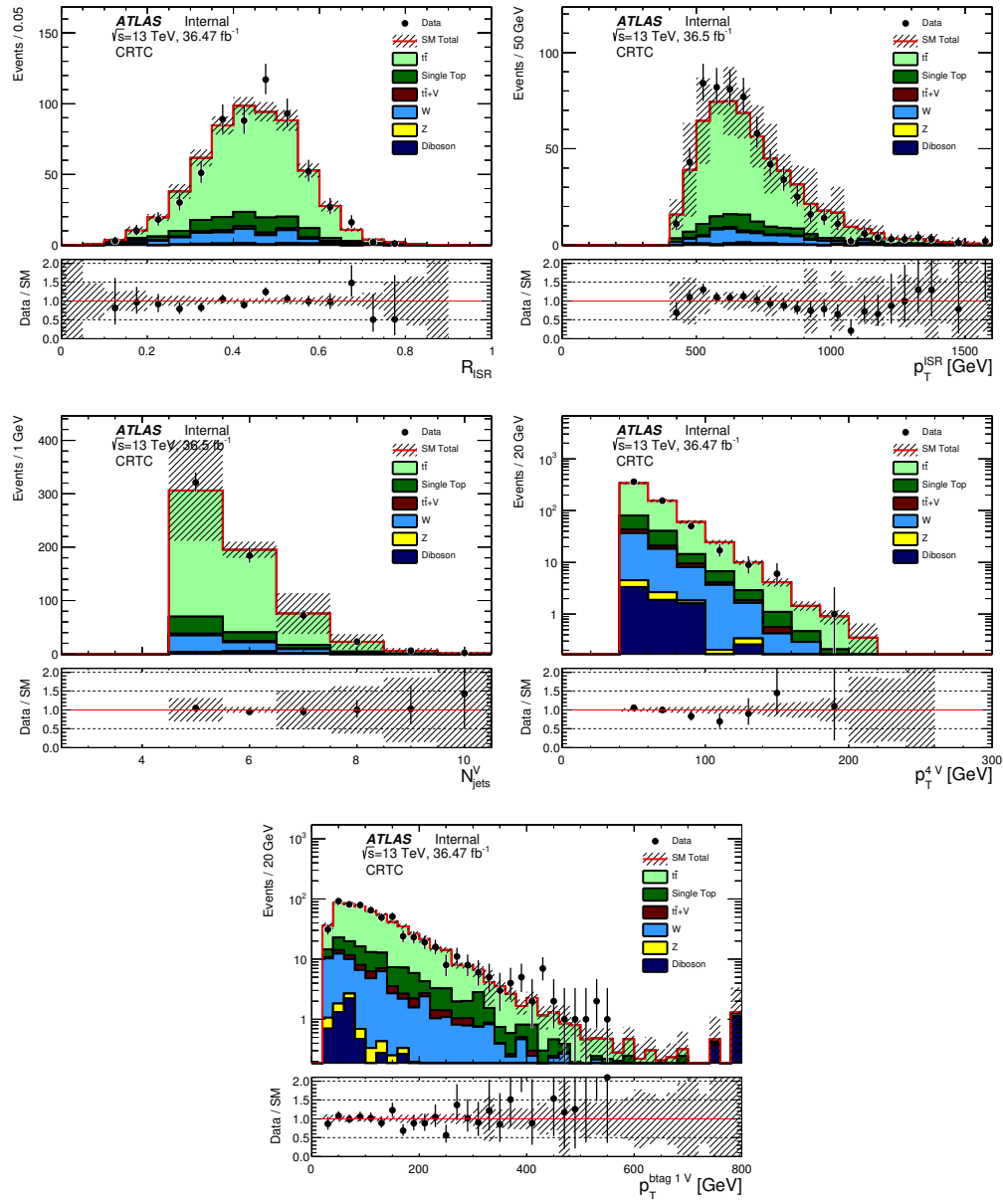
  

SRC <sub>4</sub>		SRC <sub>5</sub>	
Z	$0.71 \pm 0.14$	Z	$0.44 \pm 0.10$
dibosons	$0.49 \pm 0.41$	dibosons	$0.15 \pm 0.10$
ttbar	$21.07 \pm 1.54$	ttbar	$6.33 \pm 0.72$
singleTop	$1.00 \pm 0.39$	singleTop	$0.53 \pm 0.14$
ttV	$0.39 \pm 0.09$	ttV	$0.08 \pm 0.08$
W	$1.43 \pm 0.34$	W	$1.38 \pm 0.37$
Total MC	$25.09 \pm 1.69$	Total MC	$8.91 \pm 0.84$

**Table 9.2:** Signal Region expected discovery significance for select samples with 20% background systematic uncertainty.

**Table 9.3:** Standard Model Background Composition in the Signal Region ??.

$R_{\text{ISR}}$ Range	0.20-0.30	0.30-0.40	0.40-0.50	0.50-0.60	0.60-0.70	0.70-0.80
$t\bar{t}$						
W+jets						
Z+jets						
Others (dibosons+Single Top+QCD)						



**Figure 9.6:** NEEDS PLOTS Distributions for signal region selection. The ratio between data and MC is shown in the bottom panel. The hashed area in both the top and lower panel represent the uncertainty due to MC statistics and detector plus theoretical systematic uncertainties

# 10

## Standard Model Backgrounds

### 10.1 COMMON BACKGROUND ESTIMATION AND VALIDATION TECHNIQUES

We use both data and MC based background estimation technique for estimating background in the signal region. A common partially data driven technique is by using different control regions (CR) to directly measure the amount of background from data. Once we know the amount of background in the CR, we can then extrapolate to the signal region using MC predictions of the relative

amount of background in CR and SR.

The total amount of background is determined through a simultaneous fit to SR and all CRs. The background rate will be mainly constrained by the CRs because the CR contain many more events than the SR and is pure in specific types of background. A more detailed explanation of CR, SR and fits are covered in the statistical analysis section 12.2.

Aside from the fitting to control regions, we can get a simplified estimate of the amount of background in the SR through a simpler method. We can calculate the transfer factor and normalization factor defined in equation 10.1 and 10.2. This simplified result may slightly differ for the combined fit but should be similar as long as the CRs are well designed and consists mainly of a single type of background.

$$T = \frac{N_{MC}^{SR}}{N_{MC}^{CR}} \quad (10.1)$$

$$\mu_{MC} = \frac{N_{data}^{CR} - N_{non-ttbarMC}^{CR}}{N_{ttbarMC}^{CR}} \quad (10.2)$$

We normalize the ttbar MC in the ttbar CR to the amount of data with a normalization scale factor  $\mu$  defined in equation 10.2. We then apply the transfer factor to predict the amount of ttbar we expect to see in the SR. This is mathematically equivalent to simply normalizing the amount of ttbar MC in the SR by the scale factor derived in the CR because the transfer factor is just the relative rates of MC in the SR and CR.

We use control regions to estimate the dominant ttbar background and subdominant W+jet,

single top, and  $t\bar{t}V$  backgrounds.  $Z$ +jets and diboson backgrounds are estimated using MC alone.  $Z$ +jets and diboson contributions are less than 5 percent of all backgrounds in the SR and we allow for an additional 100 percent theory uncertainty for these two samples. Details on the  $t\bar{t}b\bar{a}$  background is found in section 10.2. Details on the treatment of each sub dominate background can be found in section 10.3. Finally QCD multijet background is estimated using the jet smearing method described in section 10.3.6.

## 10.2 DOMINANT BACKGROUND: STANDARD MODEL $t\bar{t}$

The dominant background in this analysis is standard model  $t\bar{t}b\bar{a}$ . Section 10.2.1 describes the two kinematically distinct populations of  $t\bar{t}b\bar{a}$  that exist after preselection. One  $t\bar{t}b\bar{a}$  population is also produced with strong initial state radiation and the other population does not have strong ISR.

Section ?? describes the signal selections used to remove the majority of  $t\bar{t}b\bar{a}$  background while retaining most of the signal. These selection targets the larger and kinematically different population of  $t\bar{t}b\bar{a}$  that does not have strong initial state radiation.  $t\bar{t}b\bar{a}$  with strong ISR appears more signal like and 90 percent of all  $t\bar{t}b\bar{a}$  backgrounds after signal region selection are  $t\bar{t}b\bar{a}$  events with at least 400 GeV of true initial state radiation. These same selections are also very effective at removing sub-dominate SM backgrounds such as  $W$ +jets and  $Z$ +jets.

Section 10.2.3 describes how we are able to directly measure the amount of  $t\bar{t}b\bar{a}$  background that is produced with strong initial state radiation in data using an one lepton control region. We avoid relying on theory predictions on the amount of ISR  $t\bar{t}b\bar{a}$  is expected to produce. In this way, the



control region allows us to minimize the amount of systematic uncertainties in the signal region.

After signal selection  $t\bar{t}$  still accounts for 85 percent of our background. 80 percent of the  $t\bar{t}$  has one top decay via a single hadronic tau and the other top decays fully hadronically. 15 percent of the  $t\bar{t}$  events decay via the single lepton channel where the lepton is an electron or a muon. The lepton becomes lost because either it has too low  $p_t$  to be reconstructed, removed because they were too close to another jet or is mis-reconstructed as a jet. The rest of the five percent composed of dileptonic or lepton and tau  $t\bar{t}$  events. Essentially no fully hadronic  $t\bar{t}$  survives the zero lepton selection because fully hadronic  $t\bar{t}$  do not make any hard neutrinos directly from the top decay. The 250 GeV  $E_T^{\text{miss}}$  selection removes all fully hadronic  $t\bar{t}$ .

#### 10.2.1 TWO KINEMATICALLY DISTINCT POPULATIONS OF $t\bar{t}$

Most  $t\bar{t}$  events has one top that decays leptonically and the other top decaying fully hadronically after zero lepton preselection. The leptonic top also produces a neutrino that satisfies the 250 GeV of  $E_T^{\text{miss}}$  requirement. In most cases, the lepton is a tau that decays hadronically and registers as jet in calorimeter instead of a lepton. In a smaller fraction of events a muon or electron is produced but the lepton is lost because of a number of reasons. For example, the lepton can have too low  $p_t$  to be reconstructed, or can be removed because they were too close to another jet or an electron is mis-reconstructed as a jet.

Regardless of the exact decay channel, a top decaying at rest cannot generate enough momenta for the neutrino to have 250 GeV of  $p_t$ . The top decaying via a tau or lepton, called the leptonic top, must therefore be boosted to have a high probability of satisfying the 250 GeV  $E_T^{\text{miss}}$  cut. The

leptonic top can gain this boost through one of two ways. Either the leptonic top recoils in a back to back fashion against the hadronic top or both tops recoil against strong ISR.

In both situations the axis of maximum back to back momenta, the thrust axis, contains important information. In the case where the leptonic is recoiling against the hadronic top, the thrust axis lines up along the two top's back to back recoil. In the case where both tops are boosted by strong ISR, the thrust axis lines up along the direction of the two tops' recoil against strong ISR. A basic representation of the kinematics of the two populations and the role of the thrust axis in each of them can be seen in figure 10.1.

One can clearly see that the two population has very different kinematics once we divide the event in half along the thrust axis.

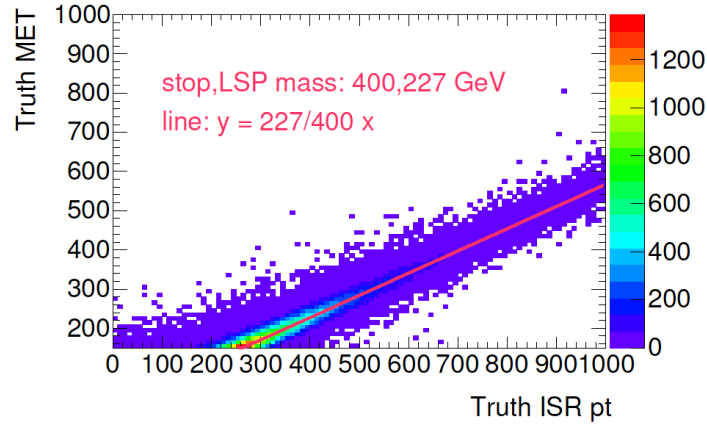


**Figure 10.1:** Basic depiction of the kinematics of the back to back  $t\bar{t}$ bar population and the  $t\bar{t}$ bar plus strong ISR population that exists after the zero lepton pre-selection.

### 10.2.2 PROPERTIES OF $t\bar{t}$ IN SIGNAL REGION

The  $t\bar{t}$  events that survives the signal region selection is almost completely  $t\bar{t}$  events also produced with strong initial state radiation. In the signal region, 90 percent of the  $t\bar{t}$  events have at least 400 GeV of ISR pt. The distribution of true ISR pt for  $t\bar{t}$  that survive the signal selections can be seen in figure 10.2.

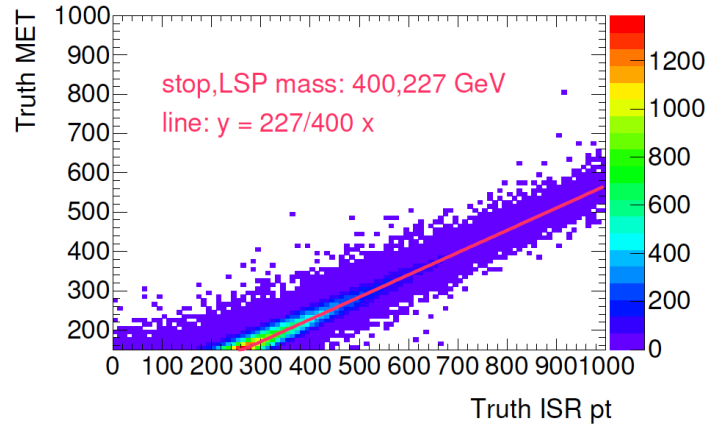


**Figure 10.2:** Distribution of true ISR pt for  $t\bar{t}$  that survive the signal selections

In terms of branching fractions, the majority of  $t\bar{t}$  branching fractions are to hadronic taus. 80 percent of the  $t\bar{t}$  has one top decay via a single hadronic tau and the other top decays fully hadronically. 15 percent of the  $t\bar{t}$  events decay via the single lepton channel where the lepton is an electron or a muon. The lepton becomes lost because either it has too low pt to be reconstructed, removed because they were too close to another jet or is mis-reconstructed as a jet. The rest of the five percent composed of di-leptonic or lepton and tau  $t\bar{t}$  events. Essentially no fully hadronic  $t\bar{t}$  survives the zero lepton selection because fully hadronic  $t\bar{t}$  do not make any hard neutrinos

directly from the top decay.

With such a large fraction of background coming from taus one might suspect setting up some sort of tau rejection. However we found that a rejection based on loose tau IDs did not improve sensitivity. The loss of signal was too large to justify the improvement in signal to background ratio. The high jet multiplicity in signal gives a high probability of false positives. Accepting mainly  $t\bar{t}b\bar{a}r$  decay to hadronic taus gives a large boost signal to background due to branching fractions alone. The two tops in signal events decay mainly through the fully hadronic channel. Fully hadronic decays accounts for 44 percent of all  $t\bar{t}b\bar{a}r$  decays. On the other hand, the  $t\bar{t}b\bar{a}r$  background mainly decay via hadronic taus which only accounts for about 10 of all  $t\bar{t}b\bar{a}r$  decays. We therefore gain a factor of 5 in signal to background ratio just by working in the zero lepton channel. This not only gains us a great boost in sensitivity in our signal region. It also allows us to design a  $t\bar{t}b\bar{a}r$  control region with very similar selections to the signal region but just in the single lepton channel. We can avoid high signal contamination in our control region because both signal and background are mainly coming from single lepton decays in the 1 lepton channel. As such, we no longer gain this factor of 5 in S/B based on branching fraction in the control region. The details of the  $t\bar{t}b\bar{a}r$  control region is described in section 10.2.3

### 10.2.3 PREDICTING THE AMOUNT OF $t\bar{t}$ IN SIGNAL REGION USING A ONE LEPTON CONTROL REGION

The  $t\bar{t}b\bar{a}r$  that populate the signal region is mainly  $t\bar{t}b\bar{a}r$  produced with strong initial state radiation as shown in section 10.2.2 and ???. A direct consequence of this is that our predictions for the amount

of background in our signal region is directly related to the amount of ISR/FSR in our ttbar MC. The next-to-leading order (NLO) MC simulations of ttbar gives upwards of 30 to 35 percent uncertainty in the amount of predicted ttbar background in the signal region (SR). This theoretical uncertainty would be our single largest uncertainty if we had to rely on theoretical calculations alone. Instead we directly measure the amount of ttbar that is produced with strong ISR in-situ directly from ATLAS data using an one lepton ttbar control region (ttbar CR). Using the ttbar CR we are able to reduce the ISR/FSR systematic uncertainty in the SR down to a manageable 10 percent in all signal regions.

The selections used to define the ttbar CR is defined in table 10.1. This control region is designed using the same sensitive variables as the SR definition to mimic the signal regions as close as possible while maintaining a high purity of the dominant background semi-leptonic  $t\bar{t}$ . The CR is defined in the 1 lepton channel where the lepton is a signal muon or signal electron. The lepton is included as a "jet" in the Jigsaw ISR algorithm and will be counted as a sparticle jet or an ISR jet depending on which hemisphere it falls. In this case the lepton is supposed to mimic the hadronic tau jet that exists in 80 percent of all ttbar events.

All variables used are defined in section 6.4. A cut of  $m_T(\ell, E_T^{\text{miss}}) < 80 \text{ GeV}$  is added to remove signal contamination and a  $\Delta R(b_{o,I}, \ell)_{\text{min}} < 2.0$  cut is added to increase ttbar purity and ensure orthogonality to the W+jets control region.

The  $\Delta\phi_{\text{ISR}, I} > 3.0$  is removed to increase CR statistics.  $\Delta\phi_{\text{ISR}, I}$  specifies the direction of neutrino relative to the direction of the ISR. A requirement on  $\Delta\phi_{\text{ISR}, I} > 3.0$  essentially selects only specific decay axis that the  $t\bar{t}$  decay can take place. Therefore removing this cut opens up more phase

**Table 10.1:** One-lepton  $t\bar{t}$ +ISR control region (ttbar CR) definitions. The same  $E_T^{\text{miss}}$  triggers as mentions in Table ?? are used.

Variable	1L 1b $t\bar{t}$ CR
1 Lepton Pre-Selection	true
Number of leptons	1
Number of $b$ -jets	$\geq 1$
$m_T(\ell, E_T^{\text{miss}})$	$< 80 \text{ GeV}$
$\Delta R(b_{o,1}, \ell)_{\min}$	$< 2.0$
$N_{\text{jet}}^S$	$\geq 5$
$N_{\text{btag}}^S$	$\geq 1$
$p_T^{4,S}$	$> 40 \text{ GeV}$
$p_T^{\text{ISR}}$	$\geq 400$

space that the tops can decay in the CR but does not change qualitative property that the  $t\bar{t}$  events in the CR must have strong initial state radiation.

The  $p_T^{\text{jet } 4, S} > 50 \text{ GeV}$  cut is relaxed to  $p_T^{\text{jet } 4, S} > 40 \text{ GeV}$  in order to increase statistics in the CR. The  $p_T^{\text{jet } 4, S}$  cut specifies the  $p_T$  of the 4th jet in the sparticle system. Loosening this cut increases statistic by allowing the 4th jet in the  $t\bar{t}$  decay to have softer  $p_T$  but does not change the hardness of  $> 400 \text{ GeV}$  ISR system. The  $p_T^{\text{jet } 4, S}$  cut can be correlated with ISR/FSR because there is a chance that the 4th most energetic jet in the sparticle system is from radiation and not a top decay. However for this analysis it is more important to accurately gauge the amount of hard ISR of order hundred or more GeV that the ttbar recoils against then amount of softer radiation on the  $t\bar{t}$  side. We found that a looser  $p_T^{\text{jet } 4, S}$  cut of 40 GeV does not cause a difference in the true ISR pt distribution of the

ttbar in the CR and SR.

Distribution of important variables after normalization to  $36.47 \text{ fb}^{-1}$  of data are shown for ttbar CR in figure 10.3. There seem to be no significant slope in signal over background between  $p_T^{\text{jet } 4, S}$  distribution. This allows for the 40 to 50 GeV extrapolation across this variable between CR and SR. There is a noticeable trend in  $p_T^{\text{ISR}}$ . This is not surprising given that a priori we have an 30-35 percent uncertainty in ISR/FSR systematic. The ttbar MC alone is a poor predictor of the amount of ISR which is why we do not extrapolate at all across the  $p_T^{\text{ISR}}$  variable. The disagreement in data and MC in  $p_T^{\text{ISR}}$  further demonstrate the need for a control region that directly measures the amount of ttbar with strong ISR pt directly from data.

The true ISR pt distribution of the events in the CR and SR is shown in figure 10.4. The remarkable similarity between the ttbar true ISR pt distribution in CR and SR show that the CR captures the same ttbar plus strong ISR population that dominates the SR.

We derive the normalization scale factor derived using  $36.47 \text{ fb}^{-1}$  of data for ttbar is 0.73 using the ttbar control region. Therefore the control region tells us that we need to scaled down the amount of ttbar background predicted by the MC in the SR by a factor of 0.73.

This scale factor is quiet different from 1.0 which indicates that the ttbar MC alone does not well model the high ISR pt phase space. This highlights the importance of a control region that captures the same ttbar+strong ISR population that we see in the o lepton SR.

Essentially we place more trust that the MC can predict the relative rates of single lepton and single hadronic tau ttbar then we do in the MC predicting the amount of ISR ttbar produces. This "trust" can be seen in the fact that other systematics such as jet energy scales and lepton ID efficiency

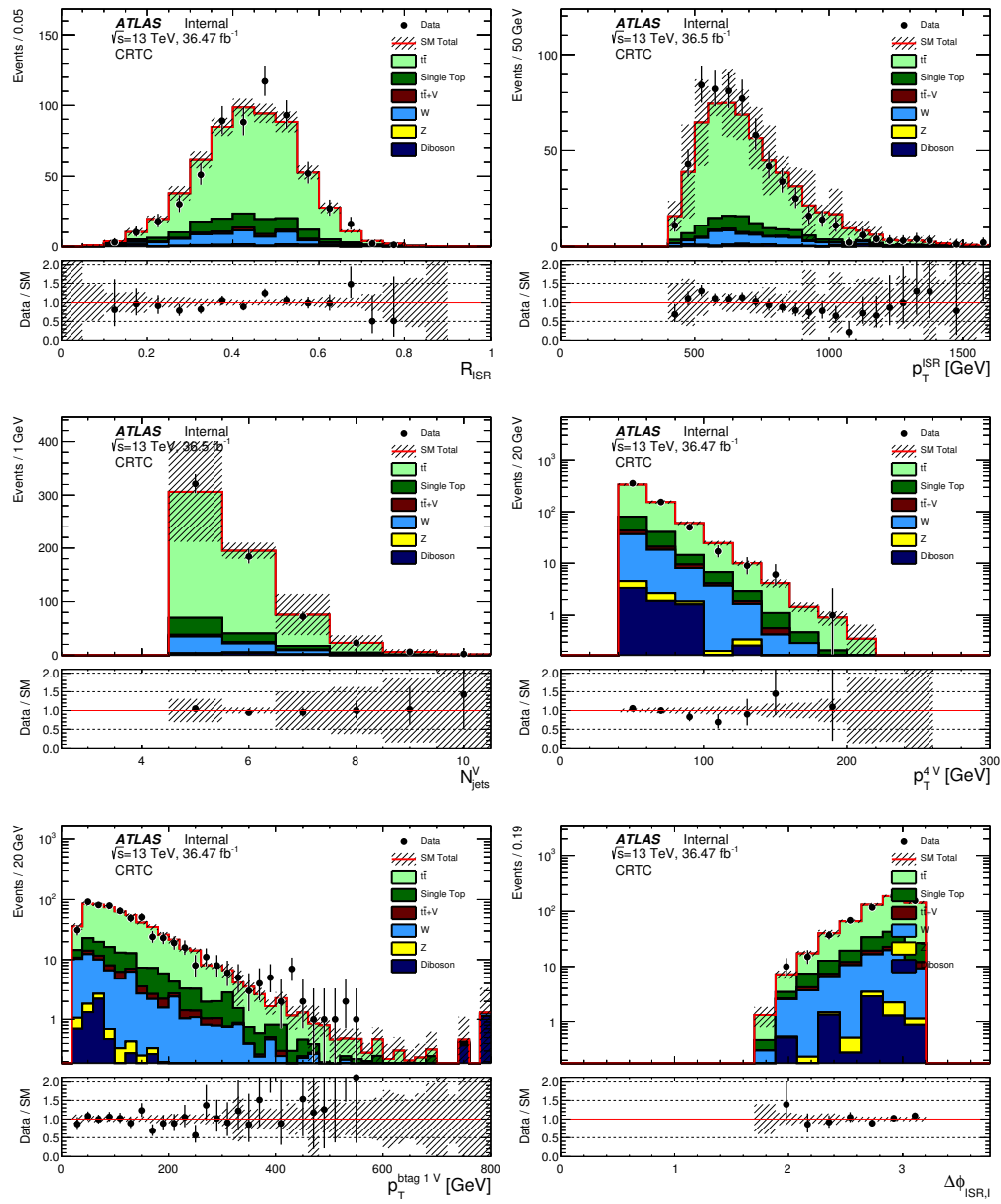


**Figure 10.3:**  $t\bar{t}$  CR postfit distributions for  $36.47 \text{ fb}^{-1}$  of data. The ratio between data and MC is shown in the bottom panel. The hashed area in both the top and lower panel represent the uncertainty due to MC statistics and detector systematic uncertainties.



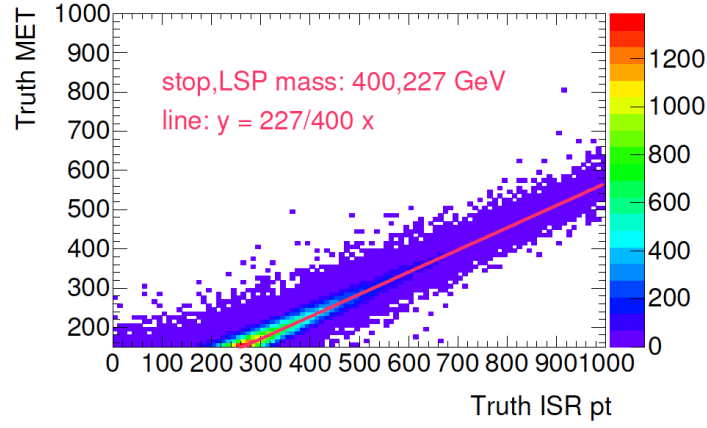


**Figure 10.4:** Distribution of true ISR pt for  $t\bar{t}$  that survive the signal selections and control region selections

are smaller than the ISR/FSR uncertainty. A more detailed discussion of systematics can be found in section ??

#### 10.2.4 VALIDATING $t\bar{t}$ PREDICTIONS IN SIGNAL REGION USING A ZERO LEPTON VALIDATION REGION

We also want a zero lepton region that is orthogonal but close to the signal in order to validate the prediction made by the one lepton  $t\bar{t}$  control region ( $t\bar{t}$  CR). We call this region the zero lepton  $t\bar{t}$  validation region ( $t\bar{t}$  VR). The validation region is designed using the same sensitive variables as the SRC definition to mimic the signal regions as close as possible while maintaining a high purity of the dominant background semi-leptonic  $t\bar{t}$ .

The requirement on  $M_T^S$  is reduced to 100 GeV (vs. 300 GeV in the SR) and an  $N_{\text{jet}}^S \geq 4$  selection is applied (vs.  $N_{\text{jet}}^S \geq 5$  in the SR) to enhance the yields of semi-leptonic  $t\bar{t}$  events. A requirement of  $M_T^{S,Vis}/M_T^S < 0.6$  is added to both to reduce signal contamination and protect

**Table 10.2:** Zero-lepton  $t\bar{t}$ +ISR validation region definitions, in addition to the SRC requirements listed in Table ??.

Variable	
$N_{\text{jet}}^S$	$\geq 4$
$N_{\text{btag}}^S$	$\geq 1$
$p_T^{\text{btag } 1, S}$	$\geq 40$
$p_T^{\text{ISR}}$	$\geq 400$
$M_T^S$	$> 100 \text{ GeV}$
$M_T^{S, Vis} / M_T^S$	$< 0.6$
$\Delta\phi_{\text{ISR}, I}$	$< 3.00$

against any remaining QCD multi-jet contribution. Again  $p_T^{\text{jet } 4, S} > 50 \text{ GeV}$  cuts are relaxed to  $p_T^{\text{jet } 4, S} > 40 \text{ GeV}$  to increase VR statistics.

Finally the  $\Delta\phi_{\text{ISR}, I}$  cut is inverted to  $\Delta\phi_{\text{ISR}, I} < 3.0$  to cut out signal and maintain orthogonality to the signal region. We expect  $t\bar{t}$  events to have neutrinos that don't go directly opposite the

The distributions of the SRC sensitive variables in the  $t\bar{t}$ +jets zero-lepton validation regions are shown in Fig. 10.5, with normalizations and systematic uncertainties corresponding to those predicted by the iL  $t\bar{t}$ +ISR CR fitted to  $36.47 \text{ fb}^{-1}$  defined in Table 10.2.

The agreement between data and MC prediction in the VR after applying the CR scale factor is better than 1 sigma. The  $R_{\text{ISR}}$  shape seems to be well modeled as we see no distinct trends in the data vs MC ratio in  $R_{\text{ISR}}$ .

This agreement both in magnitude and shape demonstrates two things. One, the  $t\bar{t}$  control

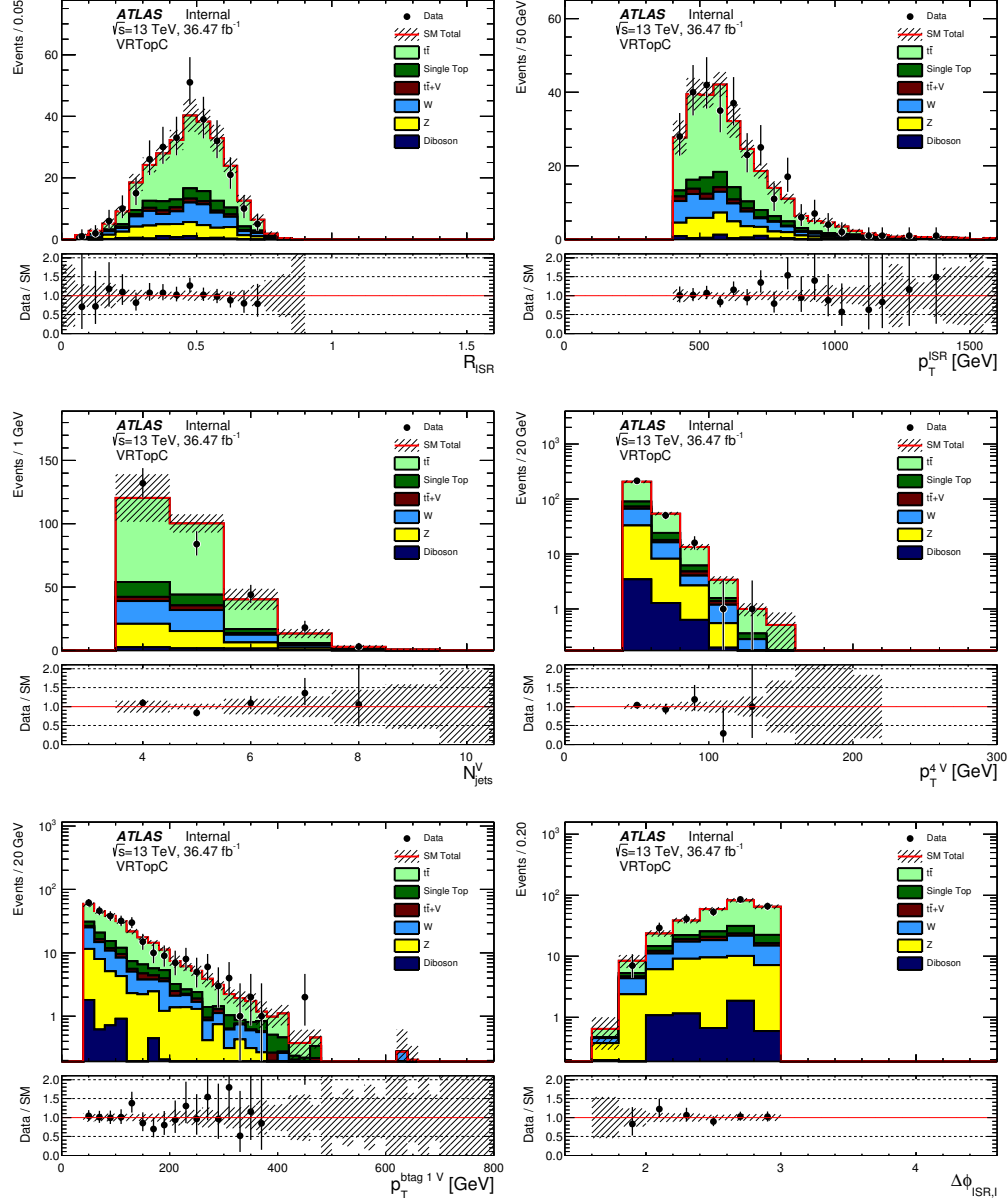


Figure 10.5: Distribution of ISR signal region sensitive variables selections in the zero-lepton  $t\bar{t}$  validation region.

region indeed does correctly measure the amount of  $t\bar{t}$  plus strong ISR that exists in both signal and validation region. Two, the sub-dominant background predictions also cannot be wrong by more than around 100 percent. For example we clearly would see disagreement in between data vs MC in this VR if the MC underestimated  $W$ +jets or  $Z$ +jets background by 100 percent. Both of these facts gives us confidence that the predictions for the amount of background in the signal region is correct.

### 10.3 SUBDOMINANT BACKGROUNDS

#### 10.3.1 STANDARD MODEL $W$ +JETS

$W$  boson produced in conjunction with QCD jets ( $W$ +jets) consists our largest sub-dominate background.  $W$ +jets consists of 5 percent of the total background in the SR. However the distribution of  $W$ +jets is not uniform across  $R_{\text{ISR}}$ .  $W$ +jets can reach around 15 percent of all background in the SR bins with the largest  $R_{\text{ISR}}$ . This means the  $W$ +jets contribution mostly affects the signal with high stop masses because those signal samples peak at high  $R_{\text{ISR}}$ .

We estimate  $W$ +Jets using a 1 lepton control region defined in section 10.3.1. The 1 lepton  $W$ +jet CR is orthogonal to the 1 lepton  $t\bar{t}$  CR and 1 lepton single top CR defined in table 10.1 and ?? .

The  $W$ +jets prediction is checked in a  $W$ +jets validation region defined in section ??

**Table 10.3:** Summary of the selection for the 1-lepton,  $W$ +jets control regions. The signal lepton is treated as a jet for the jet counting and  $p_T$  ordering as well as for the top reco.

	CRW
Number of leptons	1
Number of jets (incl. lepton)	$\geq 4$
$p_T$ of jets (incl. lepton)	(80,80,40,40) GeV
$\min  \Delta\phi(\text{jet}^{o-1}, E_T^{\text{miss}}) $	$> 0.4$
$E_T^{\text{miss}}$	$> 250$ GeV
$m_T(\ell, E_T^{\text{miss}})$	( $> 30, < 100$ GeV)
Number of $b$ -jets	= 1
$m_{\text{jet},R=1.2}^o$	$< 60$ GeV
$\Delta R(b_{o,1}, \ell)_{\min}$	$> 2.0$

### $W$ + jets CONTROL REGION

$m_{\text{jet},R=1.2}^o < 60$  GeV ensures that no boosted tops are reconstructed. The number of  $b$ -tagged jets ensures orthogonality with the single top CR. The selection on  $\Delta R(b_{o,1}, \ell)_{\min}$ , defined as the minimum  $\Delta R$  between the two jets with the highest  $b$ -tag weight and the selected lepton, ensures the orthogonality of  $t\bar{t}$ bar CR and  $W$ +jet CR.

Data/MC comparisons in the  $W$  + jets control region are shown in Fig. 10.6, 10.7, 10.8 and the yields in in Table 10.4. The MC is normalised to  $36.47 \text{ fb}^{-1}$ , and no normalisation factors are applied to any of the SM components. Only variables for which there is an extrapolation from CRW to the various SRs are shown. For SRA the extrapolation is in  $E_T^{\text{miss}}$ ,  $\Delta R(b, b)$ ,  $m_{\text{jet},R=1.2}^o$ ,  $m_{\text{jet},R=1.2}^I$ , and  $m_{\text{jet},R=0.8}^o$  while for SRB the extrapolation is in  $m_T^{b,\min}$ ,  $m_T^{b,\max}$ , and  $\Delta R(b, b)$ . The leading jet  $p_T$ s and the leading  $b$ -tagged jet  $p_T$  are shown because for these variables there is an extrapolation

from CRW to SRD while the  $E_T^{\text{miss}}$ ,  $m_T^{b,\text{min}}$ ,  $H_T$ ,  $E_T^{\text{miss}}/\sqrt{H_T}$ ,  $m_{\text{jet},R=0.8}^o$ , and  $m_{\text{jet},R=0.8}^t$  are shown due to the extrapolation to SRE. The signal contamination is less than 10% for all signal points with the largest contamination coming from the pure bChino decay of stops with mass 500 GeV and LSP mass of 50 GeV where the chargino mass is assumed to be 100 GeV. No particular trends are observed in the data-MC ratios in any of the distribution. Within statistical uncertainty the data are compatible with the MC SM expectation.

CRW (60% purity)	
Z	$1.99 \pm 0.45$
dibosons	$9.85 \pm 1.76$
ttbar	$128.42 \pm 3.82$
singleTop	$51.14 \pm 3.37$
ttV	$1.07 \pm 0.16$
W	$288.12 \pm 8.86$
Total MC	$480.58 \pm 10.38$
Data	$531.00 \pm 23.04$
SF	$1.17 \pm 0.10$

**Table 10.4:** Yields in the CRW in  $36.47 \text{ fb}^{-1}$  of data.

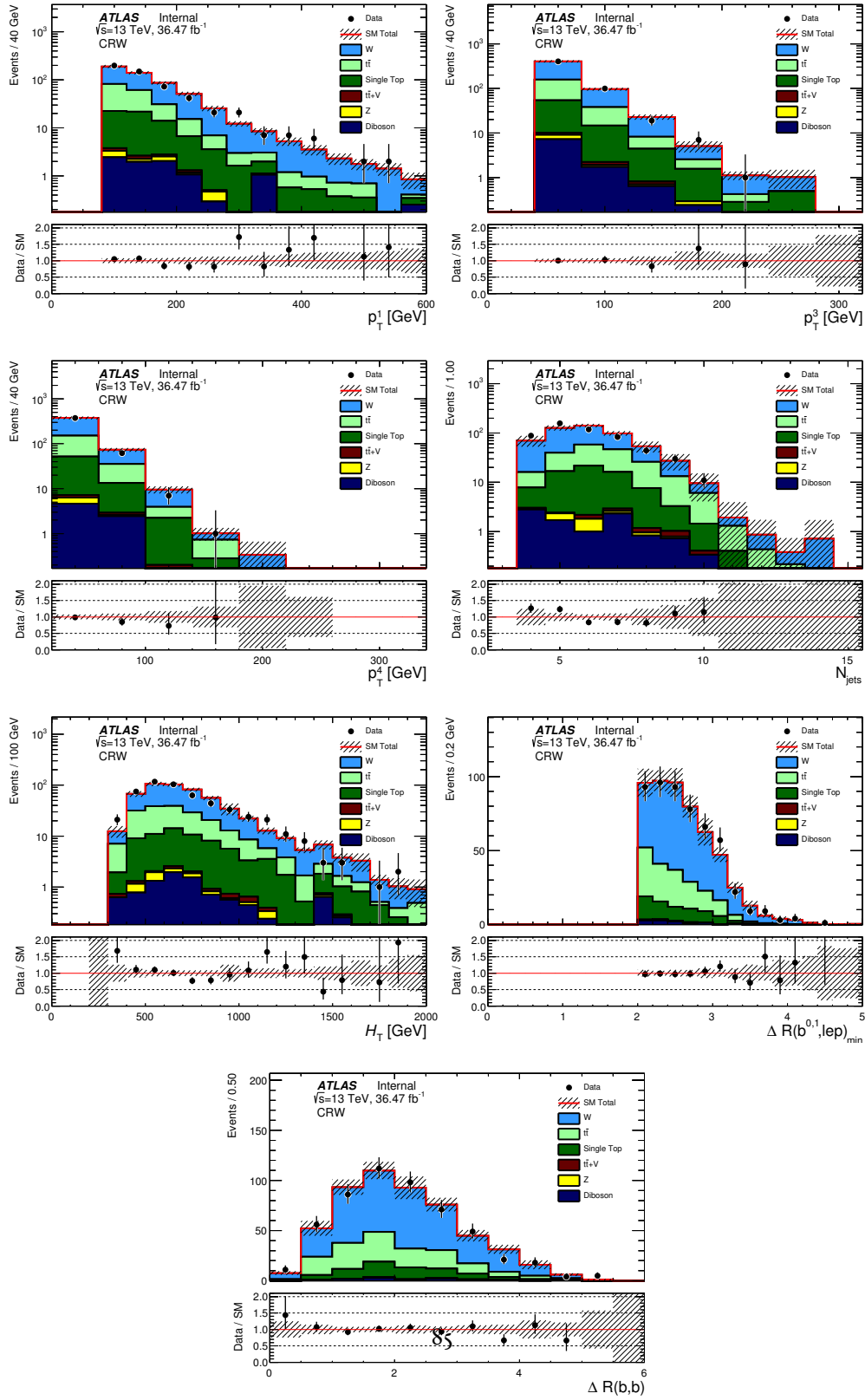


**Figure 10.6:** Postfit data/MC comparisons in the CRW. From left to right and top to bottom, the variables shown are the leading four jet  $p_T$ , the leading  $b$ -tagged jet  $p_T$ ,  $H_T$ ,  $E_T^{\text{miss}}/\sqrt{H_T}$ ,  $\Delta R(b_{0,1}, \ell)_{\text{min}}$ , and  $\Delta R(b, b)$ . The background contributions from MC are normalised to  $36.47 \text{ fb}^{-1}$ , and summed together, the data points are shown in black. The hatched band in the ratio shows the MC statistical and detector uncertainties.

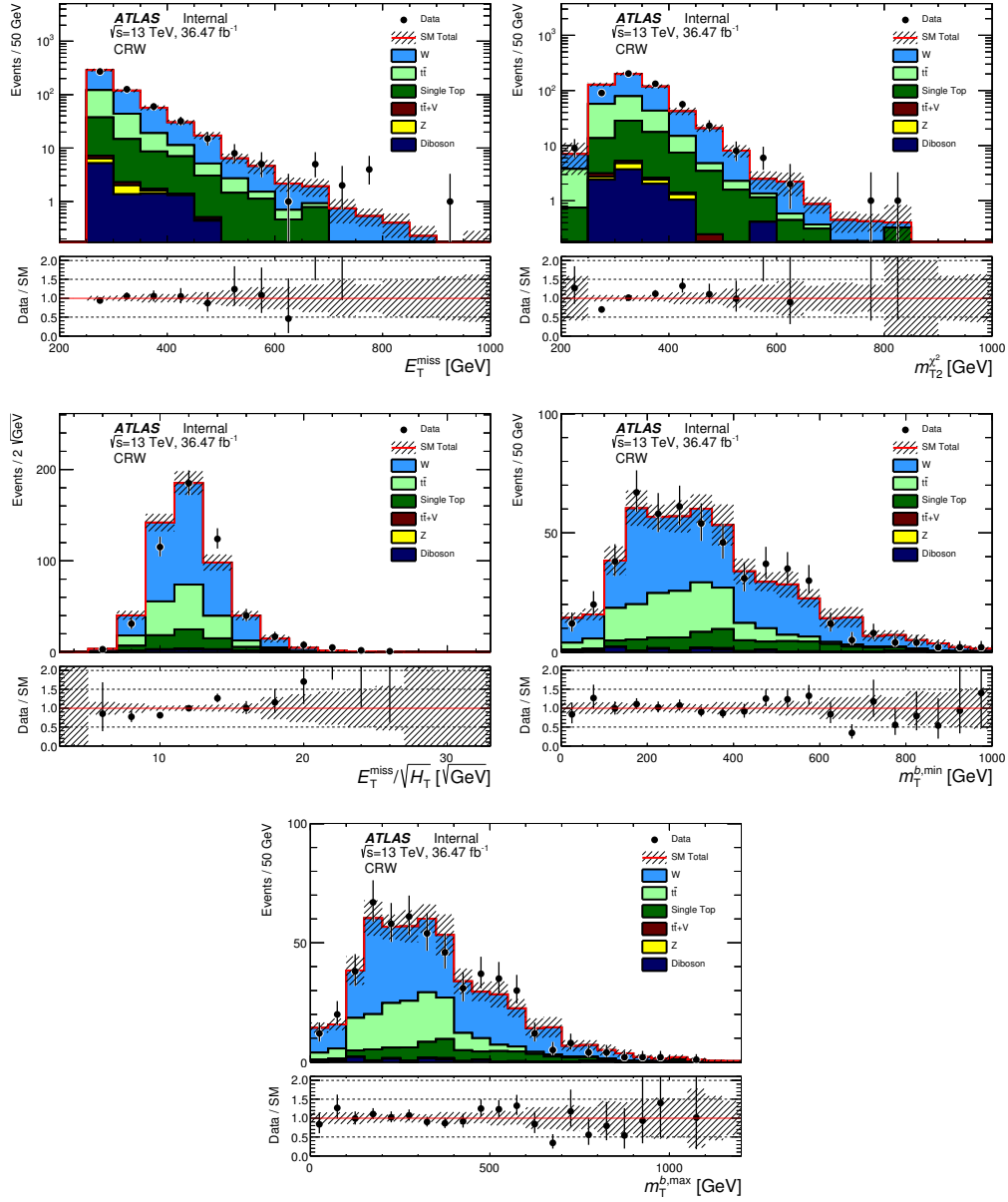


**Figure 10.7:** Postfit data/MC comparisons in the CRW. From left to right and top to bottom, the variables shown are  $E_T^{\text{miss}}$ ,  $m_{T1}^{b, \text{min}}$ ,  $m_{T1}^{b, \text{max}}$ ,  $m_{\text{jet}, R=1,2}^{\text{b}}$ ,  $m_{\text{jet}, R=1,2}^{\text{t}}$ , and  $m_{\text{jet}, R=0,8}^{\text{b}}$ . The background contributions from MC are normalised to  $36.47 \text{ fb}^{-1}$ , and summed together, the data points are shown in black. The hatched band in the ratio shows the MC statistical and detector uncertainties.



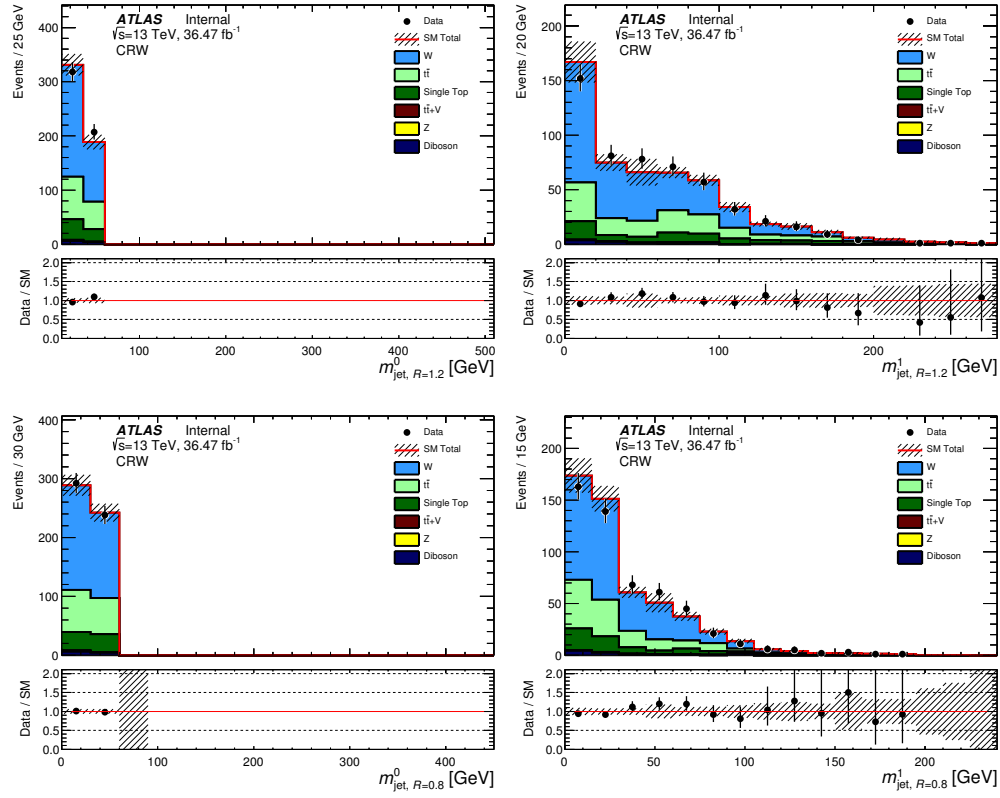


**Figure 10.8:** Postfit data/MC comparisons in the CRW. From left to right and top to bottom, the variables shown are  $E_{\text{T}}^{\text{miss}}$ ,  $m_{\text{T}}^{b, \text{min}}$ ,  $m_{\text{T}}^{b, \text{max}}$ ,  $m_{\text{jet}, R=1.2}^0$ ,  $m_{\text{jet}, R=1.2}^1$ , and  $m_{\text{jet}, R=0.8}^0$ . The background contributions from MC are normalised to  $36.47 \text{ fb}^{-1}$ , and summed together, the data points are shown in black. The hatched band in the ratio shows the MC statistical and detector uncertainties.

## $W + \text{jets}$ VALIDATION REGION

The selections for a possible  $W + \text{jets}$  validation region in the 1-lepton, two b-jets channel (VRW) are summarised in Tab. 10.5.

**Table 10.5:** Summary of the selection for the 1-lepton  $W$ +jets validation region. The signal lepton is treated as a jet. The same  $E_T^{\text{miss}}$  triggers as mentioned in Table ?? are used.

	VRW
Number of leptons	1
Number of jets (incl. lepton)	$\geq 4$
$p_T$ of jets (incl. lepton) in GeV	(80,80,40,40)
Number of $b$ -jets	$\geq 2$
$\min  \Delta\phi(\text{jet}^{0-1}, E_T^{\text{miss}}) $	$> 0.4$
$E_T^{\text{miss}}$	$> 250 \text{ GeV}$
$m_T(\ell, E_T^{\text{miss}})$	$> 30, < 100 \text{ GeV}$
$m_{\text{jet},R=1,2}^0$	$< 70 \text{ GeV}$
$m_T^{b,\min}$	$150 \text{ GeV}$
$\Delta R(b_{0,1}, \ell)_{\min}$	$> 1.8$

The yields in the VRW region are summarised in Tab. 10.6. The  $W + \text{jets}$  purity in this region is 30% while the signal contamination is less than 15% for all signal benchmark points except for  $(m_{\tilde{t}}, m_{\tilde{\tau}^\pm}, m_{\tilde{\nu}^0}) = (550, 100, 50) \text{ GeV}$  which has been excluded in previous searches.

A selection of distributions where data is compared to MC (no normalisation factors applied) is shown in Fig. 10.10.

The relative  $W + \text{jets}$  composition split in contributions from the CVetoBVeto, CFilterBVeto and BFilter samples in the  $W + \text{jets}$  control region is 19.6%, 36.6%, and 43.7% respectively. The same fractions in the WVR are 2.1%, 7.7%, and 90.2%. As an example in SRB-To the  $W + \text{jets}$  relative

VRW (38% purity)	
Z	$0.21 \pm 0.07$
dibosons	$3.05 \pm 0.89$
ttbar	$35.72 \pm 2.02$
singleTop	$42.62 \pm 1.47$
ttV	$0.57 \pm 0.13$
W	$50.45 \pm 3.50$
Total MC	$132.63 \pm 4.40$
Data	$140.00 \pm 11.83$
SF	$1.15 \pm 0.31$

**Table 10.6:** Yields in the VRW in  $36.47 \text{ fb}^{-1}$  of data. The uncertainty on the SF, which is compatible within statistical uncertainties with the SF from the CR, should come down significantly.

composition is 0.1% CVetoBVeto, 11.8% CFilterBVeto, 88.1% BFilter - the numbers of CVetoBVeto and CFilterBVeto events in the SR are affected by very large uncertainty due to MC statistics. This shows that even though the composition in the CR does not reflect completely the SR composition, the VR is designed to have very similar type of events as the SR and being hence a very good test of the goodness of the Fit in the CR.

The  $W + c$  contribution in the CR amounts to 9.73%, in the VR to 5.15%, and in SRC-high to 1.86% (number based on 20.1, Sherpa 2.1 samples).

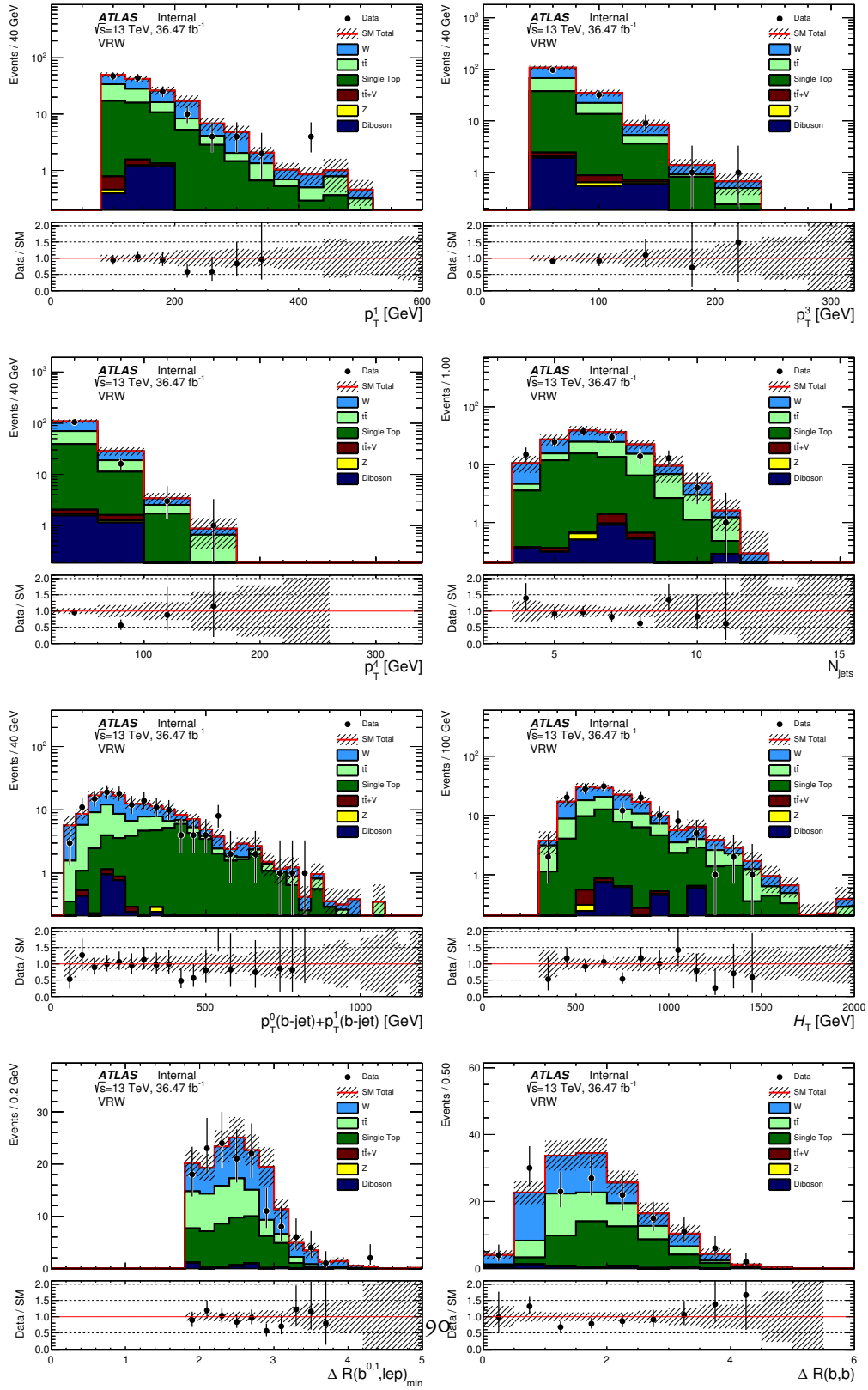


**Figure 10.9:** Postfit data/MC comparisons in the VRW. From left to right and top to bottom, the variables shown are the leading four jet  $p_T$ , the leading b-tagged jet  $p_T$ ,  $H_T$ ,  $E_T^{\text{miss}}/\sqrt{H_T}$ ,  $\Delta R(b_{0,1}, \ell)_{\min}$ , and  $\Delta R(b, b)$ . The background contributions from MC are normalised to 36.47 fb<sup>-1</sup>, and summed together, the data points are shown in black. The hatched band in the ratio shows the MC statistical and detector uncertainties.

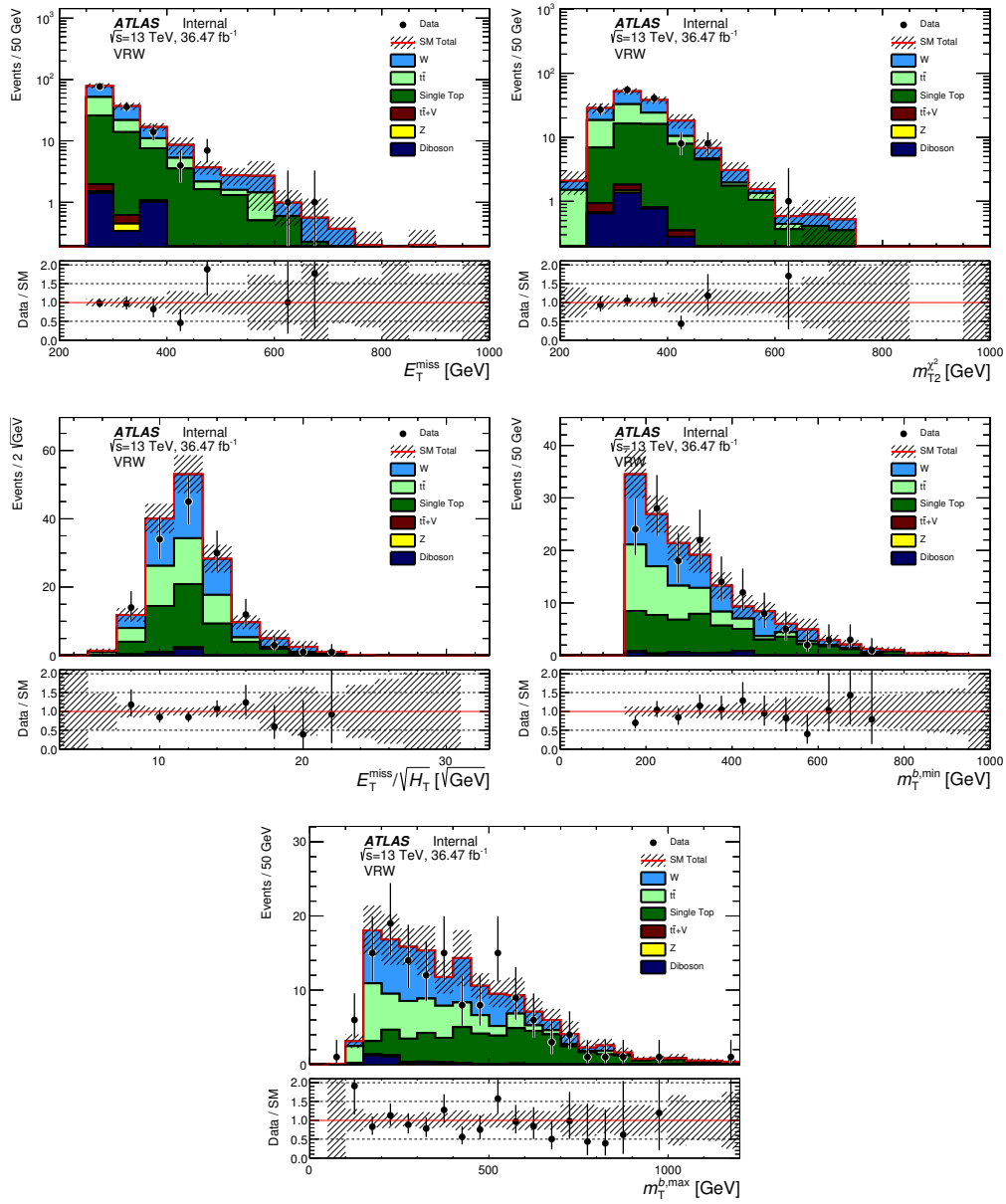


**Figure 10.10:** Postfit data/MC comparisons in the VRW. From left to right and top to bottom, the variables shown are  $E_T^{\text{miss}}$ ,  $m_{T1}^{b,\text{min}}$ ,  $m_{T1}^{b,\text{max}}$ ,  $m_{\text{jet},R=1,2}^o$ ,  $m_{\text{jet},R=1,2}^i$ , and  $m_{\text{jet},R=0,8}^o$ . The background contributions from MC are normalised to  $36.47 \text{ fb}^{-1}$ , and summed together, the data points are shown in black. The hatched band in the ratio shows the MC statistical and detector uncertainties.

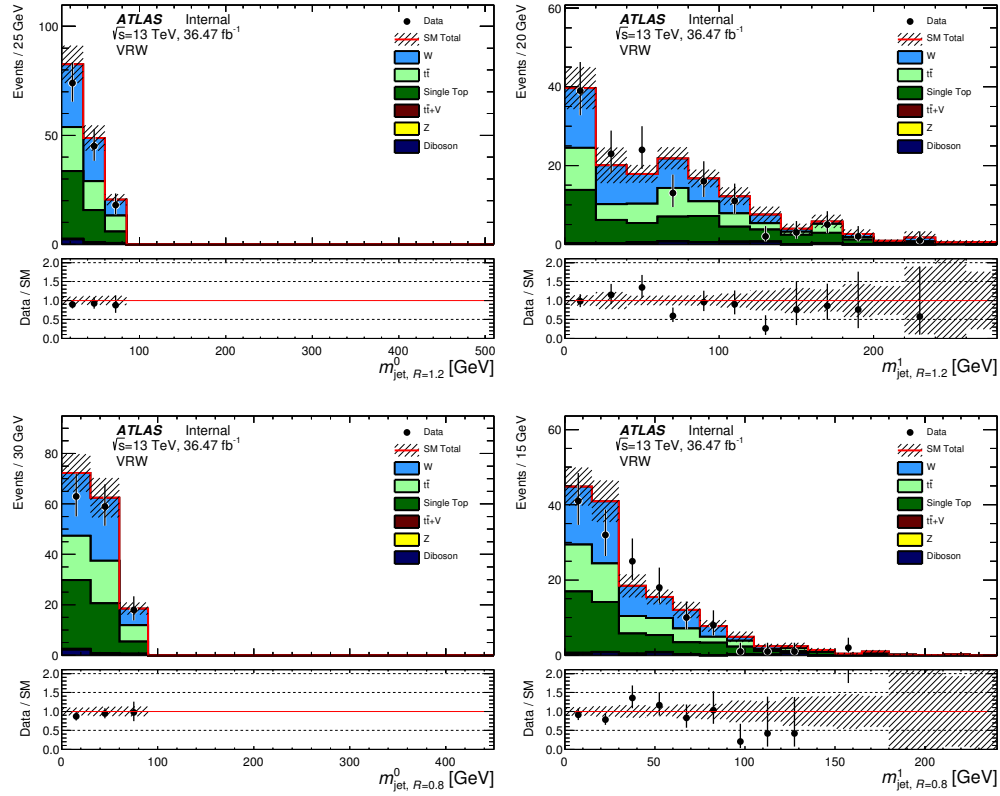


**Figure 10.11:** Postfit data/MC comparisons in the VRW. From left to right and top to bottom, the variables shown are  $E_T^{\text{miss}}$ ,  $m_T^{b,\text{min}}$ ,  $m_T^{b,\text{max}}$ ,  $m_{\text{jet}, R=1.2}^0$ ,  $m_{\text{jet}, R=1.2}^1$ , and  $m_{\text{jet}, R=0.8}^0$ . The background contributions from MC are normalised to  $36.47 \text{ fb}^{-1}$ , and summed together, the data points are shown in black. The hatched band in the ratio shows the MC statistical and detector uncertainties.

### 10.3.2 STANDARD MODEL SINGLE TOP

Standard Model single top consists of 3 to 7 percent of the background in any one  $R_{\text{ISR}}$  bin. In total, single top consist of 4 percent of the total background in SRC. A 1 lepton single top control region is defined in section 10.3.2. The single top CR is orthogonal to both the  $W$ +jets control region and ttbar control region.

### SINGLE TOP CONTROL REGION

**Table 10.7:** Selection for the 1-lepton, single top control region. The signal lepton is treated as a jet for the jet counting and  $p_T$  ordering as well as for the top reco.

	CRST
Number of leptons	1
Number of jets (incl. lepton)	$\geq 4$
$p_T$ of jets (incl. lepton)	(80,80,40,40) GeV
$\min  \Delta\phi(\text{jet}^{0-1}, E_T^{\text{miss}}) $	$> 0.4$
$E_T^{\text{miss}}$	$> 250$ GeV
$m_T(\ell, E_T^{\text{miss}})$	$> 30, < 100$ GeV
Number of $b$ -jets	$\geq 2$
$m_{\text{jet}, R=1,2}^o$	$> 120$ GeV
$m_T^{b, \text{min}}$	$> 200$ GeV
$\Delta R(b_{o,1}, \ell)_{\text{min}}$	$> 2.0$
$\Delta R(b, b)$	$> 1.5$

The selection on  $\Delta R(b_{o,1}, \ell)_{\text{min}}$ , defined as the minimum  $\Delta R$  between the two jets with the highest  $b$ -tag weight and the selected lepton, ensures the orthogonality of CRTop and CRST. In CRST the requirement on the  $\Delta R$  of the two leading-weight  $b$ -jets is necessary to reject a large part of the

remaining  $t\bar{t}$  background and reach a single top purity of  $\sim 50\%$ .

Data-MC comparisons in the single top control region are shown in Table 10.8 and for a selection of variables are shown in Fig. 10.12, 10.13, and 10.14.

CRST (44% purity)	
Z	$0.11 \pm 0.05$
dibosons	$1.52 \pm 0.54$
$t\bar{t}$ bar	$34.17 \pm 2.10$
singleTop	$45.62 \pm 1.41$
$t\bar{t}V$	$2.42 \pm 0.19$
W	$19.72 \pm 1.69$
Total MC	$103.57 \pm 3.10$
Data	$113.00 \pm 10.63$
SF	$1.21 \pm 0.29$

**Table 10.8:** Yields in the CRST in  $36.47 \text{ fb}^{-1}$  of data.



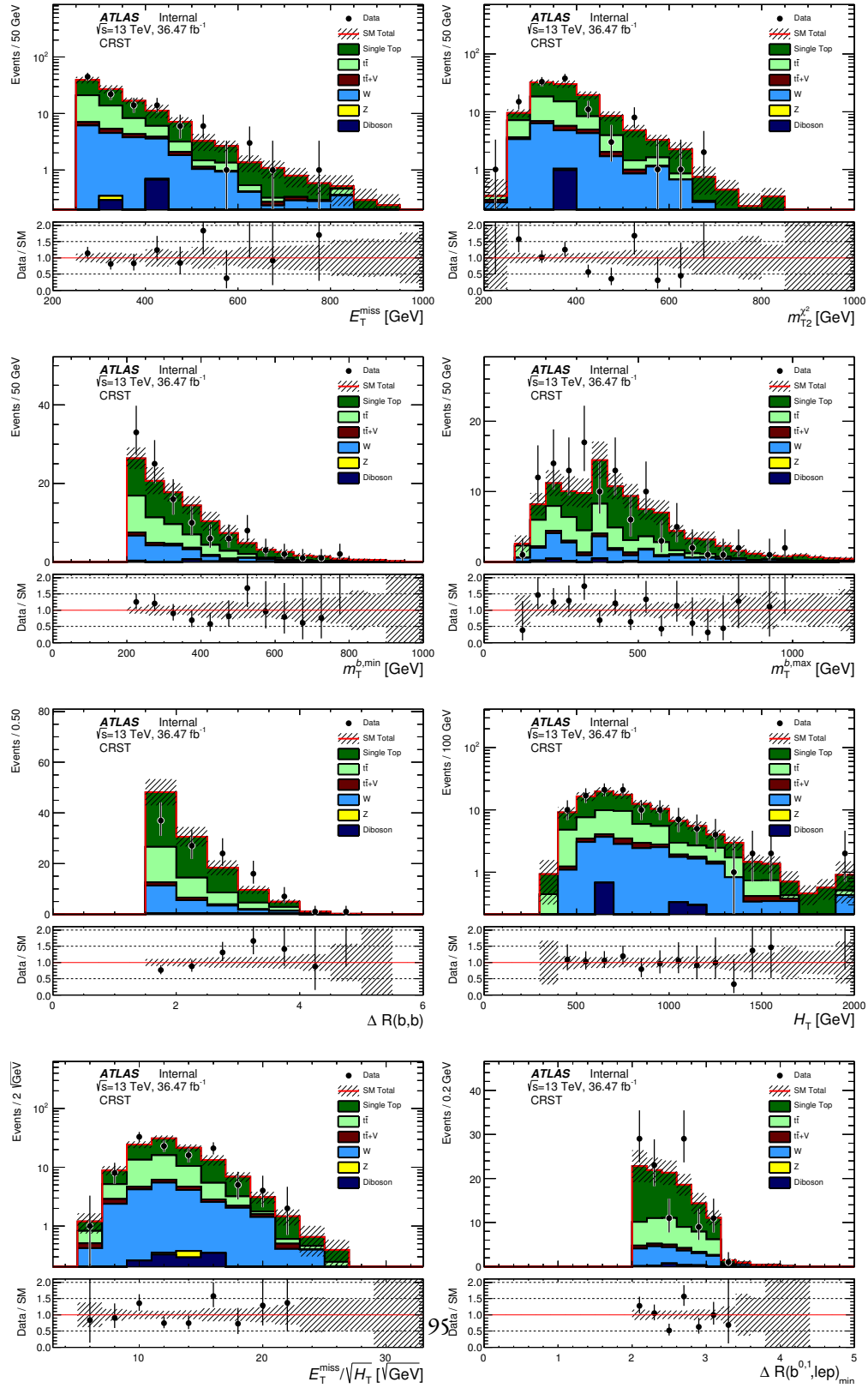


**Figure 10.12:** Single top postfit control region distributions for 36.47 fb<sup>-1</sup> of data. The ratio between data and MC is shown in the bottom panel. The hashed area in both the top and lower panel represent the uncertainty due to MC statistics.

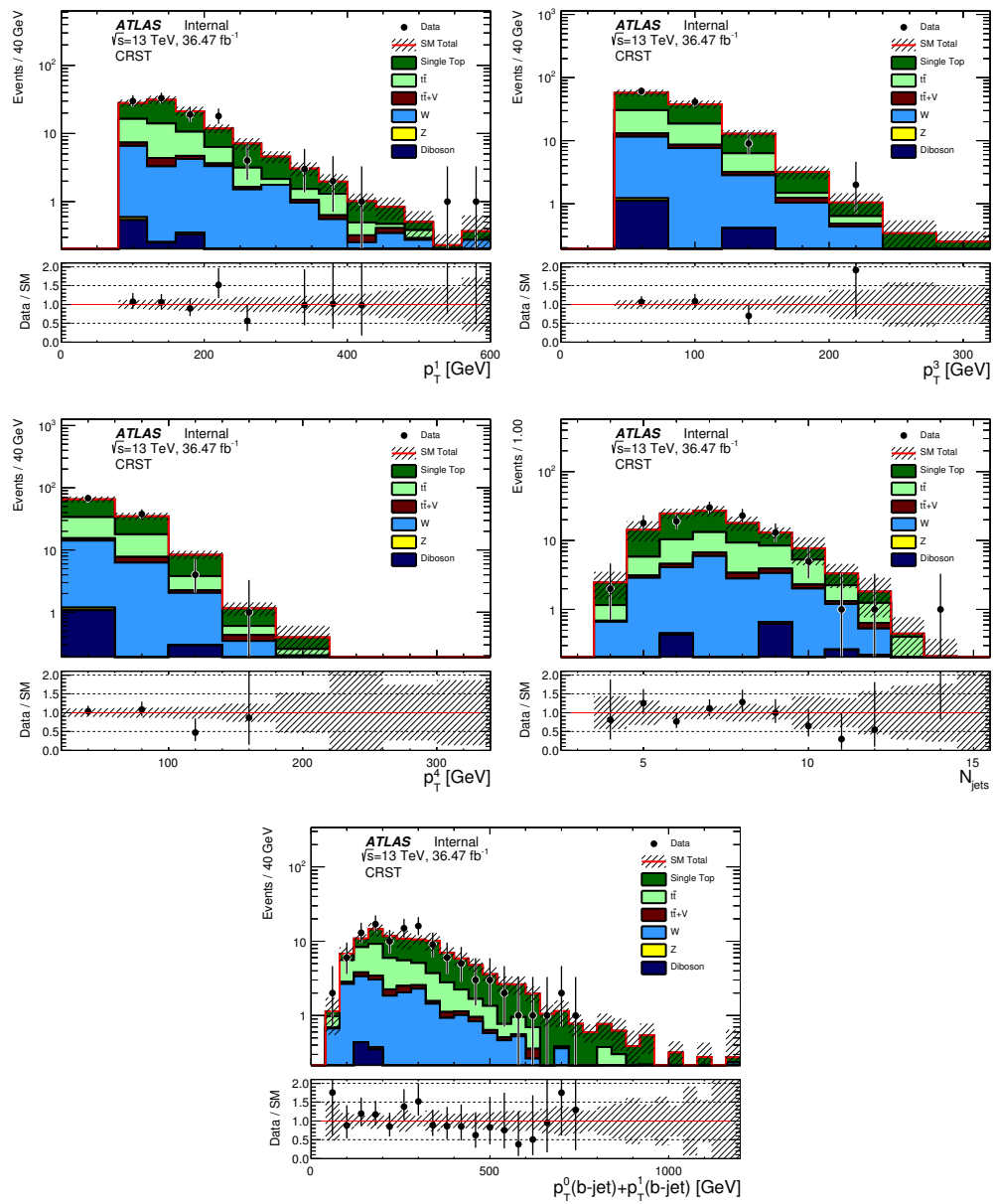


**Figure 10.13:** Single top postfit control region distributions for 36.47 fb<sup>-1</sup> of data. The ratio between data and MC is shown in the bottom panel. The hashed area in both the top and lower panel represent the uncertainty due to MC statistics.

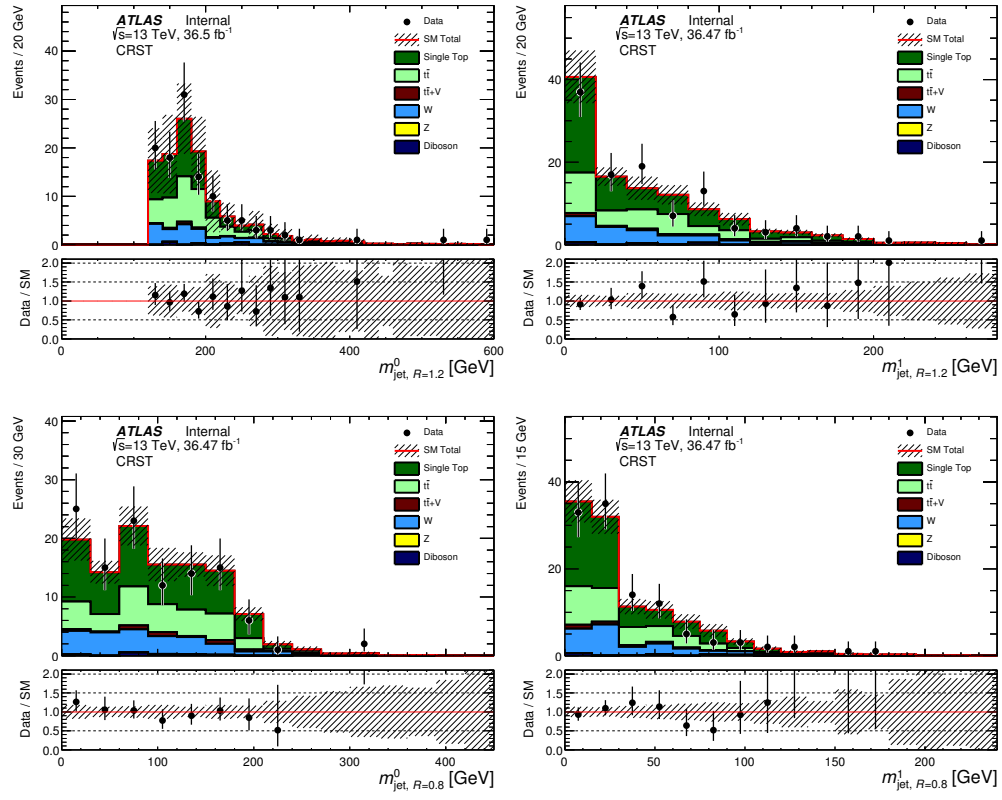


**Figure 10.14:** Single top postfit control region distributions for 36.47 fb<sup>-1</sup> of data. The ratio between data and MC is shown in the bottom panel. The hashed area in both the top and lower panel represent the uncertainty due to MC statistics.

### 10.3.3 STANDARD MODEL $t\bar{t}+Z$

$t\bar{t}$  produced in conjunction with a  $Z$  boson consist of about 1 percent of the background in the SR.

Although the background is essentially negligible we do estimate the amount of  $t\bar{t} + Z$  using a  $t\bar{t} + \gamma$  CR. Designing a CR to estimate the  $t\bar{t} + Z$  background by using the charged leptonic  $Z$  boson decays would be favorable. However, such CR is difficult to design due to low statistics and the small branching fraction to leptons. In particular a 2-lepton CR suffers from a large contamination of  $t\bar{t}$  and  $Z + \text{jets}$  processes. For this reason, another data driven approach is followed by building a one-lepton CR for  $t\bar{t}\gamma$  which is a similar process. A zero-lepton region was considered as a validation region but it was found to have a too low  $t\bar{t}\gamma$  contribution, with  $\gamma + \text{jets}$  being the main contaminant.

The CR is designed to minimize the differences between the two processes and keep the theoretical uncertainties from the extrapolation of the  $\gamma$  to the  $Z$  low.

The  $t\bar{t} + \gamma$  CR requires exactly one photon with a FixedCutTight isolation WP, exactly one signal lepton (electron or muon as defined in Section ??) and at least four jets of which at least two are required to be b-tagged. To collect these events the lepton triggers described in Table ?? are used.

Moreover, due to the difference in mass between the  $Z$  and the  $\gamma$ , to mimic the  $Z \rightarrow \nu\bar{\nu}$  decay, the highest  $p_T$  photon is required to have  $p_T > 150$  GeV.

Unlike the CRTops, CRW, and CRST one-lepton control regions the lepton is not treated as a jet. Instead, the photon is used to model the  $E_T^{\text{miss}}$  since the  $E_T^{\text{miss}}$  from  $t\bar{t} + Z$  in the SR originates mostly from the neutrino decay of the  $Z$ .

The details of the selection for the one-lepton CR are summarized in Table 10.9.

**Table 10.9:** Selection for the  $t\bar{t} + \gamma$  1 lepton CR. The same triggers as described in Table ?? are used and the same signal lepton requirements are made as in Tables ?? and ??

Selection	Requirement
Event selection	Event cleaning
Leptons	exactly 1
Lepton $p_T$	$\geq 28$ GeV
Photons	exactly 1
jet multiplicity	$\geq 4$
Jet $p_T$	$(80, 80, 40, 40)$ GeV
b-jet multiplicity	$\geq 2$
$\gamma p_T$	$> 150$ GeV

Table 10.10 shows the background composition for the  $t\bar{t}\gamma$  CR. A normalisation factor is derived as the ratio between data and MC correcting for the contamination for non- $t\bar{t}\gamma$  backgrounds.

Data/MC comparisons of several distributions are shown in the following figures after applying the full selection in Table 10.9.

Truth studies are performed in order to check the differences in kinematic distributions. The truth  $p_T$  ratio for a 2-bjet selection are shown in Fig. 10.19.

**Table 10.10:** Background composition of  $t\bar{t}\gamma$  CR.

CRTTGamma (87% purity)	
ttGamma	$112.20 \pm 1.49$
VGamma	$6.41 \pm 0.70$
Z	$0.73 \pm 0.21$
dibosons	$0.00 \pm 0.00$
ttbar	$4.57 \pm 1.23$
singleTop	$2.01 \pm 0.81$
ttV	$2.42 \pm 0.28$
W	$0.04 \pm 0.02$
Total MC	$128.38 \pm 2.23$
Data	$160.00 \pm 12.65$
SF	$1.28 \pm 0.12$

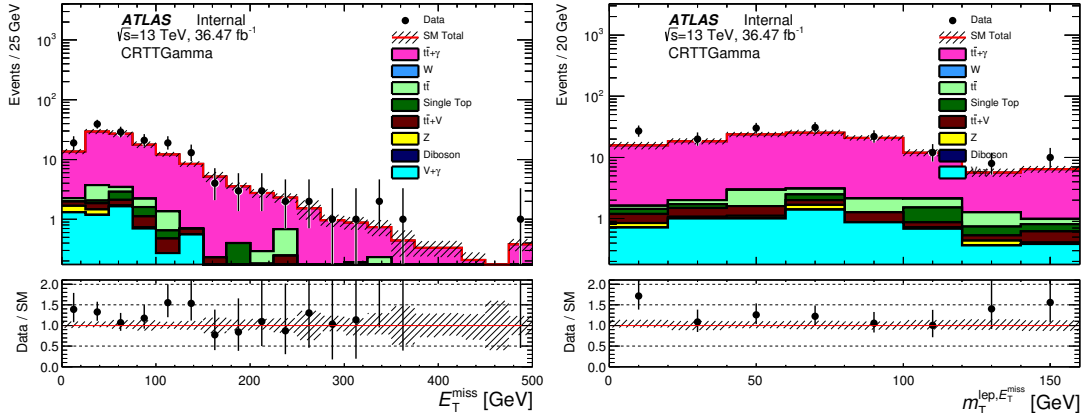


**Figure 10.15:** Prefit distributions of the  $E_T^{\text{miss}}$  and  $m_T(\ell, E_T^{\text{miss}})$  for fake lepton checks. Agreement at low  $m_T(\ell, E_T^{\text{miss}})$  is reasonable indicating no significant contributions from fake leptons. The ratio between data and MC is given in the bottom panel. The hashed area in both the top and lower panel represents the uncertainty due to MC statistics.

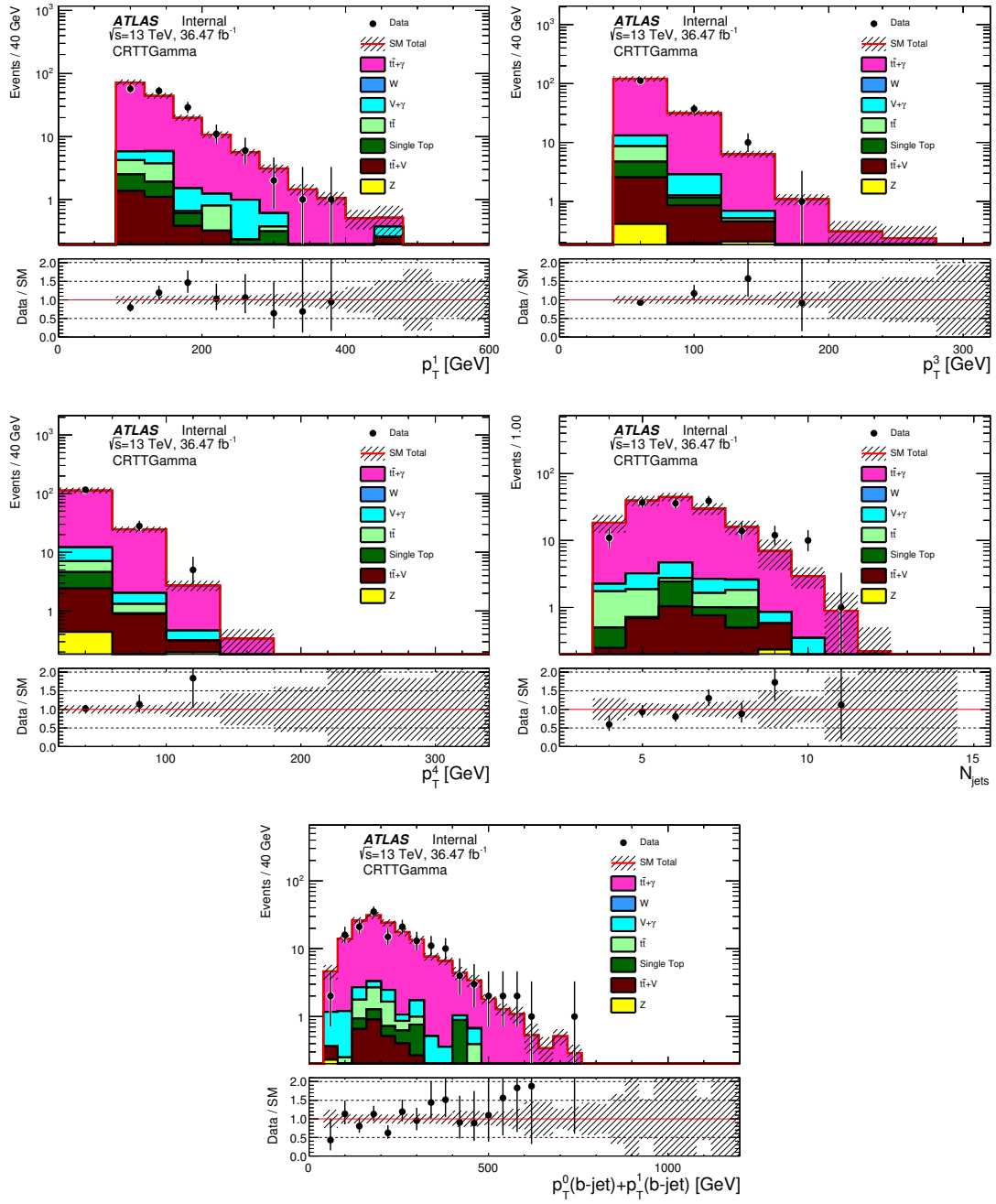


**Figure 10.16:** Postfit distributions of the  $p_T$  of the leading and subleading jets for the 2 b-jets selection. The ratio between data and MC is given in the bottom panel. The hashed area in both the top and lower panel represents the uncertainty due to MC statistics.

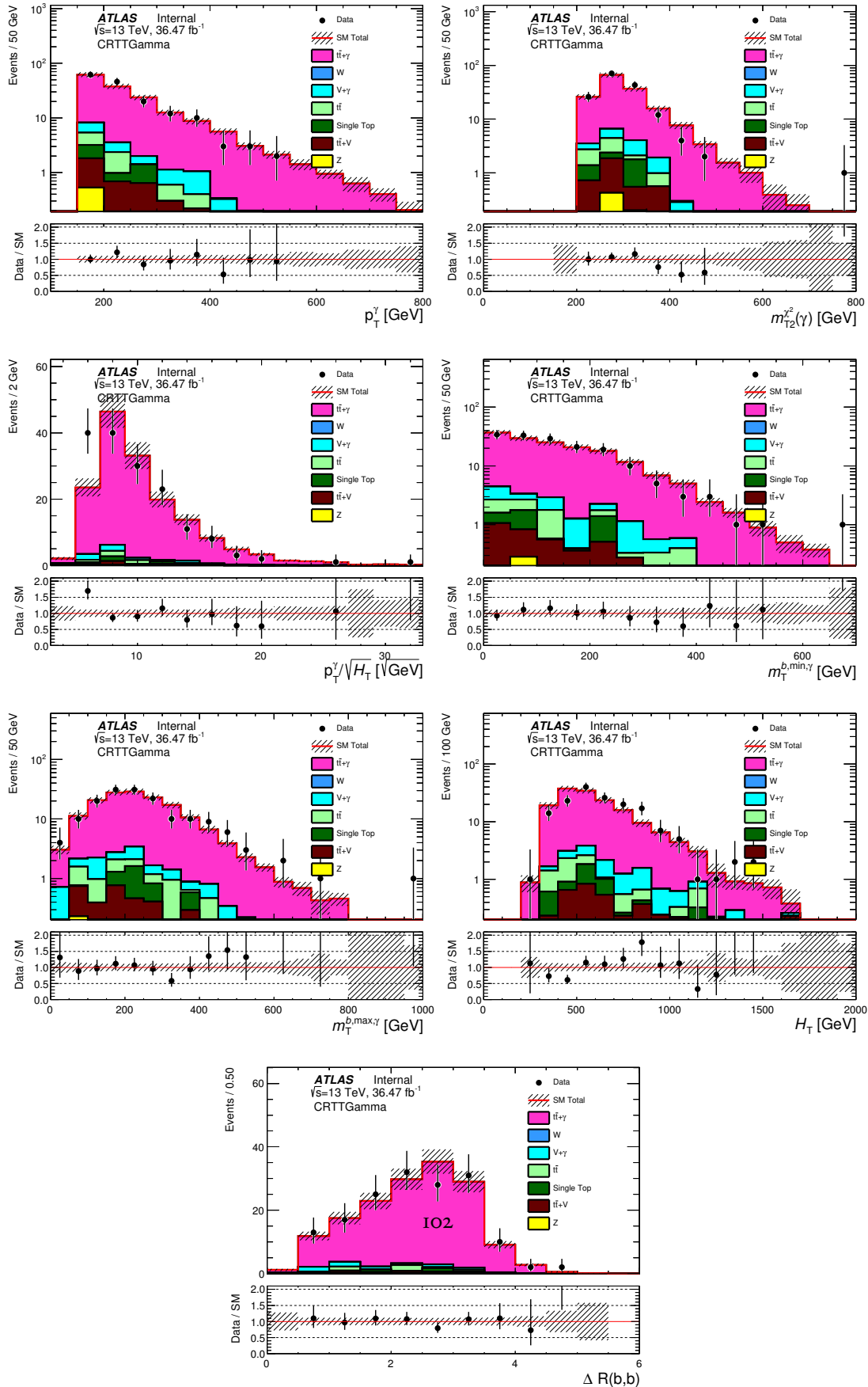
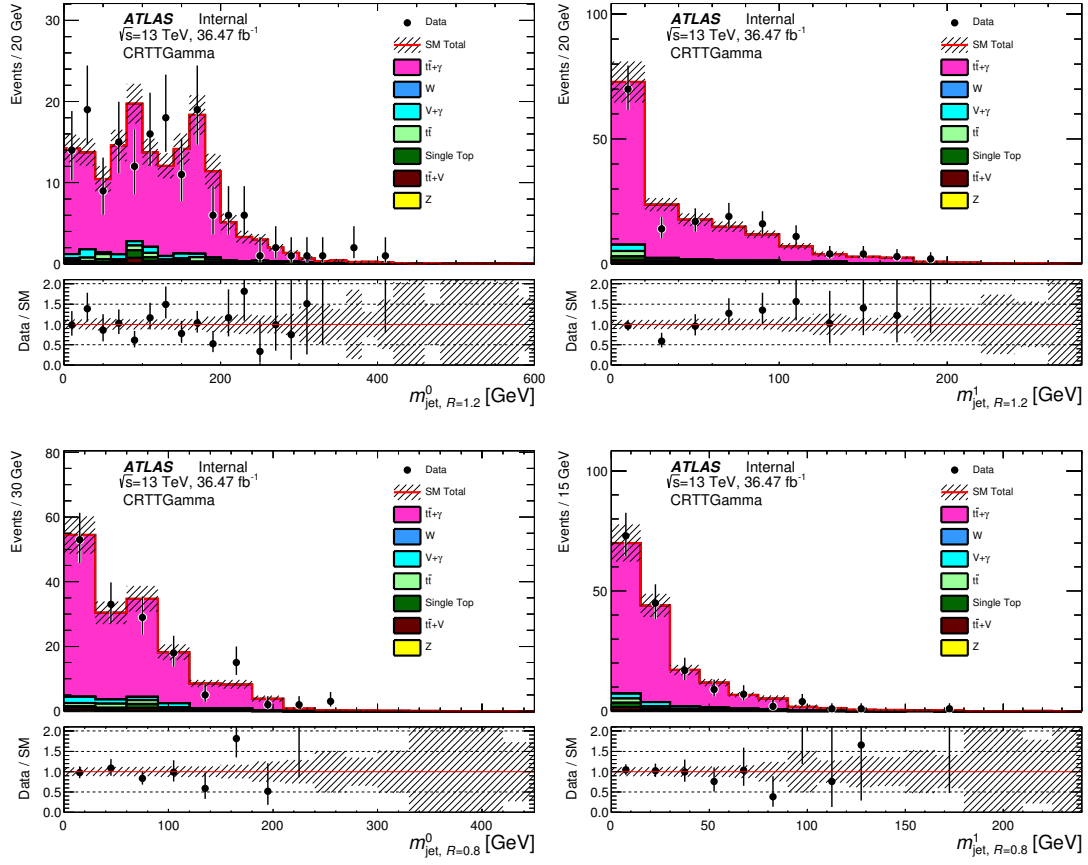


Figure 10.17: Postfit distributions of the  $p_T$  of the leading and subleading jets for the 2 b-jets selection. The ratio





**Figure 10.18:** Postfit distributions of the  $p_T$  of the leading and subleading jets for the 2 b-jets selection. The ratio between data and MC is given in the bottom panel. The hashed area in both the top and lower panel represents the uncertainty due to MC statistics.

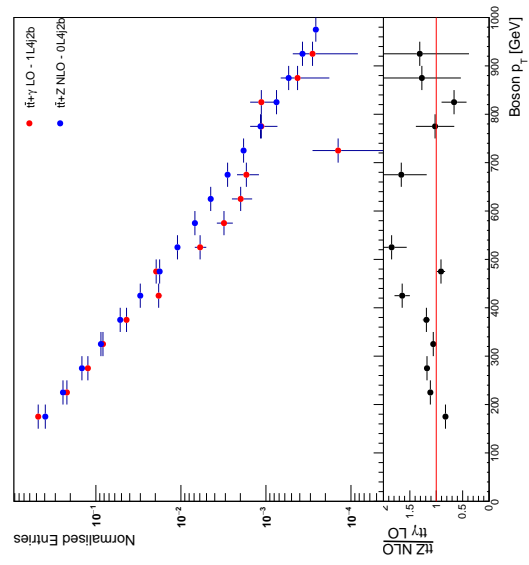


Figure 10.19: Truth  $p_T$  ratio.

#### 10.3.4 STANDARD MODEL Z+JETS

Z+jets consist of 3 percent of all backgrounds in the SR. The percentage of Z+jets is higher in high  $R_{\text{ISR}}$  bins. The percentage Z+jets rises to 7 percent in  $R_{\text{ISR}}$  between 0.6 and 0.8. We use just the MC prediction for Z+jets because the rate of Z+jet is so low. We assign an 100 percent theory uncertainty to the Z+jets rate in the SR.

The ttbar validation region described in section 10.2.4 has a larger fraction of Z+jets event than those in the SR. The ttbar VR is kinematically similar to those of the SR with some looser cuts on jet multiplicity and ISR,  $E_{\text{T}}^{\text{miss}}$  correlations. The good agreement between data and MC in the ttbar VR is evidence that the Z+jets MC cannot be wrong by more than 100 percent.

#### 10.3.5 STANDARD MODEL DIBOSON

Standard Model dibosons consist of 1 percent of the background in the signal region. The diboson background consist of less than 2 percent of any single  $R_{\text{ISR}}$  bin in the SR. The background is negligible and we only use MC predictions for background estimation.

#### 10.3.6 STANDARD MODEL QCD MULTIJET AND ALL HADRONIC $t\bar{t}$

The background from the production of multijet events and all-hadronic  $t\bar{t}$  events is estimated with the jet smearing method. The latest version of the software package (JetSmearing-00-01-26) is used and the recommendations of the jet smearing group are followed to extract the results. The jet response function is derived by the jet smearing group and used for the QCD estimate in this analysis.

## OVERVIEW OF THE METHOD

This method is based on a technique developed by the SUSY working group<sup>7</sup> and used by several analyses during Run-I and Run-II of the LHC. This method is to repeatedly smear the Lorentz vector of jets in well measured data events with small  $E_T^{\text{miss}}$  creating “pseudo-data” with potentially large  $E_T^{\text{miss}}$ .

The different stages of the method are as follows:

- Data events containing  $\geq 4$  jets of which two are b-tagged are used to select well measured “Seed Events” by defining:

$$E_T^{\text{miss sig.}} = \frac{E_T^{\text{miss}} - M}{\sum E_T}$$

Where the value of M was derived by the jet smearing group to be  $M = 8$  GeV. The motivation for this was to remove any bias in the leading  $p_T$  jet distribution of the pseudo-data.

- The JetSmearing tool is then used to smear the momentum of jets in the seed events. For each jet the Lorentz vector is multiplied by a random number derived from pre-determined jet response maps, which are provided by the JetSmearing tool.
- The operation described in the second item is repeated 5000 times for each jet in the seed event to randomly generate configurations where the  $E_T^{\text{miss}}$  comes from multiple fluctuating jets.

## SEED EVENT SELECTION

For the seed event selection, we use the derived SUSYII-datasets (jet smearing derivation) of the recorded 2015 ATLAS data and of period A and B from 2016. The events have to be recorded by any

of the HLT\_j \* triggers. Each seach event is weighted based on online leading  $p_T(\text{HLT\_xAOD\_JetContainer\_a4tcemsubj})$  and which trigger fired.

The usual cleaning cuts and a lepton veto are applied to the seed event sample (list of cuts in 10.11).

Additionally, we require at least four reconstructed jets and two  $b$ -tags.

**Table 10.11:** Seed event preselection

Cut
$n_{\text{prim.vertices}} > 0$
Jet trigger
Bad jet veto
Cosmic muon veto
Bad muon veto
Baseline lepton veto
$\geq 4$ jets
$\geq 1$ $b$ -jets
$E_T^{\text{miss}}$ sig. cut

As recommended by the jet smearing group, we use the following definition for the  $E_T^{\text{miss}}$ -significance:

$$E_T^{\text{miss}} \text{ sig.} = \frac{E_T^{\text{miss}} - 8 \text{ GeV}}{\sum E_T}$$

The cut value on this quantity depends on the number of  $b$ -tagged jets in the event:

$$E_T^{\text{miss}} \text{ sig.} < 0.3 + 0.1 \cdot n_{b\text{-jets}}$$

## SMEARING PROCEDURE

The smearing is done by the JetSmearing package. When a seed event is selected, the jet container is passed to the tool, which then returns a predefined number of smeared jet containers. For each pseudo-event, the  $E_T^{\text{miss}}$  is rebuilt with the smeared jets.

The package is used with the default properties, but  $\Delta\phi$  smearing of the jets is activated.

The systematic uncertainty is obtained by varying the selection of seed events. For an upward error we select all events passing  $E_T^{\text{miss}} \text{ sig.} < 0.6 + 0.2 \cdot n_{\text{n-bjets}}$  and for the downward error  $E_T^{\text{miss}} \text{ sig.} < 0.2 + 0.05 \cdot n_{\text{n-bjets}}$ . The total systematic uncertainty is calculated from the maximum of the up/down variations with respect to the nominal. This is then added in quadrature with a flat 30% systematic uncertainty.

The 30% uncertainty is assumed from Run-I low-side-tail modifications of the jet response. **CM:**  
these are coming soon!

## PRESELECTION

To estimate the multi-jet contribution, we stick close to the signal region cuts, loosen the  $E_T^{\text{miss}}$  requirement and invert the cut on  $\min |\Delta\phi(\text{jet}^{0-1}, E_T^{\text{miss}})|$ . A detailed list of cuts is shown in 10.12. A selection of distributions in the CRQCD is shown in Fig. ??, Fig. ??, Fig. ?? and Fig. ??.

A common CR and VR for each SRC are defined before any selection on  $R_{\text{ISR}}$ . The QCD control region is defined in a region with  $0.2 > \min |\Delta\phi(\text{jet}^{0-1}, E_T^{\text{miss}})| > 0.05$  due to contamination from the targeted signals and from possible sources of  $E_T^{\text{miss}}$  not modelled well by the JetSmearing

**Table 10.12:** QCD control region cuts

Cut
Trigger: HLT_xe70_tc_lcw (2015) and HLT_xe90_mht_L1XE50
$n_{\text{prim.vertices}} > 0$
Bad jet veto
Cosmic muon veto
Bad muon veto
Baseline lepton veto
$\geq 4$ jets
$\geq 2$ $b$ -jets
$E_T^{\text{miss}} > 200 \text{ GeV}$
$\min  \Delta\phi(\text{jet}^{0-1}, E_T^{\text{miss}})  < 0.4$

technique ( $E_T^{\text{miss}}$  from jets that fail tight-jet cleaning). To further increase the statistics and the QCD purity, an inverted selection on  $R_{\text{ISR}} < 0.3$  is applied. The  $\Delta\phi_{\text{ISR}, E_T^{\text{miss}}} > 3.00$  cut is reduced to  $> 2.00$ ,  $p_T^{\text{ISR}} > 400 \text{ GeV}$  is reduced to  $p_T^{\text{ISR}} > 150 \text{ GeV}$  and the selection of  $m_S > 300 \text{ GeV}$  is removed. For the validation region the interval  $[0.1, 0.2]$  is used for the selection on  $\min |\Delta\phi(\text{jet}^{0-1}, E_T^{\text{miss}})|$ ,  $\Delta\phi_{\text{ISR}, E_T^{\text{miss}}} > 2.00$  and  $R_{\text{ISR}} < 0.3$  are both used to increase statistics and reduce signal contamination.

An overview of the selections can be found in Table ??.

**Table 10.13:** QCD C definitions, in addition to the requirements presented in Table ??.

Variable	CR	VR
$\min  \Delta\varphi(\text{jet}^{\text{o-1}}, E_{\text{T}}^{\text{miss}}) $	$[0.05, 0.1]$	$[0.1, 0.2]$
$N_{\text{b-jet}}^{\text{s}}$	$\geq 1$	
$N_{\text{jet}}^{\text{s}}$	$\geq 5$	
$p_{\text{T},b}^{\text{o},\text{s}}$	$> 40 \text{ GeV}$	
$m_{\text{S}}$	-	$> 300 \text{ GeV}$
$\Delta\varphi_{\text{ISR}, E_{\text{T}}^{\text{miss}}}$	$> 2.00$	$> 3.00$
$p_{\text{T}}^{\text{ISR}}$	$> 150 \text{ GeV}$	$> 400 \text{ GeV}$
$R_{\text{ISR}}$	$< 0.4$	
$p_{\text{T}}^{4,\text{s}}$	$> 50 \text{ GeV}$	
b-tagged jets	$\geq 1$	



# 11

## Systematic Uncertainties

Systematic uncertainties are associated with the predictions of all background components and the expected signal yields. The systematic uncertainties can be categorized into two sources: experimental and theoretical uncertainties. These systematic uncertainties can impact the expected event yields in the control and signal region as well as the transfer factors used when extrapolating the background expectation from the control to the signal region.

This section overviews the systematic uncertainties considered and their determination in Sections 11.0.1 and 11.0.2, and the size in Section ??.

## 11.0.1 EXPERIMENTAL UNCERTAINTIES

Jet Energy Scale (JES) and Jet Energy Resolution (JER) The two main uncertainties for jets are uncertainties affecting the JES calibration and the JER. The final jet energy calibration generally referred as JES is a correction relating the calorimeter's response to the true jet energy. The JES uncertainty is derived in bins of  $p_T$  and  $\eta$  from different in-situ techniques<sup>?</sup> by the Jet/ETmiss group, updated plots can be found in Ref.<sup>?</sup>. These variations, up and down, are estimated via the `JETUncertainties` tool. Also uncertainties related to flavour composition and pile-up are included. Following the recommendation from Jet/ETmiss group, split-JES components are employed in order to reduce the total JES by the proper correlations of the components. It is possible to use the full list of nuisance parameters (77 components), a reduced set where the components are combined to give a total of 19 or 25 parameters, or a strongly reduced set where only 4 nuisance parameters (5 for AF-II samples) are left after the combination. In appendix ?? it is shown that the differences in the distributions between jets calibrated with nominal and varied JES do not depend on the choice of the reduced nuisance-parameters set, therefore the `JES2015_SR_Scenario1` list of strongly reduced parameters will be used to determine the JES uncertainties affecting this search.

The JER uncertainty is derived as one-side variation by comparing data to MC simulation via the di-jet balance and bi-sectors techniques<sup>?</sup> and the variation in this analysis is estimated by

smearing all jets momenta in simulation events with the `JetResolution` tool.

*b*-tagging The *b*-tagging uncertainty has large contribution to both signal and backgrounds because of the two *b*-tagged jets requirement. Scale factor uncertainties in *b*-tagging are derived by the flavor-tagging working group, depending on the kinematics of the jet and also on the jet flavor. Three kinds of uncertainties on the *b*-jet weight, up and down, are calculated, propagating the estimated uncertainties on the scale factors for *b*-jets as well as a mis-tagging correction to *c*-jets and light-flavor jets.

$E_T^{\text{miss}}$  Soft-term Resolution and Scale The scale and resolution uncertainties of individual objects need to be propagated to  $E_T^{\text{miss}}$  via the `METUtilities` tool. Specific systematic uncertainties on the scale and resolution of the  $E_T^{\text{miss}}$  soft term have been derived by two different in-situ methods using  $Z \rightarrow \mu\mu$  events<sup>7</sup> and considered in this analysis.

Lepton efficiencies Lepton reconstruction and identification efficiencies have contributions to the backgrounds. For electrons, the uncertainties originate from the *e*/gamma resolution and scale and from the electron reconstruction efficiency. Similarly, for muons the uncertainties originate from the muon resolution and reconstruction efficiency, the isolation and the momentum scale. The lepton trigger scale factors are also taken into consideration.

Pileup The uncertainty due to pileup re-weighting is considered as two-sided variation in the event weights.

## II.O.2 THEORETICAL UNCERTAINTIES

Theory uncertainties affecting the background normalization and kinematic distribution shapes largely impact the background prediction in the signal regions, as they directly affect the background normalization and acceptance times efficiency. If a background normalization is determined by making use of dedicated control regions, then only systematics affecting the analysis acceptance are relevant. Statistical uncertainties in the evaluation of systematics are neglected in general; where necessary, selection cuts are loosened to make the systematic comparison statistically meaningful. The remainder of this section is dedicated to the discussion on how the theory systematic uncertainties have been derived for each of the background processes considered.

The theoretical uncertainty in each signal region is evaluated by considering variations with respect to the default settings and choices for the event generation. For each of the variations considered, the systematic uncertainty is estimated as an uncertainty on the so-called transfer factor, that is, the ratio of the predicted yields between the signal region and the  $t\bar{t}$  control region(s). For a given control - signal region pair, the transfer factor  $T_f$  is defined by:

$$T_f = \frac{N_{\text{SR}}}{N_{\text{CR}}} \quad (\text{II.1})$$

$Z + jets$  For the estimation of the  $Z$  production background, the SHERPA generator is used by default. To assess the theory systematic uncertainties due to scale variations with good statistical power seven LHE<sub>3</sub> weights are used.

The theory uncertainty on the normalisation of the  $Z$  production is obtained by comparing the SHERPA predictions on the transfer factor between the control region and the signal region with and without systematic weights applied. The uncertainty on the transfer factor is computed with the following equation:

$$\Delta_X = \frac{T_f^{\text{up}} - T_f^{\text{down}}}{T_f^{\text{up}} + T_f^{\text{down}}} \quad (11.2)$$

, where  $X$  is the systematic variation. Tables 11.1 summarises the values of the transfer factors obtained for SHERPA systematics for all signal regions, together with the resulting relative uncertainty.

The  $Z + jets$  theory uncertainty is denoted by `theoSysZ` in the fit.

SR	uncertainty (%)
SRA-TT	35.7
SRA-TW	36.2
SRA-To	36.7
SRB-TT	35.0
SRB-TW	32.1
SRB-To	28.4
SRD-low	36.5
SRD-high	36.5
SRE	36.5
VRZAB	22.0
VRZD	34.6
VRZE	31.4

**Table 11.1:** Summary of the theory uncertainties (in percent) on  $Z$  production obtained on the transfer factor for all signal regions except for SRC for which the  $Z$  background is negligible. The largest uncertainty is below 37% in SRA-To.

$W + jets$  A similar approach is performed to assess the  $W$ +jets theory uncertainties. No additional

uncertainty due to possible  $W + c$  contribution in CRW which has a one  $b$ -jet requirement (compared to the 2b requirement). It was found that the flavor contribution in the VRW (which also has a two b-jet requirement) is very similar to the SR. The postfit MC from VRW match the observed data well which leads us to believe that the  $W + c$  contribution in CRW has a negligible effect on the normalization factor. The details are described in Section 10.3.1.

Table 11.2 summarises the values of the transfer factors obtained for SHERPA systematics for all signal regions, together with the resulting relative uncertainty.

These  $W$  theory uncertainties are denoted by  $\text{theoSysW}$ ,  $\text{theoSysWc}$  in the fit, respectively.

SR	uncertainty (%)
SRA-TT	9.5
SRA-TW	8.0
SRA-To	6.1
SRB-TT	9.1
SRB-TW	7.9
SRB-To	3.3
SRC <sub>1</sub>	11.4
SRC <sub>2</sub>	12.5
SRC <sub>3</sub>	11.8
SRC <sub>4</sub>	10.7
SRC <sub>5</sub>	9.5
SRC <sub>6</sub>	11.3
SRD-low	8.8
SRD-high	8.2
SRE	9.5
VRW	1.9

**Table 11.2:** Summary of the theory uncertainties (in percent) on  $W$  production obtained on the transfer factor for all signal regions. The largest uncertainty is 13%.

$t\bar{t}$  production Most  $t\bar{t}$  uncertainties are estimated by comparing variations at reco level. The hard scattering generation uncertainty however is estimated using truth quantities. In this case,

the yields are estimated by repeating the analysis at particle level. The object definitions for the particle level analysis are described in Appendix ??.

The recommended variations<sup>3</sup> of the event generation considered are summarized below, with details about how the corresponding uncertainty has been evaluated.

- Hard scatter generation: An uncertainty on the hard scattering generation is computed by comparing the MC@NLOPYTHIA with DSID 410225 and PowHegPYTHIA with DSID 410000, 407012. In this case, the uncertainty is given by:

$$\Delta_{\text{hard scatter}} = \frac{T_f^{\text{PowHeg}} - T_f^{\text{MC@NLO}}}{T_f^{\text{PowHeg}}} \quad (11.3)$$

A sample generated using SHERPA 2.2.1 was also considered for this uncertainty.

- Parton shower: An uncertainty on the choice of the showering model is computed by comparing the baseline DSID 410000, 407012 (that is, PowHegPYTHIA with the P2011C tuning for PYTHIA, where the two DSIDs correspond to the inclusive and high  $E_T^{\text{miss}}$ -sliced samples) and DSID 410004 (that is, PowHegHERWIG++ with the UE5C6L1 CT10 tuning for HERWIG++). In this case, the uncertainty is given by:

$$\Delta_{\text{PS}} = \frac{T_f^{\text{PYTHIA}} - T_f^{\text{HERWIG++}}}{T_f^{\text{PYTHIA}}} \quad (11.4)$$

- ISR/FSR: Uncertainties related to the emission of additional partons in the initial or final states are evaluated by comparing the radHi and radLow PowHegPYTHIA samples with DSID 410002 and 410001. The uncertainty is calculated with eq 11.2.

Tables 11.3, 11.4, 11.5, 11.6, 11.6, 11.4, 11.8, 11.9, 11.10 and 11.11 summarise the  $t\bar{t}$  systematic uncertainties obtained by the comparisons described above for the different control, signal and validation regions in this analysis. Control regions in which the  $t\bar{t}$  background is negligible

are not considered. The results for the single top control region are found in Table 11.8, while results for CRW are in Table 11.11.

In general, limited statistics of the MC@NLOPYTHIA and SHERPA samples result in very large values of the generator uncertainty. In the SRA signal regions, all  $t\bar{t}$  systematic uncertainties are limited by statistics of the relevant samples. For regions where sufficient statistics are available, the uncertainties typically range from a few % to 30%.

The  $t\bar{t}$  theory uncertainty is denoted by `theoSysTop` in the fit.

	CRA-TT	SRA-TT	VRTopATT
ttbar	$69.5 \pm 2.9$	$0.36 \pm 0.20$	$55.0 \pm 2.7$
ttbar (rad up)	$81.1 \pm 3.5$	$1.32 \pm 0.35$	$80.0 \pm 3.3$
ttbar (rad down)	$58.8 \pm 3.0$	$0.29 \pm 0.13$	$48.9 \pm 2.5$
ttbar (Powheg+H++)	$60.1 \pm 2.8$	$0.59 \pm 0.20$	$57.2 \pm 2.4$
ttbar (aMC@NLO+P8)	$63 \pm 16$	$< 0.01$	$32 \pm 18$
ttbar (Sherpa)	$73 \pm 10$	$< 0.01$	$79 \pm 11$
Transfer factors (in %)			
ISR/FSR		53	9
PS		90	20
Generator (aMC@NLO)		-	40
Generator (Sherpa)		-	37

**Table 11.3:** Theory uncertainties for the  $t\bar{t}$  background for the SRA-TT regions.

$t\bar{t} + W/Z$  The  $t\bar{t}+W/Z$  theory uncertainties on yields of  $t\bar{t} + W/Z$  have been determined by performing the analysis with several variations at particle level. The particle-level object definitions are the same as for  $t\bar{t}$ . The systematic uncertainty is calculated as the difference in yields in due to the variations.

Following the recommendations of the background forum, a global 13% uncertainty on the production cross section and, therefore, on the global normalisation of the MC samples is



	CRA-TW	SRA-TW	VRTopATW
ttbar	$119.0 \pm 3.5$	$0.66 \pm 0.22$	$48.4 \pm 2.7$
ttbar (rad up)	$111 \pm 4$	$0.43 \pm 0.16$	$50.1 \pm 2.6$
ttbar (rad down)	$121 \pm 4$	$0.59 \pm 0.25$	$42.0 \pm 2.0$
ttbar (Powheg+H++)	$91.7 \pm 3.0$	$0.61 \pm 0.21$	$40.0 \pm 2.3$
ttbar (aMC@NLO+P8)	$101 \pm 19$	$< 0.01$	$20 \pm 11$
ttbar (Sherpa)	$121 \pm 19$	$0.5 \pm 0.5$	$44 \pm 8$
Transfer factors (in %)			
ISR/FSR		11	13
PS		20	7
Generator (aMC@NLO)		-	51
Generator (Sherpa)		-	11

**Table 11.4:** Theory uncertainties for the  $t\bar{t}$  background for the SRA-TB regions.

	CRA-T <sub>0</sub>	SRA-T <sub>0</sub>	VRTopAT <sub>0</sub>
ttbar	$76.2 \pm 2.9$	$1.9 \pm 0.6$	$58.3 \pm 2.5$
ttbar (rad up)	$70.1 \pm 2.8$	$0.80 \pm 0.29$	$56.8 \pm 2.8$
ttbar (rad down)	$85.1 \pm 3.2$	$0.50 \pm 0.19$	$63.9 \pm 2.5$
ttbar (Powheg+H++)	$60.2 \pm 2.6$	$1.0 \pm 0.5$	$42.4 \pm 2.1$
ttbar (Sherpa)	$61 \pm 12$	$0.7 \pm 0.7$	$53 \pm 10$
Transfer factors (in %)			
ISR/FSR		32	4
PS		30	8
Generator (aMC@NLO)		-	68
Generator (Sherpa)		-	14

**Table 11.5:** Theory uncertainties for the  $t\bar{t}$  background for the SRA-T0 regions.

considered. On top of this, further uncertainties on the acceptance of the selection have been considered:

- Scale variations are used to estimate the uncertainty on the ttV yield due to various scales.
- Generator Samples produced with the SHERPA generator are compared with the default MadGraph generated samples.

Table 11.12 shows the estimated systematic uncertainties for all variations. Also mentioned earlier is the 13% uncertainty on the total cross section, together with the total estimated un-

	CRB-TT	SRB-TT	VRTopBTT
ttbar	$64.0 \pm 2.8$	$6.5 \pm 0.8$	$96.3 \pm 3.5$
ttbar (rad up)	$70.9 \pm 3.0$	$11.2 \pm 1.3$	$133 \pm 5$
ttbar (rad down)	$54.2 \pm 2.5$	$4.3 \pm 0.7$	$87.8 \pm 3.4$
ttbar (Powheg+H++)	$53.3 \pm 2.3$	$7.5 \pm 0.8$	$101 \pm 4$
ttbar (aMC@NLO+P8)	$58 \pm 17$	$9 \pm 11$	$48 \pm 26$
ttbar (Sherpa)	$66 \pm 9$	$6.3 \pm 2.6$	$123 \pm 13$
Transfer factors (in %)			
ISR/FSR		33	7
PS		39	26
Generator (aMC@NLO)		50	45
Generator (Sherpa)		10	24

**Table 11.6:** Theory uncertainties for the  $t\bar{t}$  background for the SRB-TT regions.

	CRB-TW	SRB-TW	VRTopBTW
ttbar	$265 \pm 6$	$12.8 \pm 1.1$	$119 \pm 4$
ttbar (rad up)	$241 \pm 6$	$18.5 \pm 2.1$	$129 \pm 5$
ttbar (rad down)	$275 \pm 6$	$10.7 \pm 1.1$	$121 \pm 4$
ttbar (Powheg+H++)	$200 \pm 4$	$11.6 \pm 1.3$	$107 \pm 4$
ttbar (aMC@NLO+P8)	$256 \pm 33$	$6 \pm 9$	$88 \pm 24$
ttbar (Sherpa)	$278 \pm 26$	$16 \pm 5$	$119 \pm 13$
Transfer factors (in %)			
ISR/FSR		33	10
PS		20	19
Generator (aMC@NLO)		50	23
Generator (Sherpa)		20	5

**Table 11.7:** Theory uncertainties for the  $t\bar{t}$  background for the SRB-TW regions.

certainty, obtained as the sum in quadrature of the individual uncertainties.

The largest uncertainties are 35% and 24% in SRC<sub>1</sub> and SRC<sub>5</sub>, respectively. This is expected due to the low number of  $t\bar{t} + W/Z$  events falling in such regions. However, in the regions where such background is more significant, such as SRA, SRB, and SRD, the largest uncertainties are 5.2%, 5.0%, and 6.5%, respectively.

The  $t\bar{t} + W/Z$  theory uncertainty is denoted by theoSysTtbarV in the fit.

	CRB-T0	CRST	SRB-T0	VRTopBT0
ttbar	432 ± 7	34.2 ± 2.1	45.8 ± 2.6	159 ± 5
ttbar (rad up)	382 ± 13	39.2 ± 2.7	47.6 ± 3.0	139 ± 5
ttbar (rad down)	457 ± 7	28.7 ± 1.9	36.6 ± 2.2	153 ± 5
ttbar (Powheg+H++)	308 ± 6	27.9 ± 1.8	39.6 ± 2.4	122 ± 4
ttbar (aMC@NLO+P8)	380 ± 40	59 ± 16	59 ± 20	100 ± 22
ttbar (Sherpa)	376 ± 29	37 ± 8	58 ± 15	144 ± 17
Transfer factors (in %)				
ISR/FSR		24	22	4.2
PS		14	21	8
Generator (aMC@NLO)		100	50	29
Generator (Sherpa)		24	50	4

**Table 11.8:** Theory uncertainties for the  $t\bar{t}$  background for the SRB-T0 regions.

	CRTopC	SRC1	SRC2	SRC3	SRC4	SRC5	VRTopC
ttbar	668 ± 9	16.7 ± 1.6	31.7 ± 2.1	21.7 ± 1.6	6.3 ± 0.8	0.60 ± 0.23	232 ± 5
ttbar (rad up)	872 ± 11	25.2 ± 2.3	39.5 ± 2.3	28.7 ± 2.1	8.6 ± 1.0	1.05 ± 0.33	293 ± 7
ttbar (rad down)	521 ± 9	10.1 ± 1.0	19.2 ± 1.6	15.8 ± 1.5	6.3 ± 1.2	0.7 ± 0.4	187 ± 5
ttbar (Powheg+H++)	621 ± 10	16.3 ± 1.8	27.8 ± 1.8	18.0 ± 1.5	6.5 ± 0.9	0.46 ± 0.18	206 ± 5
ttbar (aMC@NLO+P8)	310 ± 60	6 ± 5	< 0.01	4 ± 7	1 ± 5	0.9 ± 0.9	113 ± 34
ttbar (Sherpa)	840 ± 40	30 ± 8	42 ± 9	22 ± 5	7.4 ± 3.2	< 0.01	297 ± 30
Transfer factors (in %)							
ISR/FSR		20	10	4	10	5	3.3
PS		5	6	11	11	20	4
Generator (aMC@NLO)		20	110	60	70	220	0
Generator (Sherpa)		40	5	19	10	100	2

**Table 11.9:** Theory uncertainties for the  $t\bar{t}$  background for the SRC regions.

**Single-top** The single-top background in the signal region is dominated by the  $Wt$  subprocess. The

following comparisons are made to evaluate the uncertainty on the transfer factor.

- Parton shower: An uncertainty on the choice of the showering model is computed by comparing the baseline DSID 410013, 407014 (that is, PowHegPYTHIA with the P2011 tuning for PYTHIA, where the two DSIDs correspond to the top and antitop samples) and DSID 410147, 410148 (that is, PowHegHERWIG++ with the UE5C6L1 CT10 tuning for HERWIG++ and similar  $E_T^{\text{miss}}$  slicing). In this case, the uncertainty is given by equation 11.4.

	CRTopD	CRW	SRD-low	SRD-high	VRTopD
ttbar	$134 \pm 4$	$128 \pm 4$	$3.2 \pm 0.5$	$0.73 \pm 0.23$	$159 \pm 4$
ttbar (rad up)	$143 \pm 5$	$135 \pm 5$	$5.0 \pm 0.7$	$1.38 \pm 0.35$	$164 \pm 5$
ttbar (rad down)	$132 \pm 4$	$117 \pm 4$	$2.6 \pm 0.4$	$1.4 \pm 0.4$	$148 \pm 4$
ttbar (Powheg+H++)	$93.0 \pm 3.3$	$87.9 \pm 3.1$	$3.6 \pm 0.6$	$1.30 \pm 0.33$	$117 \pm 4$
ttbar (aMC@NLO+P8)	$145 \pm 22$	$218 \pm 25$	$9 \pm 5$	$3.5 \pm 2.4$	$106 \pm 32$
ttbar (Sherpa)	$119 \pm 15$	$131 \pm 14$	$5.5 \pm 2.9$	$1.5 \pm 1.5$	$150 \pm 14$
Transfer factors (in %)					
ISR/FSR		3.2	28	5	1.1
PS		1	62	160	6
Generator (aMC@NLO)		57	160	340	38
Generator (Sherpa)		15	90	130	6

**Table 11.10:** Theory uncertainties for the  $t\bar{t}$  background for the SRD regions.

	CRTopE	SRE	VRTopE
ttbar	$42.5 \pm 2.4$	$0.45 \pm 0.21$	$66.5 \pm 2.9$
ttbar (rad up)	$53.4 \pm 2.7$	$0.53 \pm 0.19$	$84.1 \pm 3.5$
ttbar (rad down)	$35.4 \pm 2.2$	$0.6 \pm 0.4$	$60 \pm 4$
ttbar (Powheg+H++)	$36.4 \pm 1.9$	$0.38 \pm 0.20$	$72.6 \pm 3.0$
ttbar (aMC@NLO+P8)	$34 \pm 11$	$< 0.01$	$44 \pm 13$
ttbar (Sherpa)	$45 \pm 8$	$0.6 \pm 0.6$	$74 \pm 10$
Transfer factors (in %)			
ISR/FSR		30	4
PS		0	27
Generator (aMC@NLO)		100	44
Generator (Sherpa)		30	5

**Table 11.11:** Theory uncertainties for the  $t\bar{t}$  background for the SRE regions.

- ISR/FSR: Uncertainties related ISR/FSR are evaluated by comparing the radHi and radLow PowHegPYTHIA samples with DSID 410099, 410101 and 410100, 410102, where the two sets of DSIDs represent the top and antitop final states. The formula used is equation 11.2.

The uncertainties resulting from these comparisons are summarized in Tables 11.13, 11.14, 11.15, 11.13, for SRA, SRB, SRC, SRD, SRE and associated control regions, respectively.

The single-top theory uncertainty is denoted by `theoSysSingleTop` in the fit.

SR	uncertainty (%)
SRA-TT	5.2
SRA-TW	4.0
SRA-To	0.8
SRB-TT	3.3
SRB-TW	5.0
SRB-To	1.2
SRC <sub>1</sub>	35.3
SRC <sub>2</sub>	5.5
SRC <sub>3</sub>	6.6
SRC <sub>4</sub>	19.7
SRC <sub>5</sub>	23.7
SRD-low	3.4
SRD-high	6.5
SRE	2.7

**Table 11.12:** Summary of the theory uncertainties (in percent) on  $t\bar{t} + W/Z$  production obtained on the transfer factor on all the signal regions. The uncertainties are symmetrised, and all numbers are given in percentages.

	CRST	CRTopATT	CRTopATW	CRTopATo	SRA-TT	SRA-TW	S
st Wt (MET <sub>200</sub> )	41.7 ± 1.1	6.0 ± 0.4	3.94 ± 0.35	3.17 ± 0.31	3.35 ± 0.33	2.39 ± 0.27	4.
st Wt (radHi, MET <sub>200</sub> )	50.4 ± 1.3	8.0 ± 0.5	5.0 ± 0.4	4.1 ± 0.4	5.5 ± 0.4	4.4 ± 0.4	5.
st Wt (radLo, MET <sub>200</sub> )	34.9 ± 1.0	4.7 ± 0.4	3.75 ± 0.33	2.56 ± 0.28	2.25 ± 0.25	1.99 ± 0.24	2.8
st Wt (Powheg+H <sup>++</sup> , MET <sub>200</sub> )	39.2 ± 1.0	5.6 ± 0.4	3.15 ± 0.30	2.39 ± 0.27	2.77 ± 0.28	2.58 ± 0.27	4.0
st Wt (DS, MET <sub>200</sub> )	6.8 ± 0.4	0.81 ± 0.13	1.42 ± 0.17	1.14 ± 0.16	0.059 ± 0.034	0.08 ± 0.04	0.0
Transfer factors (in %)							
ISR/FSR		8 ± 6	4 ± 6	5 ± 8	26 ± 7	21 ± 8	
PS		1 ± 10	15 ± 13	20 ± 14	12 ± 14	15 ± 17	
Inteference (DR vs DS)		17 ± 16	121 ± 33	120 ± 40	89 ± 15	79 ± 18	9

**Table 11.13:** Summary of the single-top theory uncertainties obtained in each of the signal regions. The uncertainties are symmetrised, and all numbers are given in percentages. Note that the event yields and transfer factors are obtained from truth-level samples.

A 100% uncertainty due to interference is applied for single top.

The Remaining Background Components A 50% uncertainty is used for the dibosons estimate.

Signal Component **Coming soon**

	CRST	CRTopBTT	CRTopBTW	CRTopBT <sub>0</sub>	SRB-TT	SRB-TW	SRB-T <sub>0</sub>
st Wt (MET <sub>200</sub> )	41.7 ± 1.1	7.3 ± 0.5	7.9 ± 0.5	12.0 ± 0.6	11.4 ± 0.6	15.1 ± 0.7	53.8 ± 1.1
st Wt (radHi, MET <sub>200</sub> )	50.4 ± 1.3	9.6 ± 0.6	9.8 ± 0.6	13.4 ± 0.7	15.4 ± 0.7	19.8 ± 0.8	59.9 ± 1.3
st Wt (radLo, MET <sub>200</sub> )	34.9 ± 1.0	5.8 ± 0.4	7.7 ± 0.5	10.5 ± 0.6	8.8 ± 0.5	11.5 ± 0.6	48.5 ± 1.0
st Wt (Powheg+H++,MET <sub>200</sub> )	39.2 ± 1.0	6.5 ± 0.4	7.1 ± 0.4	9.3 ± 0.5	10.7 ± 0.5	14.7 ± 0.6	44.9 ± 1.0
st Wt (DS,MET <sub>200</sub> )	6.8 ± 0.4	0.90 ± 0.14	3.04 ± 0.25	5.70 ± 0.35	0.67 ± 0.12	1.73 ± 0.20	9.0 ± 0.4
Transfer factors (in %)							
ISR/FSR		7 ± 5	6 ± 5	6 ± 4	10 ± 4	9 ± 4	7.8 ± 2.1
PS		5 ± 10	4 ± 9	18 ± 8	0 ± 8	4 ± 7	11 ± 5
Interference (DR vs DS)		24 ± 15	136 ± 27	191 ± 28	64 ± 10	30 ± 11	3 ± 9

**Table 11.14:** Summary of the single-top theory uncertainties obtained in each of the signal regions. The uncertainties are symmetrised, and all numbers are given in percentages. Note that the event yields and transfer factors are obtained from truth-level samples.

	CRST	SRC <sub>1</sub>	SRC <sub>2</sub>	SRC <sub>3</sub>	SRC <sub>4</sub>	SRC <sub>5</sub>	VRT <sub>0</sub>
st Wt (MET <sub>200</sub> )	41.7 ± 1.1	0.66 ± 0.14	1.14 ± 0.18	0.99 ± 0.17	0.39 ± 0.11	0.12 ± 0.06	19.9 ± 1.1
st Wt (radHi, MET <sub>200</sub> )	50.4 ± 1.3	0.60 ± 0.14	1.26 ± 0.20	1.33 ± 0.21	0.57 ± 0.14	0.25 ± 0.09	21.9 ± 1.3
st Wt (radLo, MET <sub>200</sub> )	34.9 ± 1.0	0.57 ± 0.13	0.77 ± 0.15	0.77 ± 0.15	0.37 ± 0.10	0.09 ± 0.05	16.9 ± 1.0
st Wt (Powheg+H++,MET <sub>200</sub> )	39.2 ± 1.0	0.62 ± 0.13	0.84 ± 0.16	0.79 ± 0.15	0.38 ± 0.10	0.08 ± 0.05	18.7 ± 1.0
st Wt (DS,MET <sub>200</sub> )	6.8 ± 0.4	0.12 ± 0.05	0.30 ± 0.09	0.23 ± 0.08	0.16 ± 0.06	0.020 ± 0.020	4.39 ± 0.4
Transfer factors (in %)							
ISR/FSR		16 ± 17	6 ± 13	9 ± 13	3 ± 18	32 ± 32	5.4 ± 5.4
PS		0 ± 30	22 ± 22	15 ± 24	0 ± 40	30 ± 70	0 ± 30
Interference (DR vs DS)		10 ± 50	60 ± 50	40 ± 50	150 ± 110	0 ± 110	35 ± 35

**Table 11.15:** Summary of the single-top theory uncertainties obtained in each of the signal regions. The uncertainties are symmetrised, and all numbers are given in percentages. Note that the event yields and transfer factors are obtained from truth-level samples.

	CRST	CRW	SRD-low	SRD-high	VRTopD
Transfer factors (in %)					

**Table 11.16:** Summary of the single-top theory uncertainties obtained in each of the signal regions. The uncertainties are symmetrised, and all numbers are given in percentages. Note that the event yields and transfer factors are obtained from truth-level samples.

	CRST	SRE	VRTopE
st Wt (MET <sub>200</sub> )	$41.7 \pm 1.1$	$0.93 \pm 0.17$	$2.81 \pm 0.29$
st Wt (radHi, MET <sub>200</sub> )	$50.4 \pm 1.3$	$1.77 \pm 0.24$	$3.57 \pm 0.34$
st Wt (radLo, MET <sub>200</sub> )	$34.9 \pm 1.0$	$0.37 \pm 0.10$	$2.10 \pm 0.25$
st Wt (Powheg+H++, MET <sub>200</sub> )	$39.2 \pm 1.0$	$0.73 \pm 0.15$	$2.77 \pm 0.27$
st Wt (DS, MET <sub>200</sub> )	$6.8 \pm 0.4$	$< 0.01$	$0.89 \pm 0.14$
Transfer factors (in %)			
ISR/FSR		$54 \pm 14$	$8 \pm 8$
PS		$16 \pm 25$	$5 \pm 15$
Interference (DR vs DS)		$100 \pm 26$	$90 \pm 40$

**Table 11.17:** Summary of the single-top theory uncertainties obtained in each of the signal regions. The uncertainties are symmetrised, and all numbers are given in percentages. Note that the event yields and transfer factors are obtained from truth-level samples.

# 12

## Statistical Analysis

### 12.1 INTRODUCTION TO LOG LIKELIHOOD FITTING

We check the consistency of data to predicted SM background and extract information on any potential signal using log likelihood fitting. The basic premise behind log likelihood fitting is that the parameters most likely to describe the data is the one that maximizes the total likelihood defined in equation 12.1.



$$\mathcal{L}(\vec{z}) = \prod_{i=1}^n P(x_i|\vec{z}) \quad (12.1)$$

Where  $x_i$  are data points and  $\vec{z}$  are a list of parameters, and  $P(x|\vec{z})$  is the fitted probability density function (PDF). The PDF  $P(x|\vec{z})$  have the probability of producing the a dataset  $x_i$  when the likelihood is maximized.

Maximizing the likelihood is equivalent to minimizing the negative log likelihood or NLL since logarithms are a monotonically increasing functions. Therefore, we tend to minimize the NLL  $\mathcal{M}$  defined in equation 12.2

$$\mathcal{M}(\vec{z}) = -\ln(\mathcal{L}(\vec{z})) = -\sum_{i=1}^n \ln(P(x_i|\vec{z})) \quad (12.2)$$

In collider physics we do not know the total number of  $n$  events a priori. Instead, we have an expected value of events proportional to the cross-section times luminosity. This means the actual number of measured events should vary according to a poisson distribution. We include this uncertainty in the number of final observed events by multiplying a poisson distribution with expected rate  $\lambda$  to the likelihood in equation 12.1 resulting in equation 12.3.

$$\mathcal{L}(\vec{z}) = \left\{ \frac{\exp^{-\lambda}}{n!} \right\} \prod_{i=1}^n P(x_i|\vec{z}) \quad (12.3)$$

Finally, for this particular analysis we perform a binned fit to the  $R_{\text{ISR}}$  distribution in the signal region instead of an event by event shape fit. Therefore our fitted PDF  $(x_i|\vec{z})$  is not a full continuous

function but a series of expected values in discrete bins. Therefore  $P(x|\vec{z})$  can be written as equation

12.4.

$$P_{b_i} = P(x_i|\vec{z}) = \int_{b_{i-1}}^{b_i} f(x|\vec{z}) \quad (12.4)$$

Where  $f(x|\vec{z})$  is the continuous PDF,  $b_i$  and  $b_{i-1}$  are the bin edges for the  $i$ th bin. Assuming a poisson distribution of events in each bin, the extended likelihood and NLL becomes equation 12.5 and 12.6.

$$\mathcal{L}(N_{b_i}^{data}|\vec{z}) = \prod_{k=1}^{n_{bins}} \frac{(\lambda P_{b_i})^{N_{b_i}^{data}} e^{-\lambda P_{b_i}}}{N_{b_i}^{data}!} \quad (12.5)$$

$$\mathcal{M}(\vec{z}) = -\ln(\mathcal{L}(\vec{z})) = -\sum_{i=1}^{n_{bins}} (N_{b_i}^{data} \ln(\lambda P_{b_i}) - \lambda P_{b_i} - \ln N_{b_i}^{data}!) \quad (12.6)$$

Where  $N_{b_i}^{data}$  is the number of data in the  $i$ th bin,  $\lambda$  is the expected rate in the region,  $P_{b_i}$  is the probability of an event being in the  $i$ th bin if it is in the signal region and  $\vec{z}$  is the fitted parameters such as signal cross-section etc. Both  $\lambda$  and  $P_{b_i}$  can depend on the fitted parameters  $\vec{z}$  because the total amount and shape of background and signal can change with the fitted parameters.

A mathematically equivalent interpretation is that  $\lambda P_{b_i}$  is simply the expected number of events in a particular bin. In this case, equation 12.5 and 12.6 become 12.7 and 12.8 where  $N_{b_i}^{MC}$  is the expected number of events from simulation.

$$\mathcal{L}(N_{b_i}^{data}|\vec{z}) = \prod_{k=1}^{n_{bins}} \frac{(N_{b_i}^{MC})^{N_{b_i}^{data}} e^{-N_{b_i}^{MC}}}{N_{b_i}^{data}!} \quad (12.7)$$

$$\mathcal{M}(\vec{z}) = -\ln(\mathcal{L}(\vec{z})) = -\sum_{i=1}^{n_{bins}} (N_{b_i}^{data} \ln(N_{b_i}^{MC}) - N_{b_i}^{MC} - \ln N_{b_i}^{data}!) \quad (12.8)$$

Simultaneous fits to multiple regions is performed by simultaneously maximizing the total negative log likelihood of all fitted regions. The total negative log likelihood is simply a sum of the individual likelihood of each region.

## 12.2 OVERVIEW OF FITTING TO CONTROL REGIONS AND SIGNAL REGIONS

We hope to both predict the number of expected background events and extract the amount of signal present by performing log likelihood fits to the control regions and signal region in our analysis.

We normalize backgrounds to data in control regions dominated by background but are kinematically similar to the signal region. The background normalization is allowed to float and the fit will extract the total amount of background that best describe the data in all the different control regions. All backgrounds that form a statistically significant contribution to the total background in SR has a corresponding CR. The background estimation techniques and definitions of these CRs are given in chapter 10.

The amount of MC background in both the CR and SR will fluctuate with experimental and theoretical systematics for the fit. However after the fit the total amount of background will be nor-

malized to the CR. If the raw MC yield for background fluctuate down with a given systematic then the normalization scale factor in the CR will increase. If the raw MC background yield in SR also decreases by the same amount, then the increased normalization scale factor will compensate for this and bring fitted background yield in SR remains unchanged. In this way, the control region help cancel systematic variations by directly measuring the amount of background in from data instead of relying on MC predictions.

The more kinematically similar the definition of the CR to the SR, the better the cancellation. Any extrapolation between CR and SR must only be across well modeled variables. Otherwise large systematic uncertainties will arise due to extrapolation cross poorly modeled parts of the simulation or worse the background prediction maybe wrong.

We can also check the result of our background predictions without unblinding the signal region in validation regions. Validation regions receive the normalization scale factors to background from the fit to the control region but do not participate in the fit. The VRs are designed to be kinematically similar to the SRs while keeping signal contaminations low. In this way, the VRs serves as a mid-point to check the extrapolation between CR and SR.

The relationship between CR, SR and VR is graphically depicted in figure 12.1.

In an excess were to exist in the SR, a simultaneous fit to all CR and SR is performed for to calculate the statistical significance of any potential excess in the case of discovery. If no excess were found, then a simultaneous fit to all CR and SR is also performed quantify the maximum amount of signal cross-section that can be excluded.

The background normalization and systematic uncertainty is also extracted through these simul-

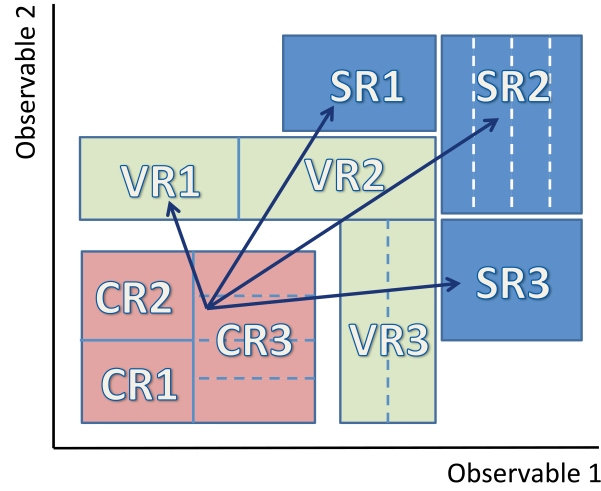


**Figure 12.1:** Basic diagram of data driven background estimation techniques. We define control regions (CR) that is dominated by background and have little signal. We can estimate the amount of background we expect in the signal region (SR) by measuring the amount of background in the CR and extrapolating to the SR using MC predictions.

taneous fit to control and signal regions.

However, the CRs have much higher statistics than the SR. Therefore, the background rate is mainly constrained by the CR and the SR mainly constrain the amount of signal. Therefore we can quantify the amount of background and the systematic uncertainty that we would expect in the signal region by performing a background only fit where only CRs are fitted. In this case, the SR behaves like another VR and is not fitted.

These three types of fits, the background only fit, the discovery fit and the exclusion fit are covered in more detail in sections 12.4 to 12.5. The parameterization of systematics as constrained nuisance parameters is covered in section 12.3.

We use the software package `HistFitter` (version `HistFitter-00-00-53`) to perform the statistical analysis.<sup>3</sup> `HistFitter` provides many tools to easily manage and integrate multiple

CR, SR backgrounds, and systematics. `HistFitter` is built upon other statistical analysis software including `Roofit`.<sup>2</sup> At its core `HistFitter` is still performing log likelihood fitting based on the principle introduced in section 12.1 but the software makes bookkeeping of the different CR, SRs and fits much more streamlined.

### 12.3 PARAMETERIZATION OF SYSTEMATICS AS GAUSSIAN CONSTRAINTS

Systematics uncertainties are parameterized as fitted parameters called nuisance parameters. The nuisance parameter, defined as  $\alpha$ , is constrained to a particular value by a constraint function  $C(\alpha)$ . The fitted PDF  $P(x|\vec{z}, \alpha)$  can depend on a number of unconstrained fitted parameter  $\vec{z}$  and the constrained  $\alpha$ . The constraint function  $C(\alpha)$  is multiplied to the likelihood as shown in equation 12.9 and contributes to the total likelihood.

$$\mathcal{L}(\vec{z}, \alpha) = \prod_{i=1}^n P(x_i|\vec{z}, \alpha) C(\alpha) \quad (12.9)$$

Now the value of  $\alpha$  corresponding to the maximum likelihood  $\mathcal{L}(\vec{z}, \alpha)$  may not be the same as value where  $C(\alpha)$  is maximized. Depending on the data points  $x_i$ , the component of the likelihood from  $\prod_{i=1}^n P(x_i|\vec{z}, \alpha)$  may be bigger even if  $C(\alpha)$  is not at its maximum.

We pay a penalty on the total likelihood if the nuisance parameter  $\alpha$  deviates from the value with maximum  $C(\alpha)$ . The fit finds the optimal point between changing the  $\alpha$  so that the PDF best describes the data and the cost from the constraint function on  $\alpha$ .

We use Gaussians as the constraint function for all systematics. The nominal value corresponds

to  $\alpha = 0$  and the plus and minus 1 sigma deviation corresponds to  $\alpha = \pm 1$ .

Two types of systematics exist normalization and shape for our analysis. Normalizations systematics are only applied to the total normalization of the background and signal in the SR. For normalization background we determine how much the backgrounds and signal will fluctuate with the  $\pm 1$  sigma variation in systematic in each of our CRs and SR.

Shape systematics on the other allow different bins in  $R_{\text{ISR}}$  in the SR to fluctuate at different rates differently. For example a shape systematic with the  $\alpha$  value of 0.1 and have a 10 percent increase in background in bin 1 but a 15 percent increase in background in bin 2. The fluctuation in each bin is determined independently.

#### 12.4 BACKGROUND ONLY FIT AND BACKGROUND ESTIMATION

For the background only fit, the CRs are simultaneously fitted but the SR is not fitted. The backgrounds in the SR are normalized to the background normalization scale factors derived from the fit to the CRs. No signal sample is included in the fit and potential signal contamination in the CR is ignored. The background only fit is performed to estimate the background systematic uncertainties and the amount of expected background in the signal region in the absence of an signal.

The background only fit has the advantage of being able to quantify the expected amount of background and systematic uncertainties on background while the SR is blinded.

The background normalizations predicted in the background only fit may differ from the discovery and exclusion fits because the SR is simultaneously fitted in those fits. This difference should be

small as long as the CRs are well designed and have much higher constraining power on the amount of background than the SR. The CRs that have high purity in a single background and high statistics will have much stronger constraining power on the amount of background than the lower statistics SR.

## 12.5 EXCLUSION FIT AND EXCLUSION LIMIT CALCULATION

The exclusion fit is performed as a simultaneous fit to all CRs and SR. The signal sample is included in both CR and SR and normalized to a signal strength parameter. The signal strength parameter can be varied but is constrained to be non-negative. The five bins in  $R_{\text{ISR}}$  is simultaneously fitted in the SR for exclusion.

The best fit signal strength is found when the negative log likelihood (NLL) is at a minimum after fitting to data. As the signal strength deviates from the best fit value, the NLL increases and we are more confident that the signal strength is not supported by data. The NLL's variation and the statistical significance should be related to one another by a parabola if the statistics in SR is high enough. The signal strength corresponding to when the NLL is 1 above the minimum NLL corresponds to the 1 sigma confidence interval on signal strength. The signal strength corresponding to when the NLL is 4 above the minimum NLL corresponds to the 2 sigma confidence interval on signal strength and so on.

In other words, we use the difference in NLL as our test statistic and the relationship between the test statistic and statistical significance approaches the asymptotic case of a parabola at high



statistics.

In this way we can find the 95 percent confidence interval on the signal cross-section. If the high end of the 95 percent confidence interval on signal cross-section is less than the production cross-section of a particular signal model then that signal model has been excluded to at least 95 confidence.

Alternatively we can calculate the NLL corresponding to the nominal signal strength of each signal model and compare it with the fitted minimum NLL. The difference in the two NLLs can be converted into the statistical significance using the parabolic relationship between the two. The statistical significance of the nominal signal strength for a particular model is the exclusion p-value for the model. If the exclusion p-value is below 5 percent then the signal model has been excluded to 95 confidence.

We calculate the exclusion p-value corresponding to a grid of signal models each with a different stop and neutralino mass. The p-values are plotted in a 2D graph with the stop mass along the x-axis and the neutralino mass along the y-axis. These p-values are then interpolated over to form a 2D contour plot. The contour corresponding to the 95 percent exclusion limit is then drawn.

## 12.6 DISCOVERY FIT AND DISCOVERY SIGNIFICANCE CALCULATION

The discovery fit is also performed as a simultaneous fit to all CRs and SR. The signal sample is included only in the SR but not to the CR in the fit. This choice of excluding the signal sample from the CR gives a more conservative estimate of the discovery significance. If a signal is present in na-

ture, the signal contamination in the CR would still exist in data. We essentially over-estimate the amount of background by counting any potential signal contamination in the CR as background. Again, a well designed CR has little signal contamination so the difference between this approach and exclusion fit should be small. Our signal contamination is less than 15 percent for all signal samples that we are sensitive to but have not been excluded by previous 8 TeV ATLAS analysis. The signal contamination is less than 10 percent for all stop masses above 300 GeV.

We do not statically combine the 5  $R_{\text{ISR}}$  bins for the discovery fit. Instead a single  $R_{\text{ISR}}$  bin is fitted at a time and the bin with the best significance is used as the discovery significance for the signal model. Again this is a conservative approach and gives us worse discovery significances but it makes the analysis less sensitive to shape uncertainties in signal.

We also use the difference in NLL as our test static for our discovery fit. The signal strength and background normalization that best fit the data is found at the minimum NLL. Then we calculate the NLL with a signal strength of zero. The difference between the NLL with a signal strength of zero and the best fit NLL is our test statistic. The relationship between the test statistic is given by a parabola in the asymptotic high statistics case. We assume we are in the asymptotic case and derive the statistic significance of the zero signal strength fit.

The statistical significance of the zero signal strength fit represent the amount of disagreement between data and the no signal case. In other words, the statistical significance of the zero signal strength fit is the p-value of the no signal hypothesis test. This p-value is the discovery significance for the analysis. If the discovery significance is above 5 sigma then discovery can be claimed.

# 13

## Results

The observed number of events in the various control regions are included in a fit that uses the profile likelihood ratio method to determine the SM background estimates in each signal region. This procedure takes common systematic uncertainties (discussed in Section ??) between the control and signal regions and their correlations into account; they are treated as nuisance parameters in the fit and are modelled by Gaussian probability density functions.

In general control regions are designed for as many of the SRs as possible. However, due to statistical limitation three CRs are used for all SRs: CRW, CRST, CRTTGamma. For these regions a choice needs to be made for which of the specially designed CRTop and CRZ regions should be used in the fits. Below is a summary:

- CRW: Due to the top mass veto the only CRs without an ISR or top mass requirement are used in CRW. These are CRZD and CRTopD.
- CRST: it was found that this CR was mainly populated with events that fall in the  $T_0$  category (66%). For this reason, CRZAB- $T_0$  is used for the Z fit. The  $E_T^{\text{miss}}$  requirements of CRTopB are closer to CRST and thus CRTopB is used for the top background fit.
- $t\bar{t}+V$ : For CRTop, CRTopB $T_0$  was chosen again because the  $T_0$  made up a large part of the events (40%) in CRTTGamma. For similar reasons, CRZAB- $T_0$  is used for the Z background.

Three different likelihood fits are performed to extract the results.

Background-only fit: Only the control regions are used to constrain the fit parameters. Potential signal contamination is neglected and the number of observed events in the signal regions is not taken into account in the fit.

Exclusion fit: Both control and signal regions are used to constrain the fit parameters. The signal contribution as predicted by the tested model is taken into account in both regions using an additional free parameter for the non-SM signal strength in the likelihood fit that is constrained to be non-negative. Since the observed event yield in the signal region is used, the background prediction can differ from the prediction on the background-only fit. The exclusion fit configuration is used to produce all the model-dependent limits.

Discovery fit: Both control and signal regions are used to constrain the fit parameters. A potential signal contribution is considered in the signal regions but neglected in the control regions. This background prediction is conservative since any signal contribution in the control regions is attributed to background and thus yields a possible overestimate of the background in the signal regions. The discovery fit configuration is used to produce upper limits on the visible cross-sections.

The `HistFitter` results with data samples are described in Section 13.0.2.

### 13.0.1 UNBLINDED DISTRIBUTIONS

Figures ??, ??, 13.1, ??, ?? show the postfit, unblinded distribution of some of the most discriminating variables of SRA, SRB, SRC, SRD, and SRE at  $36.47 \text{ fb}^{-1}$ . For SRA and SRB the distributions for individual categories are shown. Additionally, the error bands include both MC statistical and all detector systematical uncertainties.

**Figure 13.1:** Unblinded  $R_{\text{ISR}}$  and  $p_{\text{T}}^{\text{ISR}}$  distributions for SRC1-5 for  $36.47 \text{ fb}^{-1}$ .

### 13.0.2 BACKGROUND-ONLY FIT

The background-only fit has been performed taking the dominant experimental systematics and the theoretical systematics for  $W/Z$ +jets and  $t\bar{t}$  (RadLoHi and PowhegHerwigpp only) into account (to be updated). The yields in the control regions, normalized to  $36.47 \text{ fb}^{-1}$  are shown in Tables ??, ??, 13.2, ??, ?? and ??. The resulting scale factors for the backgrounds are summarized in Table 13.1. The yields in the validation regions are shown in Tables ??, ??, 13.3, ?? and ??. The background yields in the signal regions, normalized to  $36.47 \text{ fb}^{-1}$ , are shown in Tables ??, ??, 13.4, 13.5, ??, and ??; the signal regions are now unblinded and the number of events seen in the data are also shown.

The breakdown of the post-fit systematic uncertainties, summed over the backgrounds, is shown in Tables ??, ??, 13.6, 13.7, ?? and ??. The breakdown of the post-fit systematic uncertainties, summed over the backgrounds, but separated by signal region (so that the ordering is clearer in each signal region) can be found in Appendix ??.

A plot of the correlation between fit parameters of interest and the nuisance parameters is shown in Fig. 13.2 and the post-fit pull plot for the background-only fit is shown in Fig. 13.3.

MC sample	Fitted scale factor
ttbar (SRA_TT)	$1.147 \pm 0.146$
ttbar (SRA_TW)	$1.150 \pm 0.114$
ttbar (SRA_To)	$0.856 \pm 0.123$
ttbar (SRB_TT)	$1.219 \pm 0.160$
ttbar (SRB_TW)	$1.009 \pm 0.0697$
ttbar (SRB_To)	$0.904 \pm 0.0524$
ttbar (SRC)	$0.674 \pm 0.0479$
ttbar (SRD)	$1.032 \pm 0.110$
ttbar (SRE)	$1.041 \pm 0.1083$
W+jets	$1.122 \pm 0.155$
Z+jets (SRA,B TT and TW)	$1.213 \pm 0.232$
Z+jets (SRA,B To)	$1.115 \pm 0.143$
Z+jets (SRD)	$1.081 \pm 0.145$
Z+jets (SRE)	$1.233 \pm 0.149$
Single top	$1.211 \pm 0.389$
ttbar $\gamma$	$1.275 \pm 0.184$

**Table 13.1:** Fitted scale factors for the MC background samples based on  $36.47 \text{ fb}^{-1}$  of data.



CRTopCDE yields	CRTopC	CRTopD	CRTopE
Observed events	597	165	51
Fitted bkg events	$597.00 \pm 24.43$	$165.00 \pm 12.84$	$51.00 \pm 7.14$
Fitted $T\bar{T}$ events	$450.40 \pm 31.09$	$138.47 \pm 14.02$	$44.25 \pm 7.27$
Fitted Wjets events	$59.70 \pm 12.69$	$4.57 \pm 1.05$	$1.98 \pm 0.36$
Fitted Zjets events	$2.31 \pm 0.84$	$0.09 \pm 0.06$	$0.02 \pm 0.02$
Fitted $T\bar{t}$ events	$11.23 \pm 1.80$	$2.94 \pm 0.84$	$0.95 \pm 0.43$
Fitted SingleTop events	$66.14 \pm 19.97$	$17.80 \pm 5.99$	$2.54 \pm 0.81$
Fitted Diboson events	$7.22 \pm 2.14$	$1.13^{+1.27}_{-1.13}$	$1.26 \pm 1.25$
MC exp. SM events	793.63	156.47	48.40
MC exp. $T\bar{T}$ events	667.86	134.18	42.52
MC exp. Wjets events	53.23	4.08	1.77
MC exp. Zjets events	1.90	0.08	0.02
MC exp. $T\bar{t}$ events	8.80	2.30	0.74
MC exp. SingleTop events	54.61	14.70	2.10
MC exp. Diboson events	7.22	1.13	1.26

**Table 13.2:** Region: CRTopCDE. Background-only fit results for an integrated luminosity of  $36.47 \text{ fb}^{-1}$ . The uncertainties are statistical and systematic.

VRTop yields	VRTopC	VRTopD	VRTopE
Observed events	281	238	106
Fitted bkg events	$277.97 \pm 17.53$	$193.21 \pm 20.29$	$83.53 \pm 21.79$
Fitted $T\bar{T}$ events	$156.22 \pm 15.28$	$164.44 \pm 21.50$	$69.17 \pm 22.06$
Fitted Wjets events	$43.25 \pm 9.44$	$3.94 \pm 0.91$	$2.27 \pm 0.77$
Fitted Zjets events	$39.09 \pm 9.93$	$5.89 \pm 1.19$	$4.43 \pm 1.00$
Fitted $T\bar{t}$ events	$8.89 \pm 1.43$	$4.72 \pm 0.89$	$3.08 \pm 0.78$
Fitted SingleTop events	$24.92 \pm 8.61$	$13.34 \pm 4.65$	$3.76 \pm 1.23$
Fitted Diboson events	$5.60 \pm 1.63$	$0.88 \pm 0.41$	$0.82 \pm 0.46$
MC exp. SM events	335.59	183.91	78.42
MC exp. $T\bar{T}$ events	231.65	159.35	66.46
MC exp. Wjets events	38.56	3.51	2.02
MC exp. Zjets events	32.23	5.45	3.59
MC exp. $T\bar{t}$ events	6.97	3.70	2.41
MC exp. SingleTop events	20.58	11.01	3.11
MC exp. Diboson events	5.60	0.88	0.82

**Table 13.3:** Region: VRTopCDE. Background-only fit results for an integrated luminosity of  $36.47 \text{ fb}^{-1}$ . The uncertainties are statistical and systematic.

SRC yields	SRC <sub>1</sub>	SRC <sub>2</sub>	SRC <sub>3</sub>
Observed events	23	22	23
Fitted bkg events	$13.89 \pm 2.89$	$25.32 \pm 4.29$	$18.02 \pm 2.64$
Fitted T $\bar{T}$ events	$11.25 \pm 2.99$	$21.39 \pm 3.67$	$14.64 \pm 2.36$
Fitted Wjets events	$0.64 \pm 0.19$	$1.59 \pm 0.44$	$1.54 \pm 0.57$
Fitted Zjets events	$0.00 \pm 0.00$	$0.00 \pm 0.00$	$0.00 \pm 0.00$
Fitted T $\bar{t}$ events	$0.16^{+0.28}_{-0.16}$	$0.52 \pm 0.44$	$0.49 \pm 0.31$
Fitted SingleTop events	$1.42 \pm 0.98$	$1.57 \pm 1.04$	$0.85 \pm 0.36$
Fitted Diboson events	$0.41 \pm 0.24$	$0.24 \pm 0.05$	$0.51 \pm 0.20$
MC exp. SM events	18.96	35.08	24.66
MC exp. T $\bar{T}$ events	16.68	31.72	21.70
MC exp. Wjets events	0.57	1.42	1.37
MC exp. Zjets events	0.00	0.00	0.00
MC exp. T $\bar{t}$ events	0.13	0.41	0.38
MC exp. SingleTop events	1.17	1.29	0.70
MC exp. Diboson events	0.41	0.24	0.51

**Table 13.4:** Region: SRC. Background-only fit results for an integrated luminosity of  $36.47 \text{ fb}^{-1}$ . The uncertainties are statistical and systematic.

SRC yields	SRC <sub>4</sub>	SRC <sub>5</sub>
Observed events	2	0
Fitted bkg events	$6.94 \pm 1.13$	$0.66 \pm 0.28$
Fitted T $\bar{T}$ bar events	$4.26 \pm 0.99$	$0.41 \pm 0.19$
Fitted Wjets events	$1.64 \pm 0.44$	$0.18 \pm 0.10$
Fitted Zjets events	$0.00 \pm 0.00$	$0.00 \pm 0.00$
Fitted T $\bar{t}$ barV events	$0.09 \pm 0.09$	$0.07 \pm 0.03$
Fitted SingleTop events	$0.77 \pm 0.30$	$0.00 \pm 0.00$
Fitted Diboson events	$0.18 \pm 0.12$	$0.00 \pm 0.00$
MC exp. SM events	8.66	0.83
MC exp. T $\bar{T}$ bar events	6.31	0.60
MC exp. Wjets events	1.46	0.16
MC exp. Zjets events	0.00	0.00
MC exp. T $\bar{t}$ barV events	0.07	0.06
MC exp. SingleTop events	0.64	0.00
MC exp. Diboson events	0.18	0.00

**Table 13.5:** Region: SRC. Background-only fit results for an integrated luminosity of  $36.47 \text{ fb}^{-1}$ . The uncertainties are statistical and systematic.

Uncertainty of channel	SRC <sub>1</sub>	SRC <sub>2</sub>	SRC <sub>3</sub>
Total background expectation	13.89	25.32	18.02
Total statistical ( $\sqrt{N_{\text{exp}}}$ )	$\pm 3.73$	$\pm 5.03$	$\pm 4.24$
Total background systematic	$\pm 2.89$ [20.81%]	$\pm 4.29$ [16.96%]	$\pm 2.64$ [14.66%]
alpha_RadLoHi	$\pm 2.13$ [15.3%]	$\pm 1.88$ [7.4%]	$\pm 0.58$ [3.2%]
gamma_stat_SRC <sub>1</sub> _cuts_bin_o	$\pm 1.26$ [9.1%]	$\pm 0.00$ [0.00%]	$\pm 0.00$ [0.00%]
mu_ttbarC	$\pm 0.80$ [5.7%]	$\pm 1.52$ [6.0%]	$\pm 1.04$ [5.8%]
alpha_JER	$\pm 0.57$ [4.1%]	$\pm 2.58$ [10.2%]	$\pm 0.63$ [3.5%]
alpha_PowhegHerwigpp	$\pm 0.50$ [3.6%]	$\pm 1.13$ [4.5%]	$\pm 1.49$ [8.3%]
alpha_JET_GroupedNP_2	$\pm 0.46$ [3.3%]	$\pm 0.20$ [0.79%]	$\pm 0.00$ [0.02%]
mu_SingleTop	$\pm 0.46$ [3.3%]	$\pm 0.50$ [2.0%]	$\pm 0.27$ [1.5%]
alpha_MET_SoftTrk_ResoPara	$\pm 0.36$ [2.6%]	$\pm 0.37$ [1.5%]	$\pm 0.48$ [2.7%]
alpha_LightEff	$\pm 0.32$ [2.3%]	$\pm 0.38$ [1.5%]	$\pm 0.04$ [0.20%]
alpha_MET_SoftTrk_ResoPerp	$\pm 0.31$ [2.2%]	$\pm 0.68$ [2.7%]	$\pm 0.34$ [1.9%]
alpha_JET_GroupedNP_3	$\pm 0.29$ [2.1%]	$\pm 0.09$ [0.37%]	$\pm 0.06$ [0.35%]
alpha_cEff	$\pm 0.20$ [1.4%]	$\pm 0.31$ [1.2%]	$\pm 0.10$ [0.56%]
alpha_MET_SoftTrk_Scale	$\pm 0.19$ [1.4%]	$\pm 0.15$ [0.60%]	$\pm 0.02$ [0.10%]
alpha_bEff	$\pm 0.17$ [1.2%]	$\pm 0.03$ [0.10%]	$\pm 0.04$ [0.20%]
alpha_CExtrap	$\pm 0.14$ [0.98%]	$\pm 0.28$ [1.1%]	$\pm 0.17$ [0.94%]
mu_Wjets	$\pm 0.09$ [0.64%]	$\pm 0.22$ [0.87%]	$\pm 0.21$ [1.2%]
alpha_theoSysW	$\pm 0.07$ [0.53%]	$\pm 0.20$ [0.79%]	$\pm 0.18$ [1.0%]
alpha_JET_GroupedNP_1	$\pm 0.06$ [0.40%]	$\pm 0.72$ [2.9%]	$\pm 0.98$ [5.4%]
alpha_PILEUP	$\pm 0.05$ [0.39%]	$\pm 0.39$ [1.5%]	$\pm 0.68$ [3.8%]
alpha_FTEtrap	$\pm 0.03$ [0.21%]	$\pm 0.01$ [0.04%]	$\pm 0.05$ [0.29%]
alpha_JET_EtaNonClosure	$\pm 0.03$ [0.20%]	$\pm 0.90$ [3.6%]	$\pm 0.19$ [1.1%]
mu_TtbarV	$\pm 0.02$ [0.17%]	$\pm 0.08$ [0.30%]	$\pm 0.07$ [0.39%]
alpha_JVT	$\pm 0.01$ [0.04%]	$\pm 0.02$ [0.08%]	$\pm 0.05$ [0.30%]
gamma_stat_SRC <sub>2</sub> _cuts_bin_o	$\pm 0.00$ [0.00%]	$\pm 1.59$ [6.3%]	$\pm 0.00$ [0.00%]
gamma_stat_SRC <sub>3</sub> _cuts_bin_o	$\pm 0.00$ [0.00%]	$\pm 0.00$ [0.00%]	$\pm 1.22$ [6.8%]

**Table 13.6:** Breakdown of the dominant systematic uncertainties on background estimates. Note that the individual uncertainties can be correlated, and do not necessarily add up quadratically to the total background uncertainty. The percentages show the size of the uncertainty relative to the total expected background.

Uncertainty of channel	SRC <sub>4</sub>	SRC <sub>5</sub>
Total background expectation	6.94	0.66
Total statistical ( $\sqrt{N_{\text{exp}}}$ )	$\pm 2.63$	$\pm 0.82$
Total background systematic	$\pm 1.13$ [16.33%]	$\pm 0.28$ [41.43%]
gamma_stat_SRC4_cuts_bin_o	$\pm 0.72$ [10.4%]	$\pm 0.00$ [0.00%]
alpha_RadLoHi	$\pm 0.48$ [7.0%]	$\pm 0.04$ [5.4%]
alpha_PowhegHerwigpp	$\pm 0.39$ [5.6%]	$\pm 0.07$ [10.9%]
alpha_JER	$\pm 0.36$ [5.1%]	$\pm 0.11$ [16.2%]
alpha_PILEUP	$\pm 0.32$ [4.6%]	$\pm 0.05$ [7.9%]
mu_ttbarC	$\pm 0.30$ [4.4%]	$\pm 0.03$ [4.4%]
mu_SingleTop	$\pm 0.25$ [3.6%]	$\pm 0.00$ [0.00%]
mu_Wjets	$\pm 0.23$ [3.3%]	$\pm 0.03$ [3.8%]
alpha_theoSysW	$\pm 0.18$ [2.5%]	$\pm 0.02$ [2.6%]
alpha_JET_GroupedNP_1	$\pm 0.15$ [2.1%]	$\pm 0.02$ [3.2%]
alpha_MET_SoftTrk_ResoPara	$\pm 0.11$ [1.6%]	$\pm 0.04$ [5.8%]
alpha_bEff	$\pm 0.10$ [1.5%]	$\pm 0.00$ [0.20%]
alpha_LightEff	$\pm 0.09$ [1.3%]	$\pm 0.04$ [5.9%]
alpha_JET_GroupedNP_2	$\pm 0.07$ [1.0%]	$\pm 0.05$ [7.2%]
alpha_FTEtrap	$\pm 0.05$ [0.78%]	$\pm 0.01$ [1.2%]
alpha_MET_SoftTrk_ResoPerp	$\pm 0.05$ [0.75%]	$\pm 0.08$ [11.4%]
alpha_JET_GroupedNP_3	$\pm 0.04$ [0.60%]	$\pm 0.05$ [7.8%]
alpha_MET_SoftTrk_Scale	$\pm 0.03$ [0.45%]	$\pm 0.03$ [4.8%]
alpha_JVT	$\pm 0.03$ [0.39%]	$\pm 0.00$ [0.24%]
alpha_JET_EtaNonClosure	$\pm 0.02$ [0.28%]	$\pm 0.05$ [6.8%]
alpha_cEff	$\pm 0.01$ [0.20%]	$\pm 0.00$ [0.71%]
mu_TtbarV	$\pm 0.01$ [0.20%]	$\pm 0.01$ [1.6%]
alpha_CExtrap	$\pm 0.01$ [0.08%]	$\pm 0.00$ [0.63%]
gamma_stat_SRC5_cuts_bin_o	$\pm 0.00$ [0.00%]	$\pm 0.20$ [29.6%]

**Table 13.7:** Breakdown of the dominant systematic uncertainties on background estimates. Note that the individual uncertainties can be correlated, and do not necessarily add up quadratically to the total background uncertainty. The percentages show the size of the uncertainty relative to the total expected background.

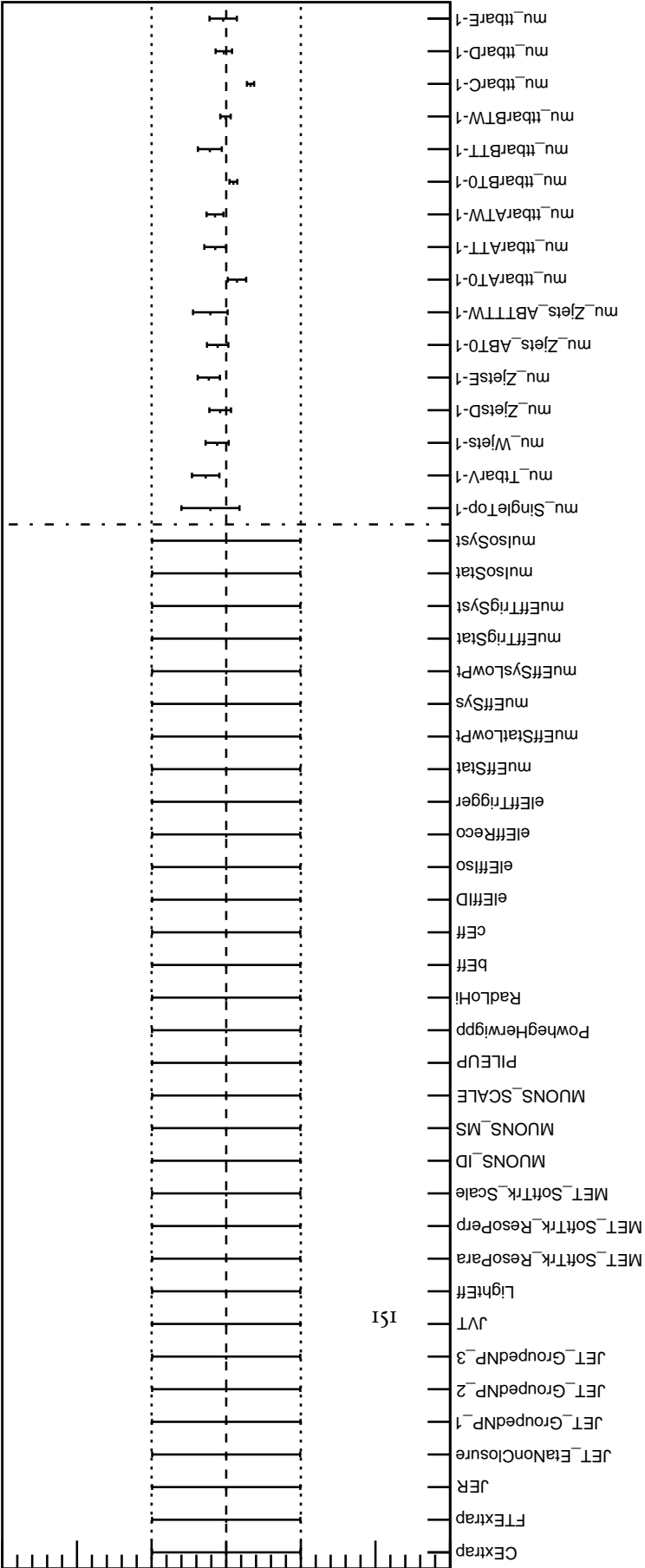
## Reduced correlation matrix

### 13.0.3 EXCLUSION-FIT RESULTS

#### RESULTS IN THE $m(\tilde{\chi}_1^0)$ VS $m(\tilde{t})$ GRID

The results of the exclusion fit for SRA, SRB and SRC are shown in Figures ??, ?? and 13.4 respectively. The signal regions are still blinded so that the “observed limit” comes from setting the observation equal to the background expectation from the Monte Carlo (pre-fit). The SRA (SRB) (SRC) results are obtained by statistically combining the results from SRA\_TT, SRA\_TW and SRA\_To (SRB\_TT, SRB\_TW and SRB\_To) (SRC1-5). SRA, SRB and SRC are then combined by taking the result with the best expected  $CL_s$ ; this combination is shown in Figure 13.5.





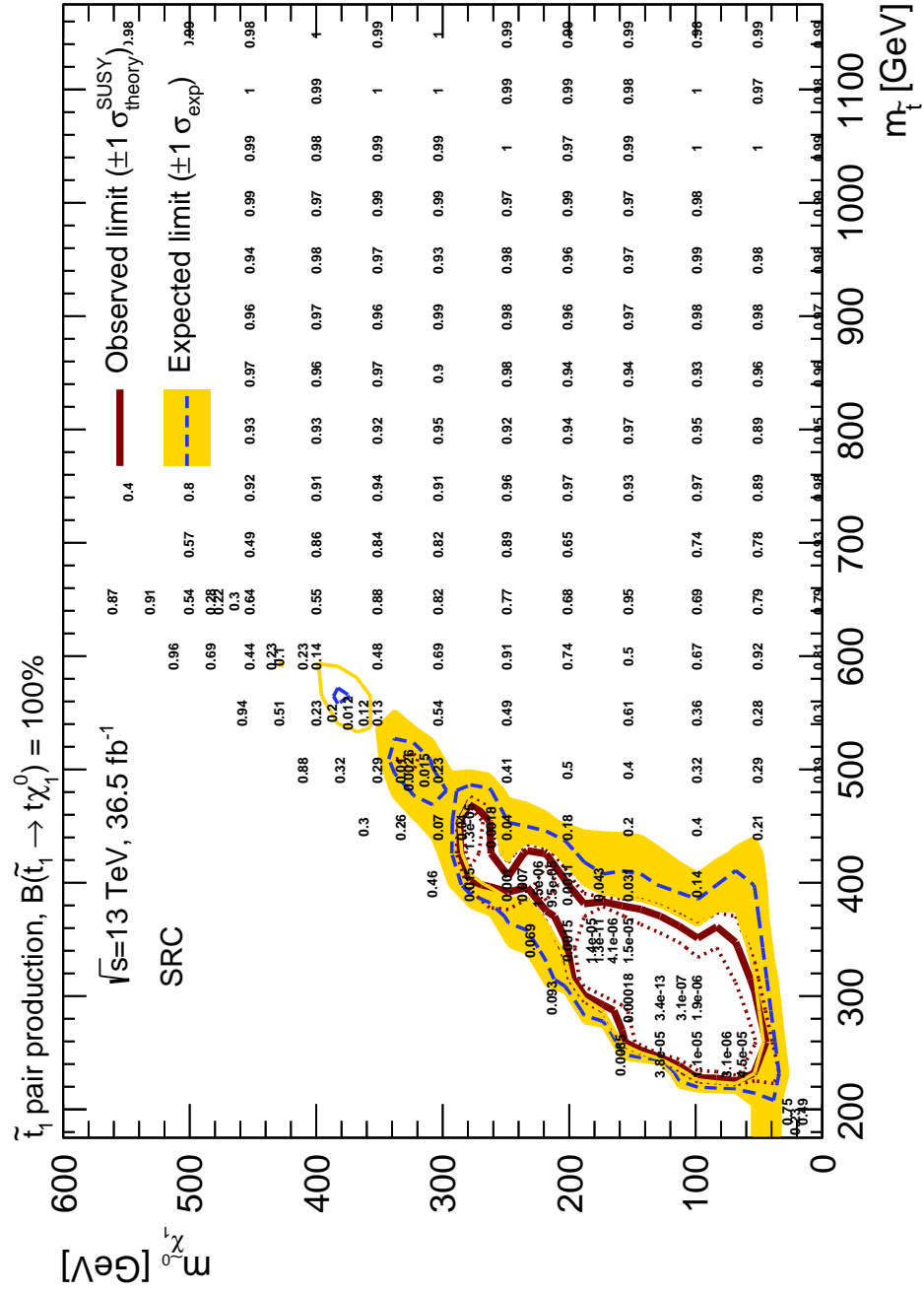


**Figure 13.4:** Results of the exclusion fits in the  $tN1$  grid from the combination of SRC1-5. The numbers centered on the grid points indicate the expected CLs values.

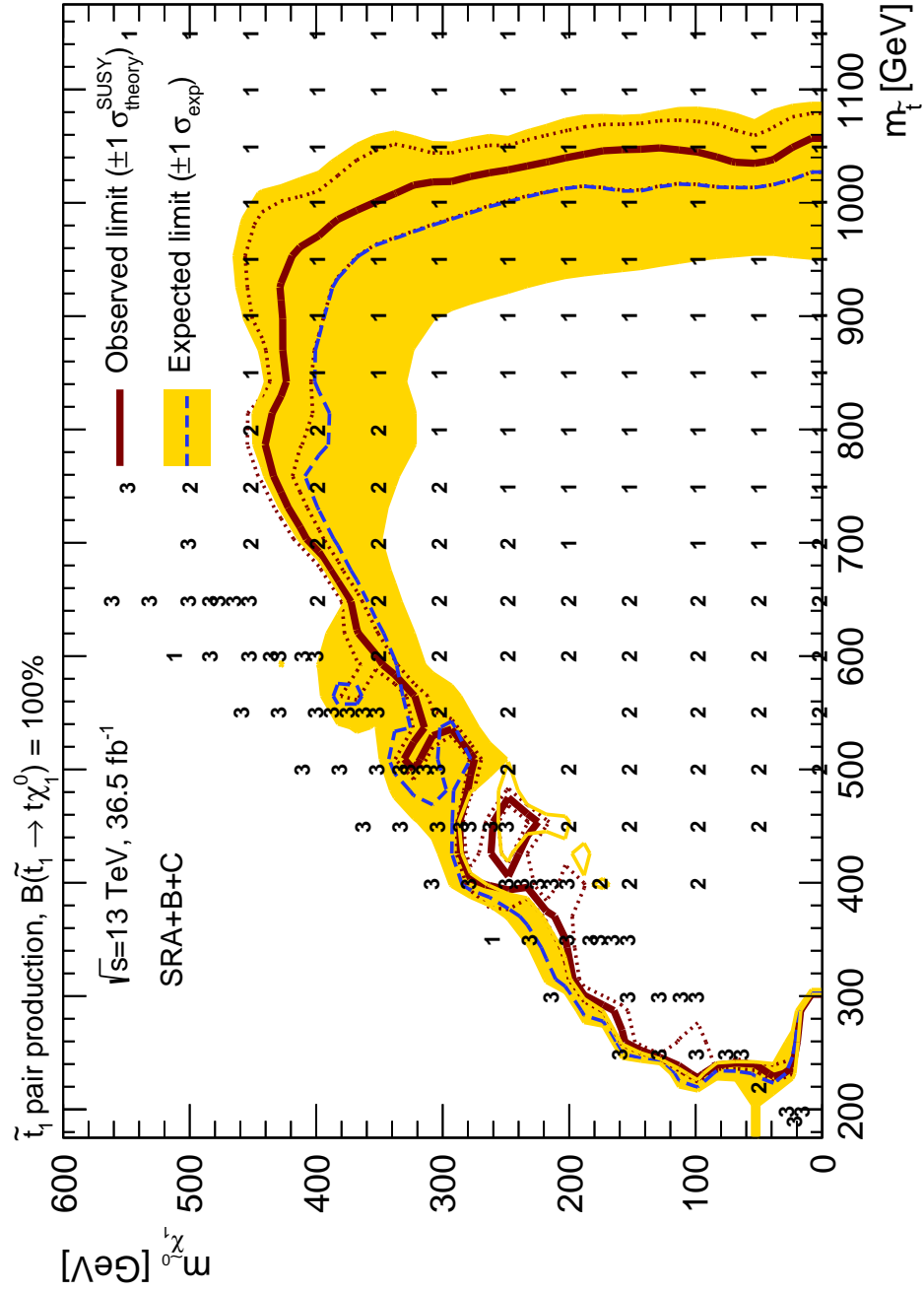


**Figure 13.5:** Results of the exclusion fits in the  $tN1$  grid from the combination of SRA, SRB and SRC, based on the best expected  $CL_s$ . The numbers centered on the grid points indicate which of the signal regions gave the best expected  $CL_s$  (with 1,2,3 corresponding to SRA,B,C respectively).

# 14

## Interpretation of Results

# 15

## Conclusion



## Sanity Checks



THIS THESIS WAS TYPESET using L<sup>A</sup>T<sub>E</sub>X,  
originally developed by Leslie Lamport  
and based on Donald Knuth's T<sub>E</sub>X.

The body text is set in 11 point Egenolff-Berner Garamond, a revival of Claude Garamont's humanist typeface. The above illustration, *Science Experiment 02*, was created by Ben Schlitter and released under **CC BY-NC-ND 3.0**. A template that can be used to format a PhD dissertation with this look & feel has been released under the permissive AGPL license, and can be found online at [github.com/suchow/Dissertate](https://github.com/suchow/Dissertate) or from its lead author, Jordan Suchow, at [suchow@post.harvard.edu](mailto:suchow@post.harvard.edu).